R. & M. No. 3044
(17,407)
A.R.C. Technical Report

MINISTRY OF SUPPLY

AERONAUTICAL RESEARCH COUNCIL
REPORTS AND MEMORANDA

On Some Aspects of the Use of Shock Tubes in Aerodynamic Research

By

B. D. HENSHALL, B.Sc.
University of Bristol, Department of Aeronautical Engineering

LONDON: HER MAJESTY'S STATIONERY OFFICE

1957

PRICE £1 10s 0d NET

On Some Aspects of the Use of Shock Tubes in Aerodynamic Research

By

B. D. Henshall, B.Sc.

University of Bristol, Department of Aeronautical Engineering

---

Summary.—Interest has recently been revived in an apparatus which was first developed fifty years ago. This apparatus, which is known today as a shock tube, consists of a simple duct which may be closed or open at one end, and closed at the other end. A diaphragm divides this duct into two compartments which initially contain gases at different pressures. When the diaphragm is ruptured, an unsteady gas motion ensues.

A survey of existing shock tube theory and experimental results has been conducted; particular emphasis was placed on the features of actual shock tube flow which diverged from ideal non-viscous theory. A basic ideal shock tube theory has been formulated in detail, using those parameters which have greatest practical significance, and subsequently, performance charts affording a rapid method for the aerodynamic design of shock tubes using air as the working fluid have been developed. Experimental results diverge from the simple ideal theory mentioned above, principally because viscous effects are present in actual shock tube flow. Careful analysis of available experimental data yielded a series of important parameters which should be incorporated in any modified theory of shock tube flow.

A new analytical approach led to the development of a theory of shock tube flow which included the effects of boundary layer growth on the walls of the shock tube and explained several features of the actual flow patterns which are at variance with ideal non-viscous theory. As presented herein, the theory is restricted to shock tube flows where the shock wave is weak, and the boundary layers on the walls of the tube are laminar and incompressible. The complete solution of shock tube flow including the effects of viscosity is a formidably difficult problem, but it is hoped that the present analysis may be a useful first step towards the full solution.

As a parallel study with the above theoretical work, the design and construction of a shock tube installation was undertaken. Low cost was one of the main criteria of this design, and a shock tube made of mahogany was finally selected. (The Bristol shock tube is believed to be the first employing wooden construction.) Ancillary equipment was developed for the installation, and particular attention was given to the optical and electronic equipment. The development of the apparatus, and principally that of the electronic instrumentation, took considerable time; but a detailed calibration of the shock tube was ultimately carried out. Finally, timed photographs of the transient diffraction of a shock wave over a wedge were obtained; this illustrated one main application of the shock tube, that is, the study of unsteady flows.

In conclusion, the probable future development and uses of shock tubes in aerodynamic research is discussed in the light of recent experimental and theoretical work.

NOTATION

a	Velocity of sound
A	Cross-sectional area of shock tube
C_+, C_-	Characteristic curves
C_p	Specific heat at constant pressure
C_v	Specific heat at constant volume

CR_3; $CR_{1\frac{1}{2}}$	Chronometer readings of the shock velocity over distances of 3 ft and $1\frac{1}{2}$ ft respectively
e, e'	Functions of shock speed
H	Hydraulic radius of shock tube $\equiv \dfrac{\text{area of tube}}{\text{perimeter}}$
M	Mach number
p	Absolute pressure
r^*, s^*	The Riemann invariants (equation 2.14a)
R	The Gas constant
$[Re]$	Reynolds number per foot
s	Entropy
t	Time
T	Absolute temperature
u	Flow velocity
U	Shock velocity
v	Gas velocity relative to shock surface
x	Distance measured along longitudinal axis of shock tube
x_0	Length of channel
$|\bar{x}_0|$	Length of chamber
y	Distance measured along normal to wall of shock tube
z	Function of shock strength $\{ = (p_s - 1)\}$
α	$\dfrac{\gamma + 1}{2(\gamma - 1)}$
β	$\left(1 + \dfrac{\gamma - 1}{2} \bar{M}\right)$
γ	C_p/C_v, the ratio of the specific heats
δ	Boundary-layer thickness
δ^*	Displacement thickness of boundary layer
θ	Momentum thickness of boundary layer or angle between shock and transverse wave (Fig. 25). In the latter case $K = \cos \theta$
η	$\dfrac{y}{\delta}$
τ	Quasi-steady flow duration
τ_w, τ_w'	Shear stresses at walls of shock tube
ξ	Co-ordinate measured along longitudinal axis of shock tube where $\xi = 0$ defines the shock position at any instant
ζ	Co-ordinate measured along longitudinal axis of shock tube where $\zeta = 0$ defines the 'linearized' rarefaction wave position at any instant

2

Chapter 11 *only*

$\bar{u}, \bar{u}'$ Free-stream velocities in transformed shock-tube problems

u, v Velocities in the boundary layer along x and y axes respectively

Non-dimensional Quantities

$V_+ = \dfrac{U}{a_0}$ Shock velocity

$V_- = \left| \dfrac{U_R}{a_0} \right|$ Velocity of reflected shock

$v_+ = \dfrac{u}{a_0}$ Flow velocity behind moving shock

$v_- = V_+ - v_+$ Function of shock speed

$X = \dfrac{x}{|\bar{x}_0|}$ Distance parameter

$X_0 = \dfrac{x_0}{|\bar{x}_0|}$ Length of channel of shock tube

$X_s, X_{cs}, |X_R|$ Positions of shock, contact surface and ' linearized ' rarefaction wave, respectively, at any instant.

$t = \dfrac{\bar{a}_0}{|\bar{x}_0|} . t$ Time.parameter (*see* Section 2.2.3.)

(t_1, X_1) Point of intersection of tail and reflected head of centred rarefaction wave (Fig. 12)

(t_2, X_2) Point of intersection of reflected shock, contact surface and reflected head of rarefaction wave (Fig. 12)

$P = \bar{p}_0/p_0$ Pressure ratio across the diaphragm

$p_s = p/p_0$ Pressure ratio across the shock wave

Superscript

$-$

Quantities related to gas initially at higher pressure in shock tube

Subscripts

0 Initial state of gas (at rest) or stagnation state

1 State of gas upstream of normal stationary shock

2 State of gas downstream of normal stationary shock

c State of gas corresponding to sonic conditions

w Wall

Correlation of Symbols

	Normal Shock Notation	*Shock-Tube Notation*
Mach number of flow behind shock ..	$(v_1 - v_2)/a_2$	M
Strength of shock	p_2/p_1	$p_s = p/p_0$
Shock velocity	v_1/a_1	$V_+ = U/a_0$
Subscripts	1	0
	2	No subscript

3

PART A—SHOCK TUBE THEORY

CHAPTER 1

The Historical Development of the Shock Tube

1.1. Introduction.—In recent years interest has been revived in an apparatus which was first developed over fifty years ago. This apparatus, which is known to-day as a shock tube, consists basically of a simple duct which may be closed or open at one end and closed at the other end. A diaphragm divides this duct into two compartments which initially contain gases at different pressures. The lower pressure compartment is called the ' channel ' and the higher pressure compartment is termed the ' chamber '. Normally the channel length exceeds the chamber length by up to ten times. When the diaphragm is ruptured, the ensuing shock-tube flow consists of an expansion wave moving into the higher pressure gas and a shock wave moving into the lower pressure gas ; these waves are separated by a region of constant velocity flow in the direction of the shock propagation. In a conventional shock tube the cross-section is constant, the ends are closed, and air is used on both sides of the diaphragm.

1.2. Physical Description of Ideal Shock-Tube Flow.—The ideal unsteady flow processes which occur in a shock tube when the diaphragm is ruptured will be treated mathematically in the next chapter ; however, at this stage, a qualitative survey of the flow may be helpful.

Consider the conventional shock tube with closed ends (Figs. 1 and 2). (Note that this allows for pressurization or evacuation of the compartments as required, depending on the desired initial pressure ratio $\bar{p}_0/p_0$ across the diaphragm.)

When the diaphragm is ruptured, an unsteady gas motion ensues. An expansion wave (known as a centred rarefaction wave), with its origin 0 at the diaphragm section, is propagated into the gas initially at the higher pressure ; a normal shock wave moves into the gas at rest in the lower pressure compartment with uniform supersonic velocity U. The gas particles in the lower pressure compartment are compressed and acquire a uniform velocity $u(< U)$ in the same direction as the moving shock. This uniform velocity u may be subsonic, sonic or supersonic depending on the initial pressure ratio $\bar{p}_0/p_0$.

At this point, a brief indication of the basic differences between steady and unsteady flow problems may be valuable, since the statement ' an unsteady gas flow can contain a region of uniform velocity ' does not at first seem plausible.

Consider the well-known normal stationary shock-flow pattern, with velocities v_1 and v_2 upstream and downstream of the shock respectively. Fig. 3 shows that this stationary shock system can be changed to an unsteady shock motion by suitable superposition of velocities.

Then $v_1 = U - u_0$ and $v_2 = U - u$, but note that v_1, v_2 are positive in the opposite sense to U, u_0 and u.

In a shock tube, the gas in front of the moving shock is at rest, that is, $u_0 = 0$. Thus

$$U = v_1 \text{ and } u = v_1 - v_2 .$$

Prandtl's equation for the normal stationary shock is

$$v_1 v_2 = a_c^2$$

where a_c is the critical speed of the flow and $v_1 > v_2$. This equation, transformed to the unsteady case, gives

$$U(U - u) = a_c^2; \ U > u ,$$

that is, since U is supersonic $(U - u)$ *must be subsonic,* and hence the unsteady gas motion contains a region of uniform flow of velocity u, *subsonic with respect to the shock velocity U.*

Fig. 2 shows that the shock is reflected on reaching the closed end of the low-pressure section and subsequently moves with a reduced velocity U_R toward the high-pressure section of the tube. It leaves the gas at rest behind it with increased pressure p_R compared with the initial pressure p_0.

Consider now the high-pressure compartment. Here the gas has expanded as a centred rarefaction wave, whose front travels with the local velocity of sound, $\bar{a}_0$, of the high-pressure gas, whilst the velocity and direction of propagation of the rear of this wave depend on the initial pressure ratio across the diaphragm. An expansion wave moving to the left (Fig. 1) into a gas at rest will set the gas particles in motion to the right, that is, in the same direction as the gas flow in the wake of the shock wave. Thus the unsteady gas motion consists of an expansion wave moving to the left and a shock moving to the right, separated by a region of constant velocity flow, subsonic with respect to the shock to the right. With the exception of the acceleration region in the expansion wave, all the gas particles in the shock tube are at rest or in uniform motion to the right. This is clearly shown by Fig. 1.

Since the gas behind the shock has been compressed, its temperature T is higher than T_0; and since the gas behind the rarefaction wave has been expanded, its temperature $\bar{T}$ is lower than $\bar{T}_0$. Consequently, a discontinuity of temperature occurs at those coincident points in the uniform gas flow which were originally on either side of the diaphragm. This 'contact surface' is also propagated into the low-pressure section with a velocity u, since it is evidently not a velocity discontinuity in the uniform flow.

Due to the presence in this flow of the temperature discontinuity, and hence a discontinuity in the speed of sound, the Mach number M of the flow between shock and contact surface will be different from the Mach number $\bar{M}$ of the flow between contact surface and expansion wave.

The reflected front of the rarefaction wave, travelling with sonic speed relative to the flowing gas of velocity u, will overtake the rear of the incident rarefaction wave, the contact surface and the shock in turn, since the flowing gas is subsonic with respect to the shock.

Consider a point in the lower-pressure compartment at a given distance x from the diaphragm. A continuous record of the flow past this point would show:

    (i) A shock moving to the right, with velocity U,
    (ii) A region of uniform 'quasi-steady' flow to the right (velocity u),
    (iii) A temperature (that is, density) discontinuity moving to the right,
    (iv) A further region of uniform quasi-steady flow to the right (velocity u),
    (v) The head of the reflected rarefaction wave moving to the right, and
    (vi) A reflected shock wave moving to the left with velocity U_R.

It is possible to select a particular point for any given initial pressure ratio and shock-tube dimensions so that the contact surface, reflected shock and reflected expansion wave, all arrive at the same instant; this clearly corresponds to the maximum duration τ seconds of the quasi-steady flow between shock and contact surface (point x_2, Fig. 2). Similarly, if the maximum duration $\bar{\tau}$ of quasi-steady flow between contact surface and expansion wave is required, a point is chosen so that the reflected head and the tail of the expansion wave arrive instantaneously (point x_1, Fig. 2). By alteration of the initial pressure ratio across the diaphragm, the desired shock strength or quasi-steady flow Mach number may be obtained; this simple method for obtaining various Mach numbers is the main advantage of the shock tube over the conventional supersonic wind tunnel, which requires different nozzle blocks for each flow Mach number.

Experiments with shock tubes have corroborated that the theoretical wave model described above is correct; indeed, it may be stated that every shock tube has an optimum position in the lower pressure compartment where experimental results agree very nearly with the theoretical predictions. For observation points located nearer to the diaphragm than this optimum position, the shock is not fully plane and has not reached its maximum speed, whilst for observation points located further away from the diaphragm than the optimum position, the shock front is attenuated by the formation of the tube boundary layer and other miscellaneous causes.

The flow behind the contact surface contains particles of the shattered diaphragm and the contact surface itself is a region of temperature gradient and not a true discontinuity in the flow.

In general, however, there is good agreement between theoretical and actual shock-tube flow, especially for initial pressure ratios of less than 100 : 1.

1.3. *History and Uses of the Shock Tube.*—It is informative to trace the history of the shock tube and to note how its use has varied. In the 19th century, interest in the propagation speeds of flame fronts and detonation waves led to the construction of the first shock tube by Vieille[1] in France (1899). He identified detonation waves with shock waves and with a 22 millimetre diameter, 20-ft long tube and high pressure air at 27 atmospheres, he measured shock velocities up to twice the speed of sound in atmospheric air. Despite the success of these experiments, the shock tube was neglected for the next forty years, until Payman and Shepherd[2] produced their classic paper in which they investigated shock-tube flow in some detail. Once again, this work was stimulated by an interest in detonation waves, with particular reference to the problem of safety in mines. Thin sheet copper diaphragms were used in these experiments and the shock tube flow was initiated by suddenly increasing the pressure difference across the diaphragm to a value greater than the static strength of the material. Thus, in any given test, the initial pressure ratio across the diaphragm was not known accurately; however this does not invalidate the comprehensive distance-time history of shock-tube flow which was obtained using a wave-speed camera. The theoretical wave system described above was verified for the first time during these experiments.

Experimental shock-tube work has been carried out in the last decade in the United States and Canada, where initial experiments were made to find a method of blast pressure measurement. It was later realized that shock tubes can be used to investigate compressible flow phenomena, and extensive experiments on the interactions of shocks, rarefactions and contact surfaces were made at Toronto.

These experiments utilized a 'double' shock tube (Fig. 4), having two diaphragms which were punctured simultaneously. Long slit windows in the tube walls and a wave-speed camera were used to obtain a complete x–t history of the flow patterns. Any desired interaction was studied by suitable selection of the pressures p_a, p_b and p_c. For example, the head-on collision of two shock waves was investigated when $p_a > p_b$ and $p_c > p_b$; and the head-on collision of a shock and a rarefaction wave was investigated[3] when $p_a > p_b > p_c$.

Recently (since 1949), the possibilities of using the regions of quasi-steady flow to investigate sub- and supersonic flow about models, that is, using the shock tube as a very short duration aerodynamic tunnel, have been considered theoretically and practically. It will be noted that the shock tube, which was invented at the same time as the wind tunnel (c. 1900) has now developed as a rival to its contemporary.

The shock tube may be used in two distinct ways, as a short duration wind tunnel, or for the study of transient phenomena. In the first case, it has been claimed that the shock tube does not experience choking when model tests at Mach numbers close to unity are being conducted and hence it was thought to be uniquely suited for transonic flow investigations. The development of 'slotted-walls' for transonic flow investigations in conventional wind tunnels has impaired the potential development of the shock tube in this field. Griffith[6] (1952) at Princeton University has obtained steady flow conditions about a 15 deg wedge for a range of Mach numbers from $0 \cdot 86$ to $1 \cdot 16$, and has thus closed the transonic gap in the data obtained from conventional wind tunnels. A Mach-Zehnder interferometer was used to determine the drag coefficients of this wedge, and the results were found to match Liepmann's data at either end of the transonic range, and also to confirm recent theoretical predictions by Vincenti, Cole and Guderley.

Theory shows that an infinite initial pressure ratio $\bar{p}_0/p_0$ across the diaphragm gives a finite upper limit for the Mach number of the flow between shock and contact surface, which, with air as the working fluid in the shock tube, is $M_{\max} = 1 \cdot 73$; whilst in the flow between contact surface and

6

rarefaction wave the Mach number $\bar{M} \to \infty$ as $\bar{p}_0/p_0 \to \infty$. This limitation on M may be overcome by the use of a divergent nozzle in the low-pressure section of the shock tube. Hertzberg[7] (1951) has obtained $M = 4\cdot2$, and, more recently[36, 37], hypersonic flows have been generated in this manner. Liquefaction of the air is not so severe a limitation as in the hypersonic wind tunnel, since the temperature of the expanded flow behind the shock is higher than in the corresponding flow in a conventional wind tunnel. [For the non-expanded flow behind the shock $T > T_0$ (atmospheric), and thus liquefaction of the air cannot occur.] Condensation in the flow may be avoided by thoroughly drying the air used, and since the quantity of air involved is smaller, it is an easier process to dry the air for a shock tube than for a wind tunnel. It seems probable that the hypersonic shock tube will be essential for the study of flows at very high Mach number and at stagnation temperatures of the order of those encountered in free flight. Ultra-high stagnation temperatures may be obtained[36] by employing a combustible mixture of oxygen and hydrogen in the chamber and igniting the mixture at the instant the diaphragm is ruptured. 'Combustion-type' hypersonic shock tubes are under development or active consideration in the United States of America[37] and in the United Kingdom[38].

For the study of transient phenomena, the wind tunnel is, in general, not of use, and it seems probable that this field may be investigated exclusively by the shock tube.

By producing very intense shock waves, relaxation time, ionization and dissociation effects on gas behaviour at high temperatures may be studied. Perry and Kantrowitz[8] (1951), in some preliminary experiments, have observed ionization in argon caused by a converging cylindrical shock, produced by placing a 'teardrop' in a shock tube of circular cross-section, as shown by Fig. 5.

Condensation phenomena in high-speed flow have been observed in a shock tube by Wegener and Lundquist[9] (1951), who used air of known humidity in the high-pressure compartment and electronically detected the presence of water droplets in the flow following the bursting of the diaphragm by the amount of light scatter from the droplets. Apart from fundamental interest, the design of conventional supersonic wind tunnels should benefit from this work.

At present, only optical methods of flow analysis are applicable to the shock tube, but if a technique can be developed to measure directly the transient forces on a model, the shock tube may compete with the conventional supersonic tunnel as the premier tool of aerodynamic research. Whatever future developments in technique may be, the shock tube offers the most economical way of demonstrating and investigating a large variety of steady and unsteady phenomena.

CHAPTER 2

Fundamental Theory of Ideal One-dimensional Wave Motion

2.1. *Basic Equations for Unsteady Compressible Flow in Tubes.*—Consider the unsteady flow of a compressible gas which can be described by one local Cartesian co-ordinate x and for which friction and heat conduction can be neglected (that is, $\mu = k = 0$). The flow in a tube of cross-sectional area A in the direction of x satisfies the above conditions if the state of the flow in each cross-section can be considered uniform.

Suppose the cross-section A of the tube can depend on the distance from a given datum x and the time t, that is, $A = A(x, t)$, then the unsteady compressible flow of gas in the tube is described by the differential equations :—

Eulers Equation of Motion

$$\frac{\partial u}{\partial t} + u\frac{\partial u}{\partial x} + \frac{1}{\rho}\frac{\partial p}{\partial x} = 0 \qquad \cdots \quad \cdots \quad \cdots \quad \cdots \quad \cdots \quad \cdots \quad (2.1)$$

The Equation of Continuity

$$\frac{\partial}{\partial t}(\rho A) + \frac{\partial}{\partial x}(\rho u A) = 0 \quad \ldots \quad \ldots \quad \ldots \quad \ldots \quad \ldots \quad \ldots \quad (2.2)$$

The Entropy Equation

$$\frac{\partial s}{\partial t} + u\frac{\partial s}{\partial x} = 0 \quad \ldots \quad \ldots \quad \ldots \quad \ldots \quad \ldots \quad \ldots \quad (2.3)$$

The Equation of State

$$\rho = \rho(s,p) \quad \ldots \quad \ldots \quad \ldots \quad \ldots \quad \ldots \quad (2.4)$$

Equation (2.2) may be rewritten as

$$\frac{\partial}{\partial x}(\rho u) + \frac{\partial \rho}{\partial t} = -\rho\left\{\frac{\partial(\log_e A)}{\partial t} + u\frac{\partial(\log_e A)}{\partial x}\right\} \quad \ldots \quad \ldots \quad (2.5)$$

2.2. *The Methods of Characteristics.*—In 1892 Riemann solved the equations (2.1) to (2.4) for the case of a perfect gas with $s =$ constant and $A =$ constant, and later with $A = A(x, t)$. After the development of the 'Methods of Characteristics' by Schutze-Grunau, Guderley, Sauer and Döring (c. 1940) there is little practical interest in the 'exact' solutions of the differential equations (2.1) to (2.4), since every technical problem may be solved by the approximative methods. However, 'exact' solutions, such as that for the conventional shock-tube problem, are useful as test cases to check the accuracy of the 'characteristics' solution.

2.2.1. *Characteristics and Life Curves.*—Sound waves are propagated relative to a gas with the local speed of sound a according to the equation

$$a^2 = \left(\frac{\partial p}{\partial \rho}\right)_{s=\text{const}} \quad \ldots \quad \ldots \quad \ldots \quad \ldots \quad \ldots \quad (2.6)$$

If a gas is flowing with velocity $u(> 0)$ in the direction of increasing x, then a sound wave moving upstream has an inclination $\frac{dx}{dt} = u - a$ at every point of the (x, t)-plane, whereas a sound wave moving downstream has an inclination $\frac{dx}{dt} = u + a$. These curves can be continuously differentiated and are called 'characteristic basic curves' or 'characteristics'. The curve $C_+ \left(\frac{dx}{dt} = u + a\right)$ is called 'running to the left', and the curve $C_- \left(\frac{dx}{dt} = u - a\right)$ is called 'running to the right', since they pass on the left and right respectively of the 'life curve' or 'particle path' $\frac{dx}{dt} = u$ (*see* Fig. 6). Hence we see that the characteristics are those curves along which sound waves spread after they are produced. Moreover, the characteristics are also defined in a gas at rest, where they form a network of two families of curves covering the entire flow field.

2.2.2. *Conditions of Compatibility.* The differential equations (2.1) to (2.4) of the flow may be transformed to use the characteristics as co-ordinate curves. From (2.5) and (2.6) we have

$$\frac{1}{a^2}\left\{\frac{\partial p}{\partial t} + u\frac{\partial p}{\partial x}\right\} + \rho\frac{\partial u}{\partial x} = -\rho\left\{\frac{\partial(\log_e A)}{\partial t} + u\frac{\partial(\log_e A)}{\partial x}\right\} \quad \ldots \quad \ldots \quad (2.7)$$

Then, from (2.1) and (2.7) we obtain by addition,

$$\left\{\frac{\partial u}{\partial t} + (u + a)\frac{\partial u}{\partial x}\right\} + \frac{1}{\rho a}\left\{\frac{\partial p}{\partial t} + (u + a)\frac{\partial p}{\partial x}\right\} = -a\left\{\frac{\partial(\log_e A)}{\partial t} + u\frac{\partial(\log_e A)}{\partial x}\right\} \quad \ldots \quad (2.8)$$

and, by subtraction

$$\left\{\frac{\partial u}{\partial t} + (u - a)\frac{\partial u}{\partial x}\right\} - \frac{1}{\rho a}\left\{\frac{\partial p}{\partial t} + (u - a)\frac{\partial p}{\partial x}\right\} = +a\left\{\frac{\partial(\log_e A)}{\partial t} + u\frac{\partial(\log_e A)}{\partial x}\right\} \quad \ldots \quad (2.9)$$

8

Since $\dfrac{\partial u}{\partial x} \cdot \dfrac{dx}{dt} + \dfrac{\partial u}{\partial t} = \dfrac{du}{dt}$ and $\dfrac{\partial p}{\partial x} \cdot \dfrac{dx}{dt} + \dfrac{\partial p}{\partial t} = \dfrac{dp}{dt}$, these equations may be written as :—

along the C_+ characteristic, $\left(\dfrac{dx}{dt} = u + a\right)$,

$$\frac{du}{dt} + \frac{1}{\rho a} \frac{dp}{dt} = - a \left\{ \frac{\partial (\log_e A)}{\partial t} + u \frac{\partial (\log_e A)}{\partial x} \right\} \qquad .. \qquad .. \qquad (2.10)$$

and along the C_- characteristic, $\left(\dfrac{dx}{dt} = u - a\right)$,

$$\frac{du}{dt} - \frac{1}{\rho a} \frac{dp}{dt} = + a \left\{ \frac{\partial (\log_e A)}{\partial t} + u \frac{\partial (\log_e A)}{\partial x} \right\} . \qquad .. \qquad (2.11)$$

2.2.3. *Special Cases.*—Now consider the unsteady compressible flow in a tube of a perfect gas with constant specific heats. The Equation of State (2.4) becomes

$$\frac{p}{p_0} = \left(\frac{\rho}{\rho_0}\right)^\gamma . e^{\frac{s - s_0}{c_v}} . \qquad .. \qquad .. \qquad .. \qquad .. \qquad (2.12)$$

Introduce non-dimensional quantities by using a reference state (suffix $_0$), for example :—

$$\bar{u} = \frac{u}{a_0} ; \quad \bar{a} = \frac{a}{a_0} ; \quad \bar{\rho} = \frac{\rho}{\rho_0} ; \quad \bar{p} = \frac{p}{p_0} ; \quad \bar{s} = \frac{s}{c_v} ; \quad \bar{T} = \frac{T}{T_0} ; \quad t = \frac{a_0}{x_0} . t \text{ and } \bar{X} = \frac{x}{x_0} ,$$

and immediately drop the $^-$ sign. Confusion is avoided since X appears in the equations. Then, from (2.6) $a^2 = \dfrac{\gamma p}{\rho}$, from (2.12) $p = \rho^\gamma e^{s - s_0}$, and on differentiation and combination we obtain $\dfrac{dp}{\rho a} = \dfrac{2da}{\gamma - 1} - \dfrac{ads}{\gamma(\gamma - 1)}$. Further, write $ds' = \dfrac{ds}{\gamma(\gamma - 1)}$ and then equations (2.10) and (2.11) become

$$\frac{du}{dt} \pm \frac{2}{\gamma - 1} \cdot \frac{da}{dt} = \mp a \left[\frac{ds'}{dt} - \left\{ \frac{\partial (\log_e A)}{\partial t} + u \frac{\partial (\log_e A)}{\partial X} \right\} \right] . \qquad .. \qquad .. \qquad (2.13)$$

If we restrict the analysis to tubes of constant cross-section and to flows involving no entropy changes, i.e., $A = $ constant and $s = $ constant, the right-hand sides of equations (2.13) vanish and the equations become on integration

$$u + \frac{2}{\gamma - 1} a = \text{constant along a } C_+ \text{ characteristic } \left(\frac{dx}{dt} = u + a\right) \text{ and}$$

$$u - \frac{2}{\gamma - 1} a = \text{constant along a } C_- \text{ characteristic } \left(\frac{dx}{dt} = u - a\right) . \qquad .. \qquad (2.14)$$

The equations (2.14) are the 'basic statements' of the method of characteristics for one-dimensional, unsteady, isentropic, compressible flow and from these equations can be derived the special formulae applicable to any type of simple wave motion

$$\left(\text{examples}: \begin{array}{ccc} \text{(ordinary)} & \text{(forward facing)} & \text{(rarefaction)} \\ \text{(centred)} & \text{(backward facing)} & \text{(compression)} \end{array} \text{waves}\right).$$

Reference 10 gives a complete account of this work: here it is sufficient to consider in detail the one simple wave formed in the shock tube, namely, the centred rarefaction wave propagated into the gas initially at the higher pressure. Fig. 2 shows that the principal shock is taken to travel in the direction of increasing X; consequently, the principal expansion wave is propagated in the

9

negative X direction, *i.e.*, it is a 'backward-facing' centred rarefaction wave. Now the 'constants' in equations (2.14) are termed the Riemann invariants and are denoted by

$$2r^* = u + \frac{2a}{\gamma - 1} \ (C_+ \text{ characteristics}) \text{ and } -2s^* = u - \frac{2a}{\gamma - 1} \ (C_- \text{ characteristics}) \ . \ .. \quad (2.14a)$$

It is shown in Reference 10, pp. 59–62, that there exist three types of solution of the characteristic equations (2.14).

    (*a*) If $r^* = $ constant AND $s^* = $ constant—a steady state exists.

    (*b*) If $r^* \neq $ constant AND $s^* \neq $ constant—a general flow exists.

    (*c*) If $r^* = $ constant OR $s^* = $ constant—a simple wave exists and one set of characteristics is straight lines. In particular (Reference 10, pp. 92–93), if $s^* = $ constant then the C_+ characteristics are straight lines and the wave is 'forward facing', or, again, if $r^* = $ constant (that is, $u + \dfrac{2a}{\gamma + 1} = $ constant *throughout* a simple wave region) then the C_- characteristics are straight lines and the wave is 'backward facing'.

    It follows that for the shock tube case the C_- characteristics radiate from the origin O (*see* Fig. 7) and that the equations (2.14) become,

$$\bar{u} + \frac{2}{\gamma - 1} \cdot \bar{a} = \frac{2}{\bar{\gamma} - 1} \ ; \ \frac{dX}{dt} = \bar{u} + \bar{a} \text{ for the } C_+ \text{ characteristics} \qquad .. \qquad .. \quad (2.15)$$

and

$$\bar{u} + \frac{2}{\bar{\gamma} - 1} \cdot \bar{a} = \frac{2}{\bar{\gamma} - 1} \ ; \ \frac{X}{t} = \bar{u} - \bar{a} \text{ for the } C_- \text{ characteristics} \qquad .. \qquad .. \quad (2.16)$$

where the superscript $^-$ refers to the gas initially at the higher pressure in the shock tube.

    From equations (2.16), by putting $\dfrac{\bar{u}}{\bar{a}} = \bar{M}$ and noting that

$$\bar{a} = \bar{p}^{\frac{\bar{\gamma}-1}{2\bar{\gamma}}} = \bar{T}^{1/2} = \bar{\rho}^{\frac{\bar{\gamma}-1}{2}} \ ,$$

by virtue of equation (2.12) for a perfect gas with constant entropy, we have

$$\bar{a} = \frac{\bar{u}}{\bar{M}} = \bar{p}^{\frac{\bar{\gamma}-1}{2\bar{\gamma}}} = \frac{1}{1 + \dfrac{\bar{\gamma}-1}{2}\bar{M}} \qquad .. \qquad .. \qquad .. \qquad .. \qquad .. \quad (2.17)$$

and

$$\frac{X}{t} = \bar{u} - \bar{a} = \frac{\bar{M}-1}{1 + \dfrac{\bar{\gamma}-1}{2}\bar{M}} \ . \qquad .. \qquad .. \qquad .. \qquad .. \qquad .. \quad (2.18)$$

    Note.—In the above non-dimensional equations (2.15) to (2.18)

$$\bar{u} = \frac{\bar{u}}{\bar{a}_0} \ ; \quad \bar{a} = \frac{\bar{a}}{\bar{a}_0} \ ; \quad \bar{p} = \frac{\bar{p}}{\bar{p}_0} \ ; \quad t = \frac{a_0 t}{|\bar{x}_0|} \text{ and } X = \frac{x}{|\bar{x}_0|} \ .$$

These symbols represent the preceding non-dimensional notation adapted for the shock tube. The relations $X = \dfrac{x}{|\bar{x}_0|}$, $t = \dfrac{\bar{a}_0 t}{|\bar{x}_0|}$, require the 'modulus' sign, since x_0 is a negative quantity (*see* Fig. 2).

---

    * s^* is not to be confused with entropy s.

2.3. *The Normal Shock Equations.*—It has been shown that unsteady shock motion can be reduced to a stationary shock by suitable superposition of velocities (*see* Fig. 3) and we may thus analyse the unsteady flow in the classical manner.

The usual conservation equations for the stationary shock become, on transformation to the shock-tube notation,

Continuity
$$\rho_0(U - u_0) = \rho(U - u) \quad .. \qquad .. \qquad .. \qquad .. \qquad .. \qquad (2.19)$$

Momentum
$$p_0 + \rho_0(U - u_0)^2 = p + \rho(U - u)^2 \quad .. \qquad .. \qquad .. \qquad .. \qquad (2.20)$$

Energy
$$\frac{\gamma}{\gamma - 1} \cdot \frac{p_0}{\rho_0} + \frac{(U - u_0)^2}{2} = \frac{\gamma}{\gamma - 1} \cdot \frac{p}{\rho} + \frac{(U - u)^2}{2} \quad .. \qquad .. \qquad .. \qquad (2.21)$$

Further, the equation of state for a perfect gas is

$$p = \rho RT \qquad .. \qquad .. \qquad .. \qquad .. \qquad .. \qquad (2.22)$$

and equation (2.12) is also valid.

From the equations (2.19) to (2.22) we may derive the following useful non-dimensional relations for the changes of parameters of state across the shock wave.

Prandtl's Equation
$$\frac{(U - u_0)(U - u)}{a_c{}^2} = 1 \quad .. \qquad .. \qquad .. \qquad .. \qquad .. \qquad .. \qquad (2.23)$$

$$\frac{p}{p_0} = \frac{2\gamma}{\gamma + 1}\left(\frac{U - u_0}{a_0}\right)^2 - \frac{\gamma - 1}{\gamma + 1} \qquad .. \qquad .. \qquad (2.24)$$

$$\frac{p_0}{p} = \frac{2\gamma}{\gamma + 1}\left(\frac{U - u}{a}\right)^2 - \frac{\gamma - 1}{\gamma + 1} \qquad .. \qquad .. \qquad (2.25)$$

$$\frac{2}{\gamma + 1} \cdot \frac{a_0}{u}\left(\frac{U - u_0}{a_0} - \frac{a_0}{U - u_0}\right) = \frac{2}{\gamma + 1} \cdot \frac{a}{u}\left(\frac{a}{U - u} - \frac{U - u}{a}\right) = 1 \quad .. \qquad (2.26)$$

$$\left(\frac{a}{a_0}\right)^2 = \frac{T}{T_0} = \frac{\left\{\gamma\left(\frac{U}{a_0}\right)^2 - \frac{\gamma - 1}{2}\right\}\left\{\frac{\gamma - 1}{2}\left(\frac{U}{a_0}\right)^2 + 1\right\}}{\left(\frac{\gamma + 1}{2}\right)^2\left(\frac{U}{a_0}\right)^2} \qquad .. \qquad (2.27)$$

Rankine-Hugoniot Equation
$$\frac{\rho}{\rho_0} = \frac{\dfrac{p_0}{p} + \dfrac{\gamma + 1}{\gamma - 1}}{\left(\dfrac{\gamma + 1}{\gamma - 1}\right)\dfrac{p_0}{p} + 1} \quad ... \qquad .. \qquad .. \qquad .. \qquad (2.28)$$

In the shock tube, the gas ahead of the advancing shock is at rest, i.e., $u_0 = 0$, and equations (2.23), (2.24) and (2.26) simplify accordingly.

Typical values of the variations of the parameters of state across a normal shock wave were calculated for the shock tube from equation (2.23) to (2.28) and are given in Tables. 1 and 2.

CHAPTER 3

Application of the Basic Theory to the Shock Tube

3.1. *Ideal Unsteady Gas Motion in an Infinite Shock Tube (Fig. 8).*—In the following theory, the assumptions made are :—

(1) the flow is exactly one-dimensional,

(2) heat conductivity and viscosity can be neglected,

(3) the gases used obey the perfect gas equation of state (2.22) and have constant specific heats,

(4) the thin, plane diaphragm is instantaneously removed,

(5) the shock tube is rigid

(6) the initial temperatures of the higher and lower pressure gases are equal, and

(7) the concept of a non-conducting contact surface is justified.

Since the conventional shock tube uses air as its working fluid, the theory to be developed assumes $\gamma = \bar{\gamma} = 1 \cdot 4$ and $T_0 = \bar{T}_0$, whence $a_0 = \bar{a}_0$.

By combining the equations of motion of a centred rarefaction wave and of a normal shock, so as to satisfy the conditions at the contact surface (at which the pressure and velocity of both gases are equal, that is $u = \bar{u}$ and $p = \bar{p}$), we may determine the unsteady gas motion in terms of the initial pressure ratio across the diaphragm, $\bar{p}_0/p_0$, the Mach numbers M and $\bar{M}$ of the quasi-steady flow behind the shock and the contact surface respectively, or the strength of the shock p/p_0.

For convenience, write $P = \bar{p}_0/p_0$, $p_s = p/p_0$ and $V_+ = \dfrac{U}{a_0}$.

Then, from equations (2.17) and (2.26) we have, with $\gamma = \bar{\gamma} = 1 \cdot 4$, $u = \bar{u}$ and $p = \bar{p}$ at the contact surface,

$$P = \frac{1}{6} \left\{ 7V_+^2 - 1 \right\} \left\{ 1 - \frac{1}{6}\left(V_+ - \frac{1}{V_+} \right) \right\}^{-7} . \qquad \cdot \cdot \qquad \cdot \cdot \qquad \cdot \cdot \qquad (3.1)$$

From equations (2.26) and (2.27), with $u_0 = 0$ and $\gamma = 1 \cdot 4$, we have

$$M = \frac{u}{a_0} \cdot \frac{a_0}{a} = 5 \left[V_+^2 - 1 \right] \left\{ \left[7V_+^2 - 1 \right] \left[V_+^2 + 5 \right] \right\}^{-1/2} . \qquad \cdot \cdot \qquad (3.2)$$

Again, from equations (2.17) and (2.26), with $u = \bar{u}$, $u_0 = 0$ and $\gamma = \bar{\gamma} = 1 \cdot 4$, we have

$$\frac{6\bar{M}}{5 + \bar{M}} = V_+ - \frac{1}{V_+} .$$

Finally, from equation (2.24),

$$p_s = \frac{1}{6} \left[7V_+^2 - 1 \right] . \qquad \cdot \cdot \qquad \cdot \cdot \qquad \cdot \cdot \qquad \cdot \cdot \qquad \cdot \cdot \qquad \cdot \cdot \qquad (3.4)$$

Thus for a given shock speed V_+ all the other quantities involved in the shock-tube flow, namely P, M, $\bar{M}$ and p_s may be theoretically determined from equations (3.1) to (3.4). Calculated values are shown in Table 2.

3.2. *Effect of Boundary Conditions on the Gas Motion.*—In Chapter 1, Section 1.2 a qualitative discussion was given of the effects on the quasi-steady flow durations of the reflection of the normal shock and the centred rarefaction wave from the closed ends of the conventional shock tube. In the following Sections these effects are considered in detail, and again the analysis is confined to the case when $\gamma = \bar{\gamma} = 1 \cdot 4$ and $T_0 = \bar{T}_0$.

3.2.1. *Reflection of the Shock.*—Fig. 9 shows the conditions applicable to the reflection of the shock from the closed end of the lower-pressure section. The air ahead of the incident shock is at rest, as is the air behind the reflected shock. Equation (2.26) gives the quadratic

$$\left(\frac{U-u}{a}\right)^2 + \frac{\gamma+1}{2}\cdot\frac{u}{a}\left(\frac{U-u}{a}\right) - 1 = 0 \qquad .. \qquad .. \qquad .. \qquad (3.5)$$

which is satisfied by both the incident shock U and the reflected shock U_R, but note that U_R is positive in the opposite direction to U.

From (3.5)

$$\left(\frac{U-u}{a}\right)\left(\frac{U_R-u}{a}\right) = -1 \text{ and } U + U_R = \frac{3-\gamma}{2}\cdot u$$

or

$$\left|\frac{U_R}{U}\right| = \frac{3-\gamma}{2}\cdot\frac{u}{U} - 1\,.$$

Since $\dfrac{U}{a_0} = V_+$, we may write $\left|\dfrac{U_R}{a_0}\right| = V_-$ and $v_+ = \dfrac{u}{a_0}$.

Again from (2.26) with $\gamma = 1\cdot4$,

$$\frac{v_+}{V_+} = \frac{5}{6}\left\{1 - \frac{1}{V_+^2}\right\}. \qquad .. \qquad .. \qquad .. \qquad .. \qquad .. \qquad (3.6)$$

Hence, finally,

$$\frac{V_-}{V_+} = \frac{1}{3}\left\{1 + \frac{2}{V_+^2}\right\}. \qquad .. \qquad .. \qquad .. \qquad .. \qquad .. \qquad (3.7)$$

The maximum duration τ of quasi-steady flow behind the incident shock occurs at a section distant X_2 from the diaphragm ($X = 0$). If X_0 is the length of the lower-pressure compartment —the channel—and X_2 the position where the reflected shock meets the contact surface, we obtain the following equations for τ and X_2 (*see* Fig. 9 and Appendix A1),

$$\frac{X_0}{X_2} = \frac{\dfrac{V_+}{v_+} + \dfrac{V_+}{V_-}}{1 + \dfrac{V_+}{V_-}} \qquad .. \qquad .. \qquad .. \qquad .. \qquad .. \qquad .. \qquad (3.8)$$

and

$$\frac{X_0}{\tau} = \frac{\left(\dfrac{V_-}{V_+}\right)V_+}{\dfrac{V_-}{V_+} + 1} + \frac{V_+}{\dfrac{V_+}{v_+} - 1} \qquad .. \qquad .. \qquad .. \qquad .. \qquad (3.9)$$

where

$$X_0 = \frac{x_0}{|\bar{x}_0|}\,, \quad \tau = t_2 - t_s\,.$$

Equations (3.8) and (3.9) may be evaluated for the series of values of V_+ given by Table 2 by using relations (3.6) and (3.7). Specimen values of these parameters are given in Table 3.

3.2.2. *The Path of the Head of the Reflected Rarefaction Wave.*—Consider the motion of the incident backward-facing centred rarefaction wave in the (t, X)-plane. (*See* Fig. 7.) The head of this wave travels with the local velocity of sound of the higher-pressure gas, whilst the velocity and direction of propagation of the tail of this wave depend on the initial pressure ratio across the diaphragm, situated at $X = 0$. Thus, for the head of the wave (characteristic C_-^H), from (2.16), we have

$$\frac{X}{t} = -1\,.$$

If the closed end of the higher-pressure chamber of the shock tube is located at $X = -1$, then the 't' co-ordinate for the point where the head of the incident wave is reflected must be $t = 1$.

13

The reflected front of the rarefaction wave advances with sonic speed relative to the flowing gas (*i.e.*, along characteristic C_+^H), and will meet or will overtake the tail of the incident rarefaction wave, the contact surface and the shock in turn, since the flowing gas is subsonic with respect to the shock.

The flow region bounded by the shock, the incident head (C_-^H) and the reflected head (C_+^H) of the centred rarefaction wave may be determined completely by solving equation (2.15) for the characteristic C_+^H through the point $(1, -1)$ of the (t, X)-plane, where the flow parameters through the incident rarefaction wave are given by equation (2.16). The variations of the parameters of state in this flow region are given by the following equations, which are derived in Appendix A2.

$$X = 5t - 6t^{2/3} \qquad .. \qquad .. \qquad .. \qquad .. \qquad .. \qquad .. \qquad (3.10)$$

$$t = \left(1 + \frac{\bar{M}}{5}\right)^3 \qquad .. \qquad .. \qquad .. \qquad .. \qquad .. \qquad .. \qquad (3.11)$$

$$X = (\bar{M} - 1)\left(1 + \frac{\bar{M}}{5}\right)^2 . \qquad .. \qquad .. \qquad .. \qquad .. \qquad (3.12)$$

Equations (3.10) to (3.12) hold for all values of $\bar{M}$, and this parameter is the most convenient to use in the subsequent analysis.

3.2.3. *The Quasi-Steady Flow behind the Contact Surface.*—When $\bar{M} < 1$, the entire rarefaction wave is propagated into the higher-pressure compartment only (*see* Fig. 10), but when $\bar{M} > 1$, the tail of the rarefaction wave is propagated into the lower-pressure compartment (*see* Fig. 11). Mathematically, we have for the tail of the rarefaction wave, characteristic C_-^T, Fig. 7, equation (2.16),

$$\frac{dX}{dt} = \frac{X}{t} = \bar{u} - \bar{a} = \bar{a}(\bar{M} - 1) .$$

That is, the C_-^T characteristic has

a positive slope if $\bar{M} > 1$ (Fig. 11)

a negative slope if $\bar{M} < 1$ (Fig. 10)

and   a zero slope if $\bar{M} = 1$.

Figs. 10 and 11 clearly show that the maximum duration $\bar{\tau}$ of quasi-steady flow behind the contact surface is affected by the direction of propagation of the tail of the centred rarefaction wave, and hence by $\bar{M}$, the Mach number of the quasi-steady flow. We must therefore consider two cases of shock-tube flow when the quasi-steady flow behind the contact surface is (1) subsonic and (2) supersonic.

3.2.3.1. *Case* (1) $\bar{M} < 1$ (*Fig.* 10).—The maximum duration $\bar{\tau}$ of the quasi-steady flow behind the contact surface is given by

$$\bar{\tau} = \frac{2\beta^3}{1 + \bar{M}} \qquad .. \qquad .. \qquad .. \qquad .. \qquad .. \qquad .. \qquad (3.13)$$

where $$\beta = \left(1 + \frac{\bar{M}}{5}\right) .$$

This maximum duration $\bar{\tau}$ occurs at the diaphragm section when $\bar{M} < 1$. There is zero flow duration at X_1 and X_2 and linear variation between these two points and the position $X = 0$. The positions X_1 and X_2 are given by

$$X_1 = (\bar{M} - 1)\beta^2 \qquad .. \qquad .. \qquad .. \qquad .. \qquad .. \qquad .. \qquad (3.14)$$

and $$X_2 = 2\bar{M}\beta^2 \qquad .. \qquad .. \qquad .. \qquad .. \qquad .. \qquad .. \qquad (3.15)$$

14

The points B (t_1, X_1) and C (t_2, X_2), Fig. 10, have 't' co-ordinates given by

$$t_2 = 2t_1 = 2\beta^3 . \quad .. \qquad .. \qquad .. \qquad .. \qquad .. \qquad .. \qquad (3.16)$$

Equations (3.13) to (3.16) are developed in detail in Appendix A3.

3.2.3.2. *Case* (2) $\bar{M} > 1$ (*Fig. 11*).—The maximum duration $\bar{\tau}$ now occurs at section X_1 and is given by

$$\tau = \frac{\beta^3}{\bar{M}} . \quad .. \qquad .. \qquad .. \qquad .. \qquad .. \qquad .. \qquad .. \qquad (3.17)$$

There is zero flow duration at the diaphragm section ($X = 0$) and at section X_2, and linear variation between these two points and the position X_1. Equations (3.14) to (3.16) give the (t, X) co-ordinates of B (t_1, X_1) and C (t_2, X_2) as before.

Equation (3.17) is also derived in Appendix A3. [Note that when $\bar{M} = 1$, both equations (3.12) and (3.17) give

$$\bar{\tau} = \beta^3 = \tfrac{1}{2}t_2 = t_1 ,$$

corresponding to point B lying on the t-axis.]

Table 4 gives specimen values of X_1, X_2, t_1, t_2 and $\bar{\tau}$, calculated from equations (3.13) to (3.17) for the range of $\bar{M}$ values specified by Table 2.

3.3. *Correlation of Criteria for Maximum Quasi-steady Flow Durations.*—In the preceding Section, the factors which influence the maximum durations of quasi-steady flow behind both shock and contact surface have been determined.

By imposing one additional condition on the flow, namely, that the reflected shock, contact surface and head of the reflected rarefaction wave should meet at point C (t_2, X_2), we may combine the results of Section 3.2 to give an overall picture of the flow occurring in a conventional shock tube with closed ends (*see* Fig. 12).

Consider a shock tube having a lower-pressure compartment of length x_0 (non-dimensional length X_0) and a higher-pressure compartment of length $\bar{x}_0$ (non-dimensional length unity). To obtain the maximum duration τ of quasi-steady flow behind the shock the test section must be situated at position X_2, whilst for maximum duration $\bar{\tau}$ of the flow behind the contact surface the test section must be placed at position X_1.

In the latter case, when studies are being conducted in the flow behind the contact surface, we may utilize a shorter lower-pressure compartment of length X_0' (*see* Fig. 12), since, by ensuring the reflected shock wave U_R' meets the contact surface at the same instant (*i.e.*, time t_1) as the reflected head of the rarefaction wave overtakes the tail of the incident wave, we have eliminated any need to study the interaction of the reflected shock with the contact surface.

It then follows directly from Fig. 12, by the properties of similar triangles, that

$$X_0' = \tfrac{1}{2}X_0$$
$$X_2' = \tfrac{1}{2}X_2 \quad .. \qquad .. \qquad .. \qquad .. \qquad .. \qquad .. \qquad .. \qquad (3.18)$$

and

$$\tau' = \tfrac{1}{2}\tau$$

since U_R' is parallel to U_R and $t_2 = 2t_1$ (equation (3.16)). We may also derive (*see* Appendix A4), an explicit relation for $\tau/\bar{\tau}$. This is

$$\frac{\tau}{\bar{\tau}} = (1 + \bar{M}) \left[1 - \left(\frac{5\bar{M}}{5 + \bar{M}} \right) \frac{1}{V_+} \right] \text{ for } \bar{M} < 1 \qquad .. \qquad (3.19)$$

and

$$\frac{\tau}{\bar{\tau}} = 2\bar{M} \left[1 - \left(\frac{5\bar{M}}{5 + \bar{M}} \right) \frac{1}{V_+} \right] \text{ for } \bar{M} > 1$$

where the corresponding values of $\bar{M}$ and V_+ are given by Table 2.

CHAPTER 4

A Rapid Method for the Calculation of the Performance of a Conventional Shock Tube

The equations governing shock-tube flow are of a complex algebraic nature and exhibit a multiplicity of parameters of state. Hence although it is possible to present shock-tube performance in many differing ways, certain parameters have much more practical importance than the remainder. In the preceding chapters the writer has attempted to develop the theory in a concise manner, using only the parameters which are amenable to simple experimental verification. These parameters are:—

(i) the initial pressure ratio P across the diaphragm, measurable by conventional pressure gauges,

(ii) the shock speed V_+, measurable by electronic equipment to be described in a later chapter,

(iii) the quasi-steady flow Mach numbers M and $\bar{M}$, determinable from photographs of the flow field around various models, and

(iv) the positions X_1, X_2 and the maximum durations τ and $\bar{\tau}$ of the quasi-steady flows, which may be verified by timed photographs of the flow.

When the shock tube is used as a short-duration wind tunnel, the Reynolds numbers of the quasi-steady flows are also of interest.

For certain shock-tube applications, for example, the study of ionization of gases in the high temperature region behind the reflected shock V_-, other parameters may become of prime importance. These parameters can be brought into the equations by algebraic manipulation as required.

4.1. *Calculation of Values.*—For the shock-tube installation to be described, the ultimate available pressure ratio across the diaphragm will not exceed 20,000 : 1, corresponding to high-pressure air in the chamber at 200 lb per square in., and a vacuum of $0\cdot5$ mm of mercury in the channel. At large pressure ratios P, the assumption that the specific heat ratio γ is a constant is invalid due to the high temperature generated behind the shock. However, even at $P = 20,000$, these effects amount to less than a 2 per cent error in the shock speed V_+ and may be neglected. As before, we assume $\gamma = \bar{\gamma} = 1\cdot4$, $T_0 = \bar{T}_0 = 288°\mathrm{K}$, $a_0 = \bar{a}_0 = 1{,}118$ ft/sec.

4.1.1. *Quasi-steady Flow Reynolds Numbers.*—Table 2 gives values of M and $\bar{M}$ calculated for given V_+ from equations (3.2) and (3.3) respectively. At the contact surface $u = \bar{u}$, $p = \bar{p}$ and hence equation (2.22) for a perfect gas gives

$$\frac{p}{\bar{p}} \cdot \frac{\bar{\rho}}{\rho} = \frac{RT}{R\bar{T}} \quad \text{or} \quad \frac{\bar{\rho}}{\rho} = \frac{T}{\bar{T}} \cdot \qquad \qquad \qquad \qquad \qquad (4.1)$$

Further, $a = \sqrt{(\gamma RT)}$ and $M = \dfrac{u}{a}$, hence

$$\frac{a}{\bar{a}} = \frac{a}{u} \cdot \frac{\bar{u}}{\bar{a}} = \frac{\bar{M}}{M} = \sqrt{\frac{T}{\bar{T}}} \cdot \qquad \qquad \qquad \qquad (4.2)$$

Combining (4.1) and (4.2) we have

$$\frac{\bar{M}}{M} = \frac{a}{\bar{a}} = \sqrt{\frac{T}{\bar{T}}} = \sqrt{\frac{\bar{p}}{\rho}} \cdot \qquad \qquad \qquad \qquad (4.3)$$

It is convenient to use the term Reynolds number per foot when discussing the character of the quasi-steady flows in the shock tube. We then define:—

$$[Re]_M = \frac{\rho u}{\mu} \text{ and } [Re]_{\bar{M}} = \frac{\bar{\rho}\bar{u}}{\bar{\mu}} \qquad \qquad \qquad \qquad (4.4)$$

The variation of viscosity with temperature will be taken as

$$\frac{\mu}{\mu_0} = \left(\frac{T}{T_0}\right)^{3/4} \qquad \cdots \qquad \cdots \qquad \cdots \qquad \cdots \qquad \cdots \qquad (4.5)$$

where suffix $_0$ corresponds to some reference state.

Then, *see* Appendix A5, we may derive

$$\frac{[Re]_{\bar{M}}}{[Re]_M} = \left(\frac{\bar{M}}{M}\right)^{7/2} \qquad \cdots \qquad \cdots \qquad \cdots \qquad \cdots \qquad \cdots \qquad (4.6)$$

also

$$[Re]_{\bar{M}} = 484{,}848\, \bar{p}_0\, \bar{M} \left(1 + \frac{\bar{M}}{5}\right)^{-9/2} \cdots \qquad \cdots \qquad \cdots \qquad \cdots \qquad (4.7)$$

where $\bar{p}_0$ is expressed in pounds per square inch absolute.

Table 5 gives specimen values of $\dfrac{\bar{M}}{M}, \dfrac{a}{\bar{a}}, \dfrac{T}{\bar{T}}, \dfrac{\rho}{\bar{\rho}}$ and $\dfrac{[Re]_{\bar{M}}}{[Re]_M}$ calculated from equations (4.3) and (4.6) for the range of M and $\bar{M}$ values specified by Table 2.

Equation (4.7) yields the interesting fact that the Reynolds number attainable with a given chamber pressure $\bar{p}_0$ has a maximum value when $\underline{\bar{M} = 1\cdot429}$. Then $[Re]_{\bar{M}\,\text{max}} = 223{,}600\bar{p}_0$ where $\bar{p}_0$ is measured in pounds per square inch absolute.

When $\bar{M} = 1\cdot429$, $M = 0\cdot883$, but this does not correspond to a maximum value of $[Re]_M$. Due to the algebraic complexity of the shock-tube equations the present writer has been unable to develop a direct equation to find the maximum value, $[Re]_{M\,\text{max}}$; but, by combining equations (4.6) and (4.7), we may plot the relation

$$[Re]_M = 484{,}848\, \bar{p}_0\, \bar{M} \left(1 + \frac{\bar{M}}{5}\right)^{-9/2} \cdot \left(\frac{\bar{M}}{M}\right)^{-7/2} \cdot \qquad \cdots \qquad \cdots \qquad (4.8)$$

We may then directly determine the $\bar{M}$ value corresponding to $[Re]_{M\,\text{max}}$. This is $\bar{M} = 0\cdot465$, and corresponds to $M = 0\cdot391$. The numerical value of $[Re]_{M\,\text{max}}$ is $82{,}770\bar{p}_0$. Hence, for a given pressure $\bar{p}_0$ in the higher-pressure compartment

$$\frac{[Re]_{\bar{M}\,\text{max}}}{[Re]_{M\,\text{max}}} = \frac{223{,}600}{82{,}770} = 2\cdot70 . \qquad \cdots \qquad \cdots \qquad \cdots \qquad \cdots \qquad (4.9)$$

Equation (4.9) holds for any shock tube flow whatsoever.

Specimen values of the shock tube Reynolds numbers per ft $[Re]_{\bar{M}}$ and $[Re]_M$, and their ratio $[Re]_{\bar{M}}/[Re]_M$ are given in Table 6 for $\bar{p}_0 = 214\cdot7$ lb per sq. in. absolute, that is, 200 lb per sq in. gauge, for the range of values of $\bar{M}$ specified by Table 2. The Reynolds numbers per ft corresponding to any other chamber pressure $\bar{p}_0$ may be obtained by direct proportion.

The data of Table 6 are plotted as Fig. 18—*see* shock-tube performance charts.

4.1.2. *Entropy Changes in Shock-Tube Flow.*—Fluid particles are continually crossing the shock wave and an entropy change occurs in this irreversible-flow process. Across the contact surface there is no *flow* and the usual conception of an entropy change has no meaning since an arbitrary value of entropy may be assigned to either of the flow regions bounding the contact surface.

Since the temperature change (and hence the entropy change) across the contact surface will govern its growth into a contact region by thermal conduction, it is convenient to refer to the flow region defined by $\bar{M}$ as a zero entropy datum (that is, $\bar{s} = 0$). With this convention, it is interesting to note that in shock-tube flow a larger entropy change occurs across the contact surface than across the shock wave.

The variation of entropy along a shock tube at some instant after the diaphragm has been ruptured is shown in Fig. 19. Mathematical expressions for the entropy changes are derived below.

17

For a perfect gas with constant specific heats, the equation of state (2.12) is

$$\left(\frac{p}{p_0}\right) = \left(\frac{\rho}{\rho_0}\right)^{\gamma} e^{\frac{s-s_0}{C_v}}$$

or

$$\frac{s-s_0}{C_v} = \log_e \left(\frac{p}{p_0}\right) - \gamma \log_e \left(\frac{\rho}{\rho_0}\right).$$

Now, since $\dfrac{p}{\rho_0} = \dfrac{p}{p_0} \cdot \dfrac{T_0}{T}$ from equation (2.22) and $R = (\gamma - 1)C_v$, the entropy change across the shock is given by

$$\frac{s-s_0}{C_v} = \gamma \log_e \left(\frac{T}{T_0}\right) - (\gamma - 1) \log_e \frac{p}{p_0}. \qquad .. \qquad .. \qquad .. \qquad (4.10)$$

In an exactly similar way, the entropy change across the contact surface (where $p = \bar{p}$) is given by

$$\frac{s-\bar{s}}{C_v} = \gamma \log_e \left(\frac{T}{\bar{T}}\right). \qquad .. \qquad .. \qquad .. \qquad .. \qquad .. \qquad .. \qquad (4.11)$$

But $\bar{T} < T_0 = \bar{T}_0$ for the expanded flow behind the contact surface (*see* Chapter 1, Section 1.2), hence

$$\frac{s-\bar{s}}{C_v} > \frac{s-s_0}{C_v}. \qquad .. \qquad .. \qquad .. \qquad .. \qquad .. \qquad .. \qquad (4.12)$$

Specimen values of the entropy changes across the shock and the contact surface, calculated from equations (4.10) and (4.11) respectively, are given in Table 7 for the range of values of $\dfrac{T}{T_0}, \dfrac{p}{p_0}, V_+$ and $\dfrac{T}{\bar{T}}$ specified by Tables 1 and 5.

4.1.3. *Tabulated Calculations.*—The derivation of the equations governing shock-tube performance is now complete. It remains to show the completed calculations in a concise form and then to adapt these results into a form suitable for practical use. Table 8 illustrates the steps in the calculation procedure and reads from left to right. Equations used are detailed in each column.

4.2. *Performance Charts.*—Figs. 13 to 18 (Charts A to F) contain the calculated data of Table 8 which has been adapted to show in a convenient manner the theoretical performance of any shock tube.

4.2.1. *Specimen Examples of the Uses of the Charts.*—4.2.1.1. *Use as a Short-duration Wind Tunnel.*—Suppose a flow at a Mach number of 2·5 is desired. Vacuum and pressure equipment are available to give an initial pressure ratio P of 1,000, whilst the overall length for the shock tube must not exceed 30 ft.

Chart A determines whether $\bar{M} = 2·5$ is attainable with the given P. [Note $M \neq 2·5$.]

Chart B gives $\tau/\bar{\tau} = 1·55$ corresponding to $\bar{M} = 2·5$.

Charts C and D enable x_0 and $|\bar{x}_0|$ to be chosen, corresponding to τ and $\bar{\tau}$ satisfying the value of $\tau/\bar{\tau}$ from Chart B and to $x_0 + |\bar{x}_0| \gg 30$ ft [e.g., $\bar{\tau} = 0·002$ sec; $\tau = 0·0031$ sec; $\bar{x}_0 = 1·7$ ft; $x_0 = 21$ ft].

Thus, as x_0 and $|\bar{x}_0|$ are known, $X_0 = \dfrac{x_0}{|\bar{x}_0|}$ is known and the positions X_1 and X_2 of the maximum durations of quasi-steady flow τ and $\bar{\tau}$ may be read off from Chart E.

Finally, Chart F yields the Reynolds numbers per foot of the quasi-steady flow regions.

18

4.2.1.2. *To Produce a Shock of a Given Strength p_s or speed V_+.*—In this case, Chart B gives p_s or V_+ corresponding to $\bar{M}$ and the procedure follows that outlined in Section 4.2.1.1.

4.2.1.3. *Modification to Charts when the Flow behind the Contact Surface is the Premier Region of Interest.*—As derived in Chapter 3, Section 3.3, the overall length of the shock tube may be reduced when these conditions appertain. Equation (3.18) gives

$$X_0 = 2X_0' ; \ X_2 = 2X_2' \ \text{and} \ \tau = 2\tau' .$$

Charts D and E allow these modifications to be made if desired.

4.2.1.4. *Maximum Quasi-steady Flow Durations.*—If the values of x_0 and $|\bar{x}_0|$ are greater than the optimum values given by Charts C and D (using the values of $\tau/\bar{\tau}$ and $\bar{M}$ obtained from Chart B) the maximum flow durations τ and $\bar{\tau}$ will be unaffected, but if x_0 and $|\bar{x}_0|$ are less than these optimum values, the available durations will be reduced by wave interactions.

4.2.2. *Variation of Flow Parameters along a Shock Tube.*—Fig. 19 illustrates the conditions at all points of the shock tube at some instant after the diaphragm has been ruptured and before any reflection phenomena have occurred. Typical values for the case $P = 17 \cdot 0$, $\bar{p}_0 = 50$ lb/sq in. (gauge) are shown in the figure.

4.2.3. *Empirical Results.*—From the calculated curves given by Figs. 14 and 17, three empirical equations may be deduced which are very much simpler than the exact equations for $\tau/\bar{\tau}$, X_1 and X_2. These equations are:—

$$\frac{\tau}{\bar{\tau}} = \frac{7}{11}\left[1 + \frac{4}{7}\bar{M}\right] \text{ for } \bar{M} > 1 \quad .. \quad .. \quad .. \quad .. \quad (4.13)$$

and
$$\frac{\tau}{\bar{\tau}} = 1 \text{ for } \bar{M} < 1 \qquad \qquad \qquad [cf. \ (3.19)]$$

and
$$X_2 = 0 \cdot 937 X_0 - 1 \quad .. \quad .. \quad .. \quad .. \quad .. \quad (4.14)$$
$$[cf. \ (3.15)]$$

$$X_1 = 0 \cdot 421 X_0 - 2 . \quad .. \quad .. \quad .. \quad .. \quad .. \quad (4.15)$$
$$[cf. \ (3.14)]$$

4.2.4. *An Explicit Relation between M and $\bar{M}$.*—Since the Mach numbers of the quasi-steady flows are amongst the most important parameters occurring in shock-tube flow, an explicit relation between these two quantities would be useful. If we eliminate V_+ from equations (3.2) and (3.3) we obtain*

$$16\left\{\frac{5}{\bar{M}} + 1\right\}^2 - 12\left\{\frac{5}{M}\right\}^2 + 84 - \left\{\left(\frac{5}{M}\right)^2 - 7 - \left(\frac{5}{\bar{M}} + 1\right)^2\right\}^2 = 0 . \quad .. \quad (4.16)$$

Equation (4.16) will reduce to a form obtained by the writer by an approach from first principles, namely

$$\frac{\bar{M}^2}{(5 + \bar{M})^2} = \frac{M^2}{(25 + M^2 - 2M\sqrt{(9M^2 + 25)})} . \quad .. \quad .. \quad .. \quad (4.17)$$

We may note that, for real $\bar{M}$, from (4.17),

$$M \gg \sqrt{3} \ \text{ i.e., } \ M \gg 1 \cdot 73 .$$

---

* Eqn. (4.16) is due to Professor A. R. Collar.

B 2

CHAPTER 5

Actual Shock-Tube Flow

In the past decade, a considerable amount of development work has been carried out in the United States of America and Canada on shock-tube installations. It is strange, therefore, that the basic experimental properties of shock-tube flow have not been fully explained and that, as yet, no decision has been reached on the validity of the use of a shock tube as a short-duration wind tunnel.

The following Sections contain a brief résumé of available data on experimental shock-tube flow and an attempt to clarify the factors which cause the flow to deviate from that predicted by theory.

5.1. *Experimental Data.*—5.1.1. *The Shock Wave.*—Many investigations[12, 13, 14, 15, 16, 17,] have been made of shock-wave velocities in shock tubes and their general results are illustrated by Fig. 20. It will be noted that for weak shocks (corresponding to $V_+ < 1\cdot7$, that is, $p_s < 3\cdot0$) agreement with theory is very good, but for strong shocks[12] the maximum shock velocity is about 10 per cent lower than the theoretical value. In all cases, a ' formation length ' or ' formation time ' is necessary and, for strong shocks only, a ' distance attenuation ' is also observed. Probable explanations of these phenomena will be discussed in Sections 5.2 and 5.3.

5.1.2. *The Contact Surface.*—A systematic investigation[12] of the contact surface revealed that a ' formation length ' occurred for all shock speeds; and, in addition, a ' distance effect ' was observed for the strong-shock case. This ' distance effect ' was an acceleration of the contact surface, whereas the shock wave suffers a distance attenuation. Fig. 20 compares the motion of the contact surface and the shock wave in shock-tube flow under both weak and strong-shock conditions; it was found experimentally that for the latter case the distance deceleration of the shock and the distance acceleration of the contact surface were of the same order.

Photographs[18] have shown the contact surface to be a mixing region up to 6 in. in thickness.

5.1.3. *The Flow Region Behind the Shock.*—Several investigators have reported uniform flow in this region, especially for weak waves. Many reports[19, 20] mention the occurrence of transverse shock waves, but little attention has been given to these phenomena. Ref. 12, reporting unpublished experiments at Toronto, states that pressure fluctuations of the order of 30 per cent of the primary shock strength may occur in this flow when the primary shock is very strong.

5.1.4. *The Flow Region Behind the Contact Surface.*—Available results[12] indicate that this flow is very similar to a jet flow, that is, it is extremely turbulent and unstable. One investigation[14] has shown fair agreement with theory for the values of M obtained from the bow wave of a wedge placed in the flow. These results indicated that $\bar{M} \gg 4\cdot5$; this has recently been confirmed[12] since very low temperatures $\bar{T}$ do not appear to be reached in this region.

5.1.5. *The Rarefaction Wave.*—A wave-speed camera schlieren photograph enables[12] the speed of sound in the gas at rest in the chamber to be measured from the trace of the head of the rarefaction wave in the photograph. These values are in excellent agreement with shock-tube theory and with acoustic measurements.

However, in all photographs, the tail of the rarefaction wave does not appear, and thus it is not possible to estimate the divergence of the rarefaction wave from the theoretical centred type. Moreover, it is not possible to determine the speed of sound $\bar{a}$, the particle velocity $\bar{u}$ and hence $\bar{M}$ in the region behind the contact surface. Since the density discontinuity is of the same order at both the head and tail of the rarefaction wave and therefore equally likely to appear in a schlieren photograph, some phenomena as yet not understood must occur between the contact surface and the head of the rarefaction wave.

5.1.6. *Viscous Effects.*—Very little has been achieved in the attempt to analyse the non-uniform growth of the boundary layer over an increasing finite part of the length of a shock tube. The probable extent of the boundary layer in a shock tube at some instant after the diaphragm has been ruptured is shown in Fig. 21.

The only approach to this problem is due to Donaldson and Sullivan[21] but this supposes the unreal condition that the boundary layer grows uniformly over an infinite length of the shock tube.

5.2. *The Formation of Shock-Tube Flow and the Transverse Shock Waves.*—5.2.1. *The Bursting of the Diaphragm.*—In practice, it is not possible to remove instantaneously the plane diaphragm which divides the shock tube into two compartments containing air at different pressures. Several flow features are associated with this fact; the most important are the ' formation time ', which the shock and contact surface require to attain their theoretical velocities (*see* Fig. 20), and the creation of a train of transverse shock waves. It may be helpful to state a certain amount of practical data at this point. Cellophane, 0·002 in. thick, has been found to have bursting characteristics which most nearly approach the theoretical requirement of instantaneous removal, that is, it shatters almost completely when punctured. Experiments[4] have shown that the nearer to the natural bursting pressure (18–20 lb per sq in. for 0·002 in. Cellophane) the diaphragm is punctured the better is the shattering and the smaller the total disintegration time (about 100 μsec minimum) and shock-wave ' formation time '. This disintegration time-lag occurs since a small jet of air emerges through the puncture and then the diaphragm shatters. [*See* pictures, pp. 60–61, Ref. 14.]

Cellophane diaphragms bow considerably when subjected to pressure and this further complicates the process of flow formation. However, it is known[12] that this initial bow, the position of the diaphragm breaker and the remnants of the shattered diaphragm have no effect on the measured shock speed. [Note in passing that these factors probably contribute to the turbulence behind the contact surface.]

In order to utilise large absolute pressures in the chamber, multiple diaphragms may be used; however care must be taken that they are all punctured simultaneously and stressed to at least one-half to two-thirds of their natural bursting pressure. This leads to the use of a special diaphragm assembly having a stepped pressure between each sheet of Cellophane.

5.2.2. *The Formation of a Plane Shock-Wave.*—When the bowed diaphragm is ruptured, a number of curved compression waves are propagated into the channel (*see* Fig. 22A). These compression waves very quickly coalesce to form a curved shock-wave (B). Since the shock is ' centred ' on point O, its profile will become less curved (C) as it progresses down the channel. Regular reflection of this curved shock will take place at the walls of the tube until the angle of incidence of the shock is such that regular reflection of the shock is impossible and the shock then undergoes Mach reflection (D). (*See* Ref. 10, p. 331.) The triple points T of the Mach reflection move toward the centre of the tube, thus producing a plane shock-wave. Subsequently, the triple points continue to move back and forth across the tube (E) until the secondary branches of the Mach configuration are very weak and disappear. Finally an optically flat primary shock is propagated down the channel (F). Photographs obtained by Lobb[14] support the above explanation*.

The elapsed time and the distance travelled by the primary shock before it becomes plane have been reported by many investigators. No consistent feature is noticed in their results, but it is probably true to assert that imperfect diaphragm rupture only affects the time taken for the shock to become plane and does not affect the optimum shock speed or the subsequent shock attenuation (Fig. 20).

Hence the ' formation distance ' depends on the shock speed and the ' quality ' of the diaphragm rupture. This would explain the different values of ' formation distance ' reported in different investigations.

---

* Multiple spark shadowgraphs which clearly show the above process have been obtained at Fort Halstead.

5.2.3. *The Transverse Shock Waves.*—The basic mechanism whereby a plane shock is formed in a shock tube has been described in the previous Section 5.2.2. However, experimental data have shown that under certain conditions the oblique branches of the Mach reflection do not die out in time, thus forming a system of transverse shock waves following the primary shock down the channel.

Fig. 23 is a simple geometrical construction which shows the pattern formed by successive reflections of two cylindrical waves in the side walls of a shock tube. In Fig. 23 we postulate that the cylindrical waves are formed by diffraction of the primary shock over small bumps on the tube wall at O_1, O_2. Points A and B correspond to the triple points T_1, T_2 of Fig. 22, and the secondary branches of the Mach configuration undergo regular reflection at points A_1A_2, B_1B_2, etc. Fig. 23 shows remarkable agreement with the transverse wave systems illustrated in Fig. 24, photographs obtained by the present writer during some preliminary experimental work previously reported[22].

An attempt* has been made to correlate experimental results with theory; in particular, an expression has been derived for the angle θ between the oblique transverse wave and the normal shock.

Consider the diffraction of a plane shock by a small bump and let the shock hit the bump at time $t = 0$. Then the configuration at any subsequent time t is as shown in Fig. 25. The diffracted circular wave, centre C, is assumed to be a sound wave.

Then θ is the angle required, since in this linearised problem the oblique wave is the almost straight part of the acoustic circle near the point A in Fig. 25 (or of some image of the original circle formed by reflections in the walls of the shock tube—Fig. 23).

Hence, directly from Fig. 25,

$$\cos \theta = \frac{U - u}{a}.$$

But, by combining equations (2.24) and (2.25) and eliminating p/p_0 we have, with $\gamma = 1 \cdot 4$, $U/a_0 = V_+$,

$$\left(\frac{U - u}{a}\right)^2 = \frac{V_+^2 + 5}{7V_+^2 - 1}.$$

Hence

$$\theta = \cos^{-1}\sqrt{\left(\frac{V_+^2 + 5}{7V_+^2 - 1}\right)}. \qquad \text{..} \qquad \text{..} \qquad \text{..} \qquad \text{..} \qquad (5.1)$$

Evaluation of Data.—Available data on the transverse waves are extremely limited. A photograph by Kantrowitz (Ref. 19, p. 876, Fig. 3) shows these phenomena but there is no comment in the text. Ref. 12 reproduced results by Uhlenbeck on an associated problem. These results are summarised in the following table and compared with the theoretical method.

		Uhlenbeck Ref. 12	Kantrowitz Ref. 19	Henshall Ref. 22	Henshall Ref. 22
Shock speed	V_+	$1 \cdot 19$	$1 \cdot 23$	$1 \cdot 34$	$1 \cdot 42$
Mach number behind shock ..	M	$0 \cdot 28$	$0 \cdot 32$	$0 \cdot 45$	$0 \cdot 53$
$K = \sqrt{\{(V_+^2 + 5)/(7V_+^2 - 1)\}}$		$0 \cdot 85$	$0 \cdot 83$	$0 \cdot 76$	$0 \cdot 73$
Theory	θ_T	$32°$	$34°$	$40°$	$43°$
Experimental	θ_E	$28°$	$33°$	$33°$	$36°$

* Suggested by Dr. D. Blackburn.

5.3. *Critical Analysis of Experimental Flow Results.*—5.3.1. *The Basic Assumption.*—In Chapter 3 we analysed ideal shock-tube flow by combining the equations of motion of a centred rarefaction wave and of a normal shock, so as to satisfy the conditions at the contact surface (at which the pressure and velocity were assumed continuous, that is $u = \bar{u}$ and $p = \bar{p}$). That is to say, we matched two separate flow processes by using the concept of a non-conducting contact surface. Whether this procedure is valid is open to slight doubt, since at the contact surface two separate stagnation quantities apply, namely, $\dfrac{2}{\gamma - 1} a_0$, a momentum constant per unit mass for the unsteady isentropic rarefaction wave process—*see* equations (2.15) and (2.16)—and $C_p T_0$, an energy constant per unit mass for the steady irreversible shock process which we have transformed by superposition of velocities (*see* Fig. 3) into an unsteady process—*see* equations (2.21), (2.22) and note $\gamma R/(\gamma - 1) = C_p$.

It is probable that this inconsistency in stagnation quantities may be related to the well-known discrepancy between the maximum speeds attainable by a stream of air in one-dimensional steady and unsteady flows. These 'limit' speeds are $\sqrt{\left(\dfrac{2}{\gamma - 1}\right)} \cdot a_0$ and $\dfrac{2}{\gamma - 1} a_0$ respectively, where a_0 is the speed of sound in the reservoir.

No satisfactory explanation of these facts has yet been formulated.

5.3.2. *The Shock Tube Anomaly.*—We have noted previously that in real shock-tube flow the shock is retarded as it progresses down the channel whereas the contact surface is accelerated by approximately the same amount.

Now it is well known (*see* Ref. 10, pp. 166–7) that the acceleration of a piston moving in a tube will cause a shock wave and that a deceleration will result in the formation of a rarefaction wave. In the shock tube, the contact surface may be regarded as a piston, and consequently we would expect an accelerating contact surface to imply an accelerating shock (that is, a shock of increasing strength). The opposite is the case, however and this apparent paradox has been called the shock tube anomaly.

In an attempt to explain the acceleration of the contact surface, Hall[23] has solved the linearized problem of heat conduction across the contact surface by treating the ideal temperature step-discontinuity ($\bar{T} < T$) as the initial value of his solution when $t = 0$. Although this does show that the contact surface will accelerate and diffuse in the course of time, the predicted velocity increase is very small (less than $0 \cdot 01$ per cent); this can be attributed to the fact that experimental flow involves turbulent mixing of the gas forming the contact surface whereas the theory only holds for 'laminar' heat transfer.

5.3.3. *Shock-Tube Vibration.*—We have so far considered the shock tube to be rigid, but it is possible that some of the energy of the shock is dissipated by conversion to vibrational energy of the tube. In an interesting paper by Niordson (1952)[24] a linearized solution is given for this problem on the assumption that the tube is thin walled.

This solution gives the following equation for the velocity behind the normal shock

$$u = \frac{2}{(\gamma + 1)} \cdot \frac{U^2 - a_0^2}{U\left\{1 - \frac{1}{2}\left(\dfrac{U}{U_a}\right)^2\left[\dfrac{2U^4 - U_0^4}{U^4 - U_0^4}\right]\right\}} \quad \cdot\cdot \quad \cdot\cdot \quad \cdot\cdot \quad (5.2)$$

where U_a and U_0 are constants depending on the size and material of the tube and the gas within the tube.

Compare (5.3) with (2.26) when $u_0 = 0$, in the form

$$u = \frac{2}{(\gamma + 1)} \cdot \frac{U^2 - a_0{}^2}{U} .$$

The present writer has computed the value of the { } bracket in equation (5.3) for several shock tubes under various test conditions. From these calculations it is clear that this mechanism is not the cause of shock retardation, since the decrement is always less than $\frac{1}{2}$ per cent, negligible compared with the experimental decrease of up to 10 per cent (*see* Ref. 12, for example). It may be noted that the above theory refers to thin-walled tubes and weak shocks, whereas the calculations did not necessarily satisfy these conditions. Nevertheless, linear theory usually yields answers in excess of the true result, and this gives added emphasis to the above conclusion.

5.3.4. *The Consequences of the Transverse Waves.*—Since the transverse waves are segments of cylindrical waves, they will have rarefaction waves attached and they will not have the ' step ' profile of the primary normal shock wave. Shock decay will therefore take place and this, in addition to the viscous flow dissipation, will affect the uniformity of the flow behind the shock.

It will be shown later by a boundary-layer analysis that the flow behind the shock is not truly quasi-steady, and it may be stated now that if the transverse waves occur, neither is this flow uniform.

Fig. 24 shows these transverse shock waves clearly; the attached rarefaction waves are also prominent. Ref. 12 contains many photographs of these phenomena; in certain cases (e.g., p. 164) they appear to be stronger than the primary shock wave, a fact which had been noted previously[22] by the present writer. The occurrence of the transverse waves is most noticeable when the absolute channel pressure is near atmospheric (this may be due to optical considerations or to Reynolds number effects).

Tube size will affect the number of reflections of the transverse waves (*see* Fig. 23) and correspondingly we would expect greatest shock attenuation to be observed in the smallest shock tubes—this is experimentally confirmed.

We have postulated that the transverse waves originate at the diaphragm section, and in that case we may eliminate them from the flow by suitably shaping that portion of the channel adjacent to the diaphragm section. It is only necessary to ensure that the initial curved shock is everywhere normal to the walls of the tube. A trial and error procedure, using shadow or schlieren photography, would be required. The probable shape of the diaphragm section of such a shock tube is illustrated in Fig. 27.

5.3.5. *Measurements of Shock Speed.*—In the assessment of the large amount of experimental data relating to shock velocities it is noticeable that certain factors have considerable influence on the results. In the present section an attempt will be made to correlate existing data in a concise manner.

A simple dimensional analysis shows that the shock attenuation due to viscous effects will depend on :—

(i) the length of tube traversed by the shock wave, (X_s),

(ii) the hydraulic radius of the tube, $H = \dfrac{\text{area of tube}}{\text{perimeter}}$,

(iii) the Mach number of the flow behind the shock, M, which we may conveniently replace by the shock strength p_s, or the shock speed V_+,

(iv) the Reynolds number of the flow, Re, and

(v) the roughness of the surface of the tube.

24

Experiments show that the shock attenuation INCREASES with

(1) Increase of $\dfrac{X_s}{H}$ (Ref. 13)

(2) Increase of p_s or V_+ (Refs. 13, 16, 12)

(3) Increase of Re (present author)

(4) Increase of tube roughness (Ref. 16)

(5) Increase of $\dfrac{vt}{A}$ (Ref. 12).

The parameter vt/A where v is the kinematic viscosity, A the cross-sectional area of the tube and t the time since the motion began (that is $t = X_s/V_+$), was introduced by Donaldson and Sullivan[21] in the first analysis of viscous effects in shock tubes (*see* Section 5.1.6).

A theory, based on boundary-layer analysis, which is developed in Part C of this report, shows that the shock attenuation varies in accordance with (1) to (5) [excluding (4), which only admits empirical results] above.

Note that attenuation occurs for a very smooth plate[16], and also that a shock hitting the open end of a tube will travel more quickly outside than inside[12, 13]. This confirms that imperfect diaphragms only affect the time taken for shock formation and have no effect on the distance attenuation.

Emrich and Curtiss[13] have developed an attenuation factor which they claim to be in error by not more than a factor of 2. This is :—

$$\frac{H}{z} \cdot \frac{dz}{dx} = 3 \cdot 5 \times 10^{-4} \quad \dots \qquad \dots \qquad \dots \qquad \dots \qquad \dots \qquad \dots \qquad \dots \qquad (5.3)$$

where $z = (p_s - 1)$. They also found that $\dfrac{dz}{dx}$ was independent of the distance traversed by the wave along the tube but was a function of the shock strength.

To sum up, the shock attenuation will be important when :—

(*a*) long tubes of small cross-section are used—(1) above,

(*b*) strong shocks are produced—(2), (5),

(*c*) the absolute pressures used are considerable—(3), and

(*d*) when the interior finish of the shock tube is irregular—(4).

5.3.6. *Recent Experimental Uses of the Shock Tube.*—Since the major part of this report was completed, further uses of the shock tube have been reported. Duff[16] has investigated the interaction between shock waves and rough surfaces, Parks[25] has initiated an investigation of flow in a shock tube of divergent cross-section, whilst Elder and de Haas[26] have studied the formation of a vortex ring at the open end of a cylindrical shock tube. Bernstein[27] has suggested a double-diaphragm shock tube for the attainment of high Mach number flows, and Kantrowitz[28] has continued his work with divergent duct shock tubes.

The Maximum Duration of Quasi-steady Flow behind the Shock

Consider a shock tube with the diaphragm originally at $X = 0$ and the lower-pressure compartment of length X_0. The maximum duration τ of quasi-steady flow occurs at the position X_2 where the reflected shock meets the contact surface (*see* Fig. 9).

Using non-dimensional notation as before, we write

$$\frac{U}{a_0} = V_+ \text{ for the incident shock, velocity } U$$

$$\left|\frac{U_R}{a_0}\right| = V_- \text{ for the reflected shock, velocity } U_R, \text{ and}$$

$$\frac{u}{a_0} = v_+ \text{ for the contact surface, velocity } u.$$

Also,
$$t \left(\equiv \frac{\bar{a}_0}{|\bar{x}_0|} \cdot t \right) \text{ is the time parameter and}$$

$$X \left(\equiv \frac{x}{|\bar{x}_0|} \right) \text{ is the distance parameter.}$$

Now, the shock takes a time t_s to travel a distance X_2 and the contact surface takes a time $t_s + \tau$ to travel the same distance X_2.

Thus
$$\frac{X_2}{V_+} = t_s \text{ and } \frac{X_2}{v_+} = t_s + \tau = \frac{X_2}{V_+} + \tau.$$

Then
$$\frac{\tau}{X_2} = \frac{1}{v_+} - \frac{1}{V_+}. \qquad \qquad \qquad \qquad \qquad \qquad \qquad \text{(A1.1)}$$

But, also in time τ, both incident and reflected shocks traverse a distance $(X_0 - X_2)$.

Thus
$$(X_0 - X_2) \left\{ \frac{1}{V_+} + \frac{1}{V_-} \right\} = \tau. \qquad \qquad \qquad \qquad \qquad \text{(A1.2)}$$

Hence, eliminating τ from equations (A1.1) and (A1.2) we have

$$\frac{\tau}{X_2} = \left\{ \frac{1}{v_+} - \frac{1}{V_+} \right\} = \left\{ \frac{X_0 - X_2}{X_2} \right\}\left\{ \frac{1}{V_+} + \frac{1}{V_-} \right\}.$$

Or, rearranging,
$$\frac{X_0}{X_2} = 1 + \left\{ \frac{\dfrac{1}{v_+} - \dfrac{1}{V_+}}{\dfrac{1}{V_+} + \dfrac{1}{V_-}} \right\} = \frac{\dfrac{V_+}{v_+} + \dfrac{V_+}{V_-}}{1 + \dfrac{V_+}{V_-}}. \qquad \qquad \text{(A1.3)}$$

Finally, substitute for X_2 in (A1.3) in terms of τ, using (A1.1).

Then
$$\frac{X_0}{\tau} = \frac{V_- \left(\dfrac{V_+}{v_+} + \dfrac{V_+}{V_-} \right)}{\left\{ \dfrac{V_+}{v_+} - 1 \right\}\left\{ \dfrac{V_-}{V_+} + 1 \right\}}.$$

Put in partial factions, then
$$\frac{X_0}{\tau} = \frac{\left(\dfrac{V_-}{V_+} \right) V_+}{\left(\dfrac{V_-}{V_+} + 1 \right)} + \frac{V_+}{\left(\dfrac{V_+}{v_+} - 1 \right)}. \qquad \qquad \qquad \text{(A1.4)}$$

Equations (A1.3) and (A1.4) show the influence of the lower-pressure compartment length X_0 on the position and duration of the quasi-steady flow behind the shock.

APPENDIX A2

The Path of the Head of the Reflected Rarefaction Wave

For the reflected head of the rarefaction wave, characteristic C_+^H (*see* Fig. 7), equation (2.15) gives

$$\frac{dX}{dt} = \bar{u} + \bar{a}. \qquad \qquad \qquad \qquad \qquad \qquad \qquad (A2.1)$$

This characteristic passes through the point $(1, -1)$ of the (t, X)-plane and traverses the incident rarefaction wave region (a fan of C_- characteristics radiating from the diaphragm at $X = 0$) where the flow parameters vary according to equations (2.16), namely $(\gamma = \bar{\gamma})$,

$$\bar{u} + \frac{2\bar{a}}{\gamma - 1} = \frac{2}{\gamma - 1} \quad \text{and} \quad \frac{X}{t} = \bar{u} - \bar{a}. \qquad \qquad \qquad \qquad (A2.2)$$

Rearranging (A2.2) for $\bar{u}$ and $\bar{a}$ explicitly we obtain

$$\bar{u} = \frac{2}{\gamma + 1}\left\{\frac{X}{t} + 1\right\}; \; \bar{a} = \frac{\gamma - 1}{\gamma + 1}\left\{\frac{2}{\gamma - 1} - \frac{X}{t}\right\}. \qquad \qquad (A2.3)$$

Inserting (A2.3) in (A2.1), we have,

$$\frac{dX}{dt} = \left(\frac{3 - \gamma}{\gamma + 1}\right)\frac{X}{t} + \frac{4}{\gamma + 1}. \qquad \qquad \qquad \qquad (A2.4)$$

Equation (A2.4) may be solved by putting $w = \frac{X}{t}$, that is,

$$\frac{dX}{dt} = w + t\frac{dw}{dt}.$$

Then

$$t\frac{dw}{dt} = w\cdot\left\{\frac{3 - \gamma}{\gamma + 1} - 1\right\} + \frac{4}{\gamma + 1}.$$

Separate the variables and integrate; hence

$$\log_e t = \frac{\gamma + 1}{2(1 - \gamma)}\log_e\left\{2\left(\frac{1 - \gamma}{\gamma + 1}\right)w + \frac{4}{\gamma + 1}\right\} + \text{constant } C.$$

Since $w = -1$ at the point $A(1, -1)$ of the (t, X)-plane (*see* Fig. 7), the constant $C = -\log_e 2$.

Reverting to the original variables, we have

$$X = \frac{2}{\gamma - 1}t - \frac{\gamma + 1}{\gamma - 1}t^{\frac{3 - \gamma}{\gamma + 1}}. \qquad \qquad \qquad \qquad (A2.5)$$

But, from (2.18)

$$\frac{X}{t} = \frac{\bar{M} - 1}{1 + \frac{\gamma - 1}{2}\bar{M}}. \qquad \qquad \qquad \qquad \qquad (A2.6)$$

By combining (A2.5) and (A2.6) we obtain

$$t = \left(1 + \frac{\gamma - 1}{2}\bar{M}\right)^{\frac{\gamma + 1}{2(\gamma - 1)}}. \qquad \qquad \qquad \qquad (A2.7)$$

Finally, combination of (A2.5) and (A2.7) gives

$$X = (\bar{M} - 1)\left\{1 + \frac{\gamma - 1}{2}\bar{M}\right\}^{\frac{3 - \gamma}{2(\gamma - 1)}}. \qquad \qquad \qquad (A2.8)$$

The above equations hold for all values of $\bar{M}$, and may be simplified by putting $\gamma = \bar{\gamma} = 1\cdot4$ for the conventional shock-tube case. (*See* equations (3.10) to (3.12).)

The Maximum Duration of Quasi-steady Flow behind the Contact Surface

Case 1.　$\bar{M} < 1$.　(Fig. 10.)

For convenience write $\dfrac{\gamma + 1}{2(\gamma - 1)} = \alpha\,;\ \left(1 + \dfrac{\gamma - 1}{2}\bar{M}\right) = \beta$.

We require (A2.5), namely

$$X = \frac{2}{\gamma - 1}\,t - \frac{\gamma + 1}{\gamma - 1}\,t^{\frac{3-\gamma}{\gamma+1}} \qquad \qquad \qquad \qquad \qquad \qquad \text{(A3.1)}$$

Also, equations (A2.7) and (A2.8) become

$$t_1 = \beta^\alpha \qquad \qquad \qquad \qquad \qquad \qquad \qquad \qquad \text{(A3.2)}$$

and

$$X_1 = (\bar{M} - 1)\beta^{\alpha-1} \text{ respectively} \qquad \qquad \qquad \qquad \text{(A3.3)}$$

where $\bar{M}$ is the value corresponding to point B (t_1, X_1). [Note that for part AB of the path ABC of the reflected head of the rarefaction wave, $\bar{M}$ is a variable, its value being zero at A $(1, -1)$ and $\bar{M}$ at B (t_1, X_1), according to equations (3.11) and (3.12).]

From Fig. 10, we see that

$$\bar{\tau} = t_1 + (\bar{\tau} - t_1) . \qquad \qquad \qquad \qquad \qquad \qquad \text{(A3.4)}$$

Also, the slope of BC, positive from figure

$$= \left(\frac{dX}{dt}\right)_{BC} = \frac{-X_1}{\bar{\tau} - t_1} \qquad \qquad \qquad \qquad \qquad \text{(A3.5)}$$

noting that X_1 is a negative quantity.

But the slope of BC must be equal to the slope of AB at B for continuity. Now, from (A3.1), the slope of AB at B (t_1, X_1) is

$$\left(\frac{dX}{dt}\right)_B = \frac{2}{\gamma - 1} - \frac{3 - \gamma}{\gamma - 1}\,t_1^{-(1/\alpha)}$$

or, using (A3.2),　$\left(\dfrac{dX}{dt}\right)_B = \dfrac{2}{\gamma - 1} - \dfrac{3 - \gamma}{\gamma - 1}\,\beta^{-1}$. $\qquad \qquad \qquad \qquad$ (A3.6)

Equating (A3.5) and (A3.6), and using (A3.3), we obtain

$$-\frac{(\bar{M} - 1)\beta^{\alpha-1}}{\bar{\tau} - t_1} = \frac{2}{\gamma - 1} - \frac{3 - \gamma}{\gamma - 1}\,\beta^{-1} . \qquad \qquad \qquad \text{(A3.7)}$$

Substitute in (A3.4) for t_1 and $(\bar{\tau} - t_1)$ using (A3.2) and (A3.7), and simplify.

Then　$\qquad \qquad \qquad \bar{\tau} = \dfrac{2\beta^\alpha}{1 + \bar{M}}\,(\bar{M} < 1)$. $\qquad \qquad \qquad \qquad \qquad$ (A3.8)

We must also determine the co-ordinates of the point C (t_2, X_2) where the reflected head of the rarefaction wave overtakes the contact surface. From the equation of the contact surface we have

$$X_2 = v_+ t_2 = \bar{a}\bar{M}t_2 . \qquad \qquad \qquad \qquad \qquad \qquad \text{(A3.9)}$$

Also, for BC, characteristic C_+^H (*see* Fig. 10 and equation (A2.1))

$$\frac{dX}{dt} = \frac{X_2 - X_1}{t_2 - t_1} = \bar{u} + \bar{a} = \bar{a}(\bar{M} + 1) , \qquad .. \qquad .. \qquad .. \quad (A3.10)$$

and for OB, characteristic C_-^T, equation (A2.2),

$$\frac{X_1}{t_1} = \bar{u} - \bar{a} = \bar{a}(\bar{M} - 1) . \qquad .. \qquad .. \qquad .. \qquad .. \qquad .. \quad (A3.11)$$

On substituting for X_2 and X_1 in equation (A3.10), using (A3.9) and (A3.11), and simplifying, we get

$$t_2 = 2t_1 . \quad .. \qquad .. \qquad .. \qquad .. \qquad .. \qquad .. \qquad .. \qquad .. \quad (A3.12)$$

Now substitute (A3.2), (A3.3) and (A3.12) in (A3.10), then

$$X_2 = \bar{a}(\bar{M} + 1)\beta^\alpha + (\bar{M} - 1)\beta^{\alpha-1} .$$

But from (2.17) $\qquad \bar{a} = \beta^{-1} = \left(1 + \frac{\gamma - 1}{2} \bar{M}\right)^{-1}$, hence

$$X_2 = 2\bar{M}\beta^{\alpha-1} . \qquad .. \qquad .. \qquad .. \qquad .. \qquad .. \qquad .. \qquad .. \quad (A3.13)$$

Case 2. $\bar{M} > 1$.   (Fig. 11.)

Equations (A3.2), (A3.3), (A3.12) and (A3.13) again give the (t, X) co-ordinates of points B (t_1, X_1) and C (t_2, X_2). The maximum flow duration $\bar{\tau}$ now occurs at section X_1 where $\bar{\tau}$ is given by

$$t_1 = t_c + \bar{\tau} \ (\textit{see} \text{ Fig. 11}) . \qquad .. \qquad .. \qquad .. \qquad .. \qquad .. \quad (A3.14)$$

Also, from the equation to the contact surface (A3.9), and (A3.3), we have

$$X_1 = \bar{a}\bar{M}t_c = \frac{1}{\beta} \bar{M}t_c = (\bar{M} - 1)\beta^{\alpha-1}$$

or, rearranging $\qquad t_c = \left(\frac{\bar{M} - 1}{\bar{M}}\right)\beta^\alpha . \qquad .. \qquad .. \qquad .. \qquad .. \qquad .. \qquad .. \quad (A3.15)$

Substituting in (A3.14) for t_c and t_1 from (A3.15) and (A3.2), we have

$$\bar{\tau} = \frac{\beta^\alpha}{\bar{M}} \qquad (\bar{M} > 1) .$$

In the conventional shock tube case, $\gamma = 1\cdot4$, $\alpha = 3$ and $\beta = 1 + \bar{M}/5$, and the above equations reduce to equations (3.13) to (3.17) in the main text.

APPENDIX A4

An Explicit Relation for $\tau/\bar{\tau}$

Case 1. $\bar{M} < 1$.

The equations connecting the quantities τ and $\bar{\tau}$ are:

(A1.1) $\qquad\qquad\qquad \tau = \left(\frac{1}{v_+} - \frac{1}{V_+}\right) X_2$

(A3.13) $\qquad\qquad\qquad X_2 = 2\bar{M}\beta^{\alpha-1}$

(A3.8) $\qquad\qquad\qquad \bar{\tau} = 2\beta^\alpha/(1 + \bar{M})$

Combining these equations, we have

$$\frac{\tau}{\bar{\tau}} = \left(\frac{1}{v_+} - \frac{1}{V_+}\right)\left(\frac{5\bar{M}}{5+\bar{M}}\right)(1+\bar{M}) . \quad .. \qquad .. \qquad .. \qquad .. \qquad (A4.1)$$

But

$$\frac{1}{v_+} = \frac{1}{\bar{a}\bar{M}} = \frac{\beta}{\bar{M}} \quad (\textit{see} \text{ equation (2.17)}) . \quad .. \qquad .. \qquad .. \qquad .. \qquad (A4.2)$$

Hence, substituting for $\dfrac{1}{v_+}$, we obtain ($\bar{M} < 1$),

$$\frac{\tau}{\bar{\tau}} = (1+\bar{M})\left[1 - \left(\frac{5\bar{M}}{5+\bar{M}}\right)\frac{1}{V_+}\right] . \quad .. \qquad .. \qquad .. \qquad .. \qquad (A4.3)$$

Case 2. $\bar{M} > 1$.

In an exactly similar way, but using (A3.16) instead of (A3.8) to define $\bar{\tau}$, we obtain

$$\frac{\tau}{\bar{\tau}} = 2\bar{M}\left[1 - \frac{5\bar{M}}{5+\bar{M}}\frac{1}{V_+}\right] . \quad .. \qquad .. \qquad .. \qquad .. \qquad .. \qquad (A4.4)$$

APPENDIX A5

Quasi-steady Flow Reynolds Numbers in a Shock Tube

The relevant equations are:

$$(4.3) \qquad \frac{\bar{\rho}}{\rho} = \frac{T}{\bar{T}} = \left(\frac{\bar{M}}{M}\right)^2 \quad .. \qquad .. \qquad .. \qquad .. \qquad .. \qquad .. \qquad .. \qquad (A5.1)$$

$$(4.4) \qquad \frac{[Re]_{\bar{M}}}{[Re]_M} = \frac{\bar{\rho}}{\rho}\cdot\frac{\bar{u}}{u}\cdot\frac{\mu}{\bar{\mu}} \quad .. \qquad .. \qquad .. \qquad .. \qquad .. \qquad .. \qquad .. \qquad (A5.2)$$

$$(4.5) \qquad \frac{\mu}{\bar{\mu}} = \left(\frac{T}{\bar{T}}\right)^{3/4} \quad .. \qquad .. \qquad .. \qquad .. \qquad .. \qquad .. \qquad .. \qquad (A5.3)$$

Combination of (A5.1) to (A5.3) gives, directly,

$$(4.6) \qquad \frac{[Re]_{\bar{M}}}{[Re]_M} = \left(\frac{T}{\bar{T}}\right)^{7/4} = \left(\frac{\bar{M}}{M}\right)^{7/2} . \quad .. \qquad .. \qquad .. \qquad .. \qquad .. \qquad .. \qquad (A5.4)$$

Now, by definition $[Re]_{\bar{M}} = \bar{\rho}\bar{u}/\bar{\mu}$.

Introducing the reference state, suffix $_0$, superscript $^-$, using (A5.3) and noting that $\dfrac{\gamma\bar{p}_0}{\bar{\rho}_0} = \bar{a}_0{}^2$ and $\bar{M} = \dfrac{\bar{u}}{\bar{a}}$, we have

$$[Re]_{\bar{M}} = \frac{\bar{\rho}}{\bar{\rho}_0}\cdot\frac{\bar{a}}{\bar{a}_0}\cdot\bar{M}\cdot\frac{\gamma\bar{p}_0}{\bar{\mu}_0\bar{a}_0}\cdot\left(\frac{\bar{T}_0}{\bar{T}}\right)^{3/4} .$$

But, from (2.17),

$$\frac{\bar{\rho}}{\bar{\rho}_0} = \left(\frac{\bar{T}}{\bar{T}_0}\right)^{5/2} \text{ and } \frac{\bar{a}}{\bar{a}_0} = \left(\frac{\bar{T}}{\bar{T}_0}\right)^{1/2} = \left(1 + \frac{\gamma-1}{2}\bar{M}\right)^{-1} .$$

Finally, it follows that

$$[Re]_{\bar{M}} = \frac{\gamma\bar{p}_0}{\bar{\mu}_0\bar{a}_0}\bar{M}\left(1 + \frac{\gamma-1}{2}\bar{M}\right)^{-4\cdot5} . \qquad .. \qquad .. \qquad .. \qquad .. \qquad (A5.5)$$

Hence equation (4.7) follows when $\gamma = 1\cdot4$, $\bar{a}_0 = 1{,}118$ ft/sec, $\bar{\mu}_0 = 3\cdot719 \times 10^{-7}$ slugs/ft sec at 15°C and $\bar{p}_0$ is measured in lb per sq in. absolute.

Differentiation of (A5.5) and equating to zero shows that the maximum $[Re]_{\bar{M}}$ occurs at $\bar{M} = 1\cdot429$.

PART B—THE CONSTRUCTION AND CALIBRATION OF A SHOCK-TUBE INSTALLATION

CHAPTER 6

The Shock-Tube Installation : General Design

Almost every report of experiments with shock tubes has contained a section dealing with the design criteria relevant to the application of the shock tube to the particular problem therein reported. It is pointless to reiterate available information[5, 6, 7, 8, 12, 15, 19] and thus the following chapter is devoted solely to design problems encountered during the present work.

6.1. *Overall Design Considerations.*—Shock-tube installations may be rudimentary and inexpensive or complex and costly. Assuming that results of comparable accuracy are required from all installations, the recording instrumentation will vary little in either type or cost ; this implies that the overall cost of an installation depends only on the type of construction employed for the shock tube proper. Only limited funds were available in the present case, and low cost was an essential feature of the design.

If instantaneous photography of either unsteady or quasi-steady phenomena is contemplated (as in this case), then the cross-section of the shock tube must be rectangular to satisfy the requirements of the optical system. It is now possible to consider the principal methods whereby a shock tube of rectangular cross-section may be constructed. Five possible configurations are illustrated in Fig. 28 and a brief summary of the salient features of each type is given below.

(a) Fillet-welded steel plate. Easily made, moderate cost, but distortion is considerable in large shock tubes.

(b) A steel plate fillet-welded to a steel channel. Preferable to (a), but distortion can again be considerable.

(c) Extruded aluminium box-section. Convenient in small standard sizes, but the prohibitive cost of die manufacture makes special large ' shock-tube ' sections impracticable.

(d) Two ground steel plates, bolted to two machined channels and positively located by dowels. This construction gives extremely accurate internal dimensions.

(e) Wood planks, glued, screwed and jointed. A cheap, easily manufactured construction, and although wood is never a permanent material, well-seasoned varieties minimize distortion troubles.

As previously stated, low cost was one of the main criteria of this design, hence construction method (e) was chosen*. Moreover, most shock tubes[5, 6, 12] have been very accurately constructed (in particular, the Toronto shock tube[12], utilizing method (d) above, is accurate to one thousandth of an inch in cross-sectional dimensions throughout its length of $16\frac{1}{2}$ ft), and the present writer wanted to compare results from ' luxury ' and ' utility ' shock tubes.

The height of the cross-section is chosen so that diffracted waves from objects in the working-section will not cause undue interference when reflected from the roof and floor of the tube; the width is related to the sensitivity of the flow visualization methods. Consideration of these facts led to the choice of a cross-section 6 in. high and $2\frac{1}{2}$ in. wide. To avoid undue vibration during a test, it is desirable for the tube to have a substantial wall thickness; the $1\frac{3}{8}$-in. thick seasoned mahogany planks which were available† for this installation ensured that shock induced vibrations were kept to a tolerable level. We have previously noted (Chapter 4) that for maximum flow durations the length of the shock tube should be a maximum ; that is, laboratory size will determine the shock tube length. Fig. 29 is a schematic diagram of the Bristol University Aeronautical

---

* The Bristol shock tube is believed to be the first employing wooden construction.

† The Bristol shock tube was manufactured by John Perkins and Sons, Ltd., Easton, Bristol, 5.

31

Extension Laboratory, and it will be noted that only a limited space was available for the installation. The chosen overall length of 36 ft was the maximum possible length compatible with access to door D_2.

Several types of vacuum pump were available for evacuation of the channel and a compressor supplied high-pressure air to the chamber via two storage bottles. Fig. 30 illustrates the pipework of the installation and details all valves, gauges and air supplies. The maximum design diaphragm pressure ratio P for this shock tube is approximately 11,000 : 1, to be obtained using a chamber pressure of 200 lb/sq in. (gauge) and a channel pressure of one millimetre of mercury. The achievement of high pressure-ratios is limited by the loss of sensitivity of the optical system at very low absolute pressures (channel criteria) and the static strength of the diaphragm (chamber criteria).

All vacuum and pressure gauges, their associated shut-off valves, the diaphragm-striker release toggle and a mercury barometer were mounted on a control panel adjacent to the diaphragm section of the shock tube (*see* Figs. 29, 30 and 31). We have noted that the maximum possible length of this shock tube was 36 ft. It remained to decide the respective lengths of the chamber and the individual interchangeable channel sections. Interest in testing in the transonic region[6] suggested as a typical case for calculation, $M = 1 \cdot 0$; whence $P = 42$, $\bar{M} = 1 \cdot 82$, $X_0 = 8$, $x_0 = 32$ ft and $|\bar{x}_0| = 4$ ft (*see* Table 8). The ratio X_0, (channel length)/(chamber length), is different for each quasi-steady flow Mach number, hence both the chamber and the channel should be of variable length.

The total channel length of 36 ft was made up of individual sections of lengths 12, 6, 5, 4, 2, 2 and 1 ft. All sections (except the 12-ft section which incorporated the diaphragm joint and ancillary equipment) were interchangeable so that the channel length was adjustable from 12 ft to 32 ft in 1-ft steps. Further, the working-section, 2 ft in length, could be placed so that the flow patterns at any position between 12 and 32 ft from the diaphragm could be studied.

Since the origin problem (that is, the flow processes which occur immediately the diaphragm is ruptured) of shock-tube flow formation had been previously studied[12, 14], the length of the non-interchangeable diaphragm-joint section was determined solely by the condition for the production of a plane shock wave travelling down the tube; namely, that the length should be approximately 20 times the largest cross-sectional dimension[4]. Hence the selected length of this section was 12 ft.

In the original design proposals, thermocouples were included to measure the initial temperatures of the gases in the chamber and the channel. Later, it was decided that the thermocouples were an additional complication in an apparatus which already posed considerable physical problems for a single operator. Moreover, before each test, the gases in the shock tube were allowed to come to thermal equilibrium, that is, room temperature. For these reasons, the thermocouples were deleted from the installation and the calculations of Chapter 4 carried out with $T_0 = \bar{T}_0 = 288°K$.

A detailed description of the installation follows—the shock tube proper in the remainder of the present Chapter and the electronic and optical equipment in Chapters 7 and 8 respectively.

6.2. *Detail Design and Construction.*—6.2.1. *The Chamber* (Fig. 32).—A simple wooden construction, such as Fig. 28e, will not withstand a pressure of 200 lb/sq in.; hence the chamber was fabricated from a steel pipe*, 4 ft in length, $8 \cdot 12$ in. internal diameter and $0 \cdot 277$ in. wall thickness. Steel flanges*, $0 \cdot 5$ in. thick, $13 \cdot 25$ in. diameter, having $8 \frac{11}{16}$-in. holes equally spaced on an $11 \cdot 5$-in. pitch circle diameter, were circumferentially fillet-welded to the pipe at its ends. Two steel end plates*, $0 \cdot 5$ in. thick, were drilled to mate with the flanged ends of the pipe and gasket slots, $\frac{1}{2}$ in. wide, $\frac{1}{8}$ in. deep and $9 \cdot 95$ in. mean diameter were milled in the flanges and the endplates.

---

* Manufactured by Bristol Piping Co., Ltd., 75 King Street, Bedminster, Bristol, 3.

The standard 6 in. by $2\frac{1}{2}$ in. cross-section of the shock tube was preserved by inserting 'drive-fit' shaped wooden liners into the steel pipe. To facilitate the changing of diaphragms the chamber was mounted in two supports, the castors of which ran in two 1-in. by 1-in. steel channels, 5 ft in length, parallel to the longitudinal axis of the shock tube (*see* Fig. 32). A safety valve set at 200 lb per sq in., the high-pressure air inlet pipe and the outlet pipe to the gauge panel were mounted on the end plate of the chamber remote from the diaphragm. Flexible pipes were used for these connections so that the movement of the chamber during the replacement of a diaphragm did not fatigue the pipework.

We have noted that, preferably, the length of the chamber should be variable. It was hoped that wood blocks of 6 in. by $2\frac{1}{2}$ in. cross-section and of various lengths might be inserted in the chamber to reduce its effective length; but, through an unfortunate oversight in the design, this was not possible. Such a scheme required that the high-pressure air inlet should be adjacent to the diaphragm—contrary to the configuration described above.

6.2.2. *The Diaphragm Joint and Section* (Fig. 33).—Speedy replacement of diaphragms is a prime requirement of shock-tube operational technique, consequently six 'Speetog'* toggle-action clamps rigidly held the diaphragm joint during a test. The diaphragm striker was constructed of mild steel and operated by three springs. These springs are tensioned and held in position by a distance piece until a Bowden cable pulls the distance piece aside and the springs contract, causing the striker to rupture the diaphragm (which is assumed to bow 1 in.), at its centre. The striker was silver-soldered to a $6\frac{1}{2}$ in. by $4\frac{1}{2}$ in., $\frac{1}{4}$-in. thick, steel plate which was screwed to the channel. This plate, and other similar plates on which were mounted the air inlet valve V_4 (Fig. 30) and the main vacuum pump (Edwards Type 1SP30) line and gauge connections, were grooved to receive $\frac{1}{4}$-in. square rubber gaskets. All openings into the channel had fine mesh gauzes incorporated so that debris from shattered diaphragms could not enter the vacuum pumps or block valves.

Fig. 33 illustrates most of the above features and also shows the construction of the mating face of the channel in detail. The four bolts shown are tightened to stop small leaks round the periphery of the diaphragm when high pressures are used in the chamber. A $\frac{1}{4}$-in. thick 'sorbo' rubber gasket fits into the recess in the mating face and the diaphragm is placed between this gasket and a $\frac{1}{16}$-in. rubber sheet glued to the steel flange of the end of the chamber. (This sheet has been removed in Fig. 32.)

6.2.3. *The Interchangeable Channel Sections.*—Fig. 28e shows how the channel sections of the shock tube were constructed from $1\frac{3}{8}$-in. thick seasoned mahogany planks, glued, screwed and jointed together. Simple butt joints with positive locating projections were used to assemble the individual sections of the channel such that the cross-section was sensibly constant along the tube. A typical joint is illustrated in Fig. 34, this view showing the end of the ultimate channel section and, above, the associated mating end plate of the tube. The latter has a central hole, protected by a fine mesh gauze cone, which is connected to either an Edwards Type 1S50 or a 'water-jet' type vacuum pump. Two of four 'Speetog' toggle-action 'C'-clamps which are used to hold the end plate securely to the tube are also shown in Fig. 34. These quick-release clamps make the removal of debris from the tube (by 'flushing' with high pressure air) a very easy process. The channel end plate pictured in Fig. 34 was one of a pair of mating master blocks (the other was similar to the end of the channel proper) used in the construction of the channel. The ends of each individual channel section were made to mate accurately with these two master blocks and hence all the channel joints had a standard fit (with this type of joint the sections are of course not reversible end to end, but this is of no practical importance in this case). All joints were grooved to take $\frac{1}{4}$ in. by $\frac{1}{4}$ in. rubber gaskets, and the 'positive location' beading also helped to ensure a vacuum tight joint (*see* Fig. 34). Since the support for the tube was effectively continuous (*see* Section 6.3.1) there were no high bending moments acting on the joints, and hence four 2BA bolts, acting through holes drilled in four pairs of small mating aluminium angles attached to the channel sections to be joined, were all that were required to draw the joints together (*see* Figs. 34 and 35).

* Manufactured by Speed Tools, Ltd., Gresse Street, London, W.1.

33

One of these sections, namely, that 4 ft in length, was slightly modified so that it became the 'light-screen' section. Three pairs of 2 in. diameter, $\frac{3}{4}$ in. thick, optical-quality glass windows were glued into recesses in the section so that the internal cross-section remained constant. Fig. 52 illustrates a typical light screen, and shows how the tube walls were cut away to leave 1 in. diameter 'peepholes' through which the 1 in. by $\frac{1}{16}$ in. light beam of the miniature schlieren system traversed the tube. Three pairs of light screen windows W_A, W_B and W_C were provided so that the velocity and acceleration of the shock wave were measurable, and the window centre line distances $W_A W_B = W_B W_C = \frac{1}{2} W_A W_C = 18$ in.

6.2.4. *The Working-Section.*—This section, illustrated in its final form in Fig. 35, was constructed in a similar manner to that employed by the present writer in the 4 in. by $1\frac{3}{4}$ in. shock tube working-section described in Ref. 22, save that the construction material in this case was wood instead of steel. In its original form, the sides of the working-section were two $22\frac{1}{2}$ in. by 8 in., $\frac{1}{2}$-in. thick ordinary plate glass slabs, mounted in two 24 in. by 10 in. wooden frames. These frames were spaced $2\frac{1}{2}$ in. apart by two solid 2 in. by $2\frac{1}{2}$ in. by 24 in. mahogany longerons 6 in. apart; the complete assembly was screwed together so that the 6 in. by $2\frac{1}{2}$ in. internal cross-section was preserved and over a 21-in. length the whole 6-in. height of the channel was observable.

With the above arrangement, the changing of models in the working-section necessitated breakage of two channel joints, a time-wasting process since there was usually considerable difficulty in making these joints vacuum tight. Hence a 'door' was incorporated in this section to obviate the above difficulty. At first this door hinged downwards, but was later merely clamped in position by quick-action toggle-type clamps. This final arrangement is shown in Fig. 35. Angle section steel stiffeners are noticeable in the photograph; these minimized distortions of the door and, hence, leakage troubles. The glass plates were mounted in their frames by 'Bostik' and thin rubber sheet, approximately $\frac{1}{64}$ in. thick, prevented leaks between the longerons and the side walls of the section.

6.3. *Assembly of Installation.*—6.3.1. *Layout in Laboratory.*—Fig. 29 illustrates how the tables 'A', 'B' and 'C' were used to maintain the shock tube at a uniform level, and shows the layout of the optical and electronic equipment tables. 'Dexion' longerons joined up all the individual wooden channel supports (see Fig. 36), and the whole assembly was rigidly connected to the concrete floor. The individual channel sections were assembled so that no undue strains were present at the joints; in particular, the longitudinal centre-line of the tube was corrected to a stretched piano wire and the general level of the tube checked by spirit level at frequent intervals. The chamber was constrained to move in channels which were aligned to give accurate mating between the high- and low-pressure sections at the diaphragm joint.

6.3.2. *Preliminary Assembly Testing.*—All vacuum tubing, pressure piping, gauges, valves and air supplies were connected as detailed by Fig. 30. Leak tests were made on all connections and the operation of the vacuum pumps, air compressor and diaphragm striker checked. Full details of all the preliminary tests carried out before the calibration of the tube was commenced are deferred to Chapter 9, following the description of the optical and electronic recording equipment.

CHAPTER 7

Electronic Equipment

The extremely limited duration of the flow processes occurring in a shock tube necessitates the use of electronic chronometer equipment to provide an accurate time history of the flow phenomena. In particular, it is necessary to obtain the shock speed (V_+) in almost all applications of the shock tube and it is also very desirable to be able to take timed photographs of the flow patterns.

Aerodynamic phenomena have been used[19, 22] to obtain shock speeds and timed photographs of the flow, but it is the experience and opinion of the present writer that these methods are not sufficiently accurate; for example, it is not possible to deduce shock speeds from photographs of the flow patterns to better than 2 per cent, whereas the electronic equipment described below enables the shock speed to be determined to within 0·25 per cent. Further, the timing of photographs by the use of mechanical pressure switches is likely to involve considerable errors due to the inherent inertia of the diaphragm of the pressure switch. The present writer obtained[22] variations of $\pm$ 50 μsec during work on such mechanical switches. An inertialess beam of light and a photocell may be used as an electronic switch with an accuracy of better than $\pm$ 1 μsec. [It is admitted that the above rather crude mechanical switch[22] could be improved to give better reproduceability but the inherent drawback remains.]

The present shock-tube installation was therefore fitted with complete electronic equipment so that experimental results would involve as small an error as possible.

7.1. *The Measurement of Shock Speed*.—A block schematic diagram of the basic function of the electronic instrumentation, namely the measurement of the primary shock-wave velocity, is given in Fig. 37.

The operation of the 'light-screens' L_1, L_2, which are miniature schlieren systems will be fully described in Chapter 8, Section 8.2. Here it is only necessary to note that the passage of the shock wave past L_1 causes an increased illumination to fall on the sensitive cathode of photocell P_1, thus giving rise to a voltage pulse which, after modification, starts the electronic chronometer. When the shock passes an identical light screen L_2 a pulse is produced which stops the chronometer. Then, since the time interval (measured directly by the chronometer) and the distance between the light screens are accurately known, the shock velocity is determinable. The apparatus used for this function will now be described in detail.

7.1.1. *The Microsecond Counter Chronometer**.—This chronometer is essentially a high-speed electronic stop-watch capable of measuring very short time intervals with a high degree of accuracy. The time interval measured is indicated directly on six meters† each scaled 0 to 9 (*see* photograph Fig. 38), and remains displayed until the Reset button is pressed. Manual 'test' stop and start push buttons are provided.

The complex nature of this instrument is such that development time would have been too long for the chronometer to be built as part of the electronic programme. A block diagram of the chronometer is given by Fig. 39. It is noted that the circuit contains two crystal-controlled oscillators, an electronic gate, six decades and a stabilized power supply. The switch S enables any available frequency to be selected, thus choosing the maximum measurable time interval. In the following experimental work only the 1 Mc/s position is used, giving a timing range of 0 to 0·999999 second, in steps of 10^{-6} second.

On receipt of a start pulse, the gate is opened and the decades count the individual cycles (each 1 μsec) from the oscillator. This continues until a stop pulse is received, when the gate shuts and the meters indicate the number of cycles executed by the oscillator, that is, the number of microseconds (μsec) in the measured time interval (subject to a 1 μsec error). The chronometer requires start and stop pulses of amplitude 10 $\rightarrow$ 40 volts and having a rise time of less than one microsecond.

7.1.2. *The Photocell Equipment*.—7.1.2.1. *The Photocell Units*.—The general principles of photoelectric cells are well known[29] and, again in an endeavour to reduce development time for the electronic equipment, commercial photocell units‡ and power supplies‡ were obtained.

---

* Manufactured by Cinema-Television, Ltd., Lower Sydenham, London, S.E.26, and supplied by D.S.I.R. under the special apparatus scheme.

† In Fig. 38 one meter has been removed for repair.

‡ Manufactured by AIRMEC, Ltd., High Wycombe, Type 805 and Type 811 respectively.

35

The photocell units comprise a Mullard 90CG gas-filled photocell sensitive to incandescent sources, with a pentode EF91 connected as a cathode follower, and give a positive pulse output for an increase of light falling on the photocell. Fig. 40 gives the circuit diagram of these units and a photograph appears as Fig. 38.

7.1.2.2. *Pulse Modification.*—The duration of the output pulse from the photocell depends on the time taken for the shock to pass the light screen—a beam of light $\frac{1}{16}$ in. wide. This may be of the order of $2 \rightarrow 3\ \mu\text{sec}$, whereas the chronometer requires a pulse having a rise time of less than $1\ \mu\text{sec}$. We can ensure this by using a thyratron as an electronic switch, giving a rapid rise step pulse to operate the chronometer[30].

The positive pulse applied to the thyratron grid V_2 (Fig. 40) will cause the valve to 'fire' (that is, to conduct) if the pulse is of greater amplitude than the standing negative grid bias on the valve. In this case, a positive pulse appears across the cathode resistor R_7 and this is fed directly to the chronometer. The circuit may be reset by opening switch S, which when reclosed leaves the circuit in the 'ready-to-fire' condition. For a sharp output pulse, the screened leads from R_7 to the chronometer, must be as short as possible. Both thyratron circuits were mounted on the same chassis (*see* Fig. 38).

7.1.2.3. *Power Supplies.*—Various power supplies were required for the above equipment. Commercial units provided:—

AIRMEC 811	140v H.T.	30mA	Smoothed
	12v D.C.	0·6A	Smoothed
	6·3v A.C.	1·0A	Unsmoothed
EDISWAN R1103	250–400v H.T.	150–200mA	Stabilized
	6·3v 6A A.C.		Unstabilized

A filament transformer gave 4v 4 amps for the thyratrons GTIC.

7.1.2.4. *Operational Difficulties.*—The above circuits, whilst moderately sensitive to light fluctuations, did not prove reliable in operation. In particular, any mechanical vibration would cause the thyratrons to fire and, further, stray pulses caused by 'resetting' one circuit by switch S would frequently fire the other thyratron. In an attempt to have greater control over the thyratron circuits a stage of amplification of the photocell output was built into the unit before the thyratron stage. This proved ineffective at first but, later, careful screening of leads and the use of decoupling condensers to earth at various points in the circuit led to the elimination of the interference between the two thyratron circuits. This screening also decreased 'hum' pick-up from other equipment. Vibration troubles were also eliminated (*see* Chapter 8, Section 8.2) and it was then found that these units would not detect the shock at all. Previous 'results' could all be attributed to spurious counting of the chronometer due to the vibration and interference effects mentioned above.

Subsequently the photocell units were made sensitive to RATE of change of light by incorporating the $R_D C_D$ differentiating network in the grid circuit of the cathode follower valve V_1 (*see* Fig. 40). No improvement was noted. It was found that the photocell units were not working at their maximum efficiency; in particular, the anode voltage on the photocell was insufficient. Higher anode voltage improved the pulse voltage, but the units still would not detect the passage of the shock.

At the same time, the optical part of the light screens had been developed to maximum efficiency (*see* Chapter 8, Section 8.2). The only further improvement which could be made in order to increase the sensitivity of the equipment concerned the photocells themselves. The Mullard 90CV vacuum photocell has a sensitivity of 150 μA/lumen (*cf.* 90CG 125 μA/lumen), that is, it produces a current of 150 microamps for every lumen of light incident upon it and pro rata. The 90 CV is sensitive to blue light (i.e., mercury vapour lamps such as the 'Mazdalux')

which would also give increased sensitivity due to its greater wattage (250) than the tungsten lamp (50 watt) used with the 90CG photocells. Even this factor of 6 : 1 increase on the sensitivity did not seem to the writer to promise satisfactory operation, and then, a chance reference in the literature on schlieren systems[31] led to the 'discovery' of photomultiplier tubes with a sensitivity of $2 \times 10^6 \mu$A/lumen, an increase of 10,000 times on the previous photocell sensitivity.

It is unfortunate that references in shock tube literature to light screens have referred to photocells more often than to the correct name of photomultiplier tubes, and the present writer was at fault in not knowing of the difference between the two. It will therefore be appreciated that the commercially obtained photocell units are not suitable for this type of application but may be valuable in other experiments where the changes in light intensity are of a greater order. Consequently these units were retained as a separate piece of equipment for possible further use. Entirely new photomultiplier equipment for shock detection using light screens was then designed and built.

7.1.3. *The Photomultiplier Equipment.*—7.1.3.1. *The Photomultiplier Tubes.*—These are Mazda type 27M2, responsive to the visible spectrum and requiring a power supply of 1,000 v at 2mA. The overall sensitivity is $2 \times 10^6 \mu$A/lumen at 800v. This enormous increase in sensitivity over the more widely used photocell is achieved by using the effect called 'secondary emission'. That is, the photoelectrons emitted by the cathode strike a secondary electrode (dynode), positive with respect to the cathode. This in turn emits, say, double the number of photoelectrons, and then the process is repeated, usually nine times. Consequently the extreme sensitivity of the tube depends on the number of stages and the volts per stage. It is important not to 'overload' the tube, hence these photomultiplier tubes are only of use when very small changes of light have to be measured.

·7.1.3.2. *Circuit Diagrams of the Equipment.*—Block schematic and detail circuit diagrams of the photomultiplier units are given by Figs. 41 and 42 respectively. The power unit supplies 1,200 volts, but adequate control of the volts/stage and hence the overall sensitivity of the photomultiplier tubes is obtained by using the variable resistances R_{10} and R_{11}. Fig. 43 is a photograph of the units in position in the installation.

The operation of these circuits is very similar to the photocell units previously described; the output pulse from the photomultiplier tube is amplified, differentiated and sharpened before being fed to the chronometer exactly as before. In this circuit the thyratron is automatically 'reset'. These circuits were designed by combining features found in several reports from North America.

7.2. *Timed Photographs of Flow Patterns.*—The chronometer may be used to determine the precise instant relative to a given datum (say when the shock passes light screen L_1) at which a photograph of the flow in a shock tube was taken. A block schematic diagram of this function is given in Fig. 44. In theory, after the calibration of the time-delay circuits, the chronometer is merely needed for occasional checking purposes; however, in the following experiments, the chronometer is always used—*see* Chapter 9.

7.2.1. *The Phantastron Time Delay Circuits.*—Fig. 45 is a complete circuit diagram of the final form of the time-delay unit and the associated pulse sharpener and output thyratrons. The basic phantastron time-delay circuit is fully described in Ref. 32, which is, however, very specialised and the following brief explanation of the mode of operation of the circuit may be helpful.

Refer to Fig. 45; in the normal quiescent condition the pentagrid valve V_1 has no current flow in its anode circuit since a standing bias exists on the control grid (3) with respect to the cathode via R_2. Application of a pulse input to grid 3 causes current to flow in the anode circuit; consequently the charge on condenser C_g leaks away through resistances R_{g1}, R_{g2} until the voltage of grid 1 is such that the anode circuit is again cut off and the valve V_1 resumes its quiescent state. A further pulse—the output pulse—is formed as the valve V_1 returns to the quiescent condition, and this may be developed across R_6 or R_7 as the pulse to be fed to the next stage

37

of the unit. The cycle of operations from one stable quiescent state to the next constitutes the time delay of the circuit and this time delay depends solely on the charge on C_g and the values of R_{g1}, R_{g2} and C_g.

For given values of R_g and C_g the maximum delay is given by (Ref. 32, p. 104),

$$T_{max} = R_g C_g (V_{max} - V_0)/E_{bb} \qquad \cdots \qquad \cdots \qquad \cdots \qquad \cdots \qquad \cdots \qquad (7.1)$$

where $\qquad V_{max} =$ voltage at HT side of R_{10}

$\qquad V_0 =$ voltage at earth side of R_{10}

and $\qquad E_{bb} =$ supply HT voltage.

For the circuit detailed in Fig. 45, the quantity

$$(V_{max} - V_0)/E_{bb} \simeq \tfrac{1}{2}; \quad \text{then } T_{max} = \tfrac{1}{2} R_g C_g. \qquad \cdots \qquad \cdots \qquad \cdots \qquad (7.2)$$

Any delay from 0 to T_{max} may be obtained by varying the charge on C_g, that is, by altering R_{10} suitably, and hence controlling the anode voltage of V_1 via V_2. The main advantage of the phantastron over other time delay circuits is that the delay varies *linearly* with the setting of the accurate potentiometer R_{10}. For example, if $R_{10} = 20,000\Omega$ and $T_{max} = 20,000$ microseconds any intermediate delay would be obtained by setting R_{10} in a 1 : 1 ratio.

To recapitulate, the values of R_g and C_g determine the maximum delay available in the circuit and the setting of the potentiometer R_{10} controls the actual delay.

7.2.2. *Development of the Delay Circuits.*—Two phantastron circuits were constructed using component values quoted in Table 2 of Ref. 32, p. 105. These circuits were to have delays of 500 μsec and 10,000 μsec.

Once again, the pulse output from these circuits would not operate the chronometer satisfactorily, and so thyratrons V_3 were added to the units to provide a step pulse output as in the photomultiplier units.

The final pulse output from the time-delay unit was also required to trigger the light source so that a photograph of the flow could be taken at any predetermined instant. It was found that the thyratron V_3 could not pass the current generated when the light source was triggered, hence a further power thyratron V_4 was incorporated in the circuit. When the thyratron V_4 is fired by the output pulse from the phantastron, condenser C_4 discharges through the pulse coil of the flash unit, thus triggering the light source in the desired manner—*see* Section 7.3. Thyratron V_3 provides an output pulse which may be fed to the chronometer for test purposes.

Details of the calibration of the time delay circuits are reported in Chapter 9.

7.3. *The Electronic Flash Equipment.*—7.3.1. *The Mullard LSD–2 Unit.*—This unit has been described in detail in an earlier report[22] by the present writer. Certain modifications have been made to the circuit, however, and these are detailed below and in the modified circuit diagram of the unit (Fig. 46).

(1) The unit has been earthed (point B). This gives more positive protection for the operator and also more consistent triggering of the flash tube.

(2) A 210-volt, 50-cycle supply is now used, giving approximately 6,000 volts on the anode of the LSD–2.

(3) Leads for an FA–5 flash tube (*see* Section 8.2) have been taken from points G (2,000 volts-anode) and B (earth-cathode).

(4) A co-axial lead (6,000 volts) for the spark discharge unit (*see* Section 7.3.3) has been taken from points A (core) and B (sheath-earth).

These modifications are illustrated in Fig. 47.

7.3.2. *Comparison of Flash Sources.*—The salient features of each type of source for instantaneous photography are given in the following table :—

Source	Operating voltage	Energy of flash (Joules)	Average life (flashes)	Source size millimetres	Approx. duration μsecs.
LSD–2	6,000	24*	10,000	35 × 5	3
FA–5	2,000	8*	5,000	5 × 3	10
Spark	12,000	3·6	1,000	2 mm. dia.	1

The large source size of the LSD–2, combined with a tendency for the arc to wander round the glass envelope of the tube makes this source only moderately suitable for shadow/schlieren photography. Much of the available light energy is wasted. The FA–5 has a small source size and is very consistent in operation; however the flash duration is rather long and photographs of shock waves lack definition due to movement blurring of the image. A spark gap is the most useful source : it has small size, short duration and utilizes most of the available energy.

7.3.3. *The Spark Source Unit.*—High voltages are required to operate air spark-gaps efficiently and to ensure that the spark has a very short duration (of the order of one microsecond or less). An ingenious arrangement whereby two condensers are charged in parallel and discharged in series enables the flash unit described above to operate a spark-gap at 12,000 volts. The circuit diagram† of this spark unit is given in Fig. 48 and a photograph of the unit is also appended (Fig. 47). The existing flash unit was utilised as far as possible, and the trigger-gap was made to fit into the LSD–2 socket.

Thick-walled Pyrex glass tubing, drilled to accommodate the trigger electrode, enclosed the trigger spark-gap, and the steel electrodes of this gap were fitted in brass collars equipped with locking bolts. In this manner, the spark-gap was more reliable than an unconfined air-gap and the length of the gap was easily adjustable—*see* photograph (Fig. 47). The main spark-gap was also enclosed in a Pyrex glass tube, but here the light from the spark emerged through a hole drilled in a steel plate electrode, thus providing a point source for shadow or schlieren photography.

7.3.3.1. *Operation of the Circuit* (Fig. 48).—The condensers C_1 and C_2‡ are charged in parallel to 6,000 volts through the charging resistor R_1§ and the surge resistor R_5. When a pulse is applied to the trigger gap it breaks down (*i.e.*, fires) and so completes a circuit consisting of itself, condenser C_1 and the surge limiting inductance L. The resulting oscillatory discharge reverses the polarity of C_1 after the first half cycle. At this point the polarities of the condensers C_1, C_2 are series additive, that is, nearly 12,000 volts is applied across the main spark-gap.

This voltage pulse breaks down the main gap and the two condensers discharge in series through the main ' light ' gap. This circuit is very reliable since the voltage pulse applied is well above the static breakdown potential of the light gap (about 9,000 volts).

---

* Assuming only 66 per cent of energy in condensers is dissipated in the actual discharge.

† Developed during private communications between the writer and R. J. North of the National Physical Laboratory.

‡ Supplied by the Wego Condenser Co., Ltd., Perivale, Middlesex. Type 2416. Special non-inductive D.C. pulse condensers, 0·1 mfd.

§ *See* Fig. 46.

CHAPTER 8

Optical Equipment

This chapter describes the two optical systems developed for the shock-tube installation; namely, the main system used in the photography of shock-tube flow and the 'light screens' developed to measure the speed of the primary shock as it progresses down the tube.

8.1. *The Main Optical System.*—Because the shock tube was positioned near one wall of the laboratory (*see* Fig. 29), a single mirror, double pass, shadow/schlieren optical system had to be employed. The schematic layout of such a system is shown by Fig. 49.

Since the basic features of the schlieren method are well known, we will merely restate some of the more important details given by Holder and North[33] and adapt their results for a twin-mirror system to the single-mirror system employed in these experiments.

In the first instance, suppose the condenser lens is not included in the system shown in Fig. 49.

If E_0 is the illumination of the image (size $b \times h$) and E is the illumination of the source, then, assuming no losses,

$$E = \frac{a}{h} \cdot E_0 \qquad \qquad \qquad \qquad \qquad \qquad \qquad (8.1)$$

since the knife edge K_1 is introduced a distance ' a ' into the image in the ' h ' direction.

Now a gradient of density in the shock-tube working-section will deflect a light ray through an angle $2d\varepsilon$ (double-pass system) and the corresponding part of the image will move through a distance $2d\varepsilon \cdot 2f_1 = 4f_1 \, d\varepsilon$. Consequently the illumination of the image changes by

$$\delta E = \frac{4f_1 \, d\varepsilon}{h} \cdot E_0 . \qquad \qquad \qquad \qquad \qquad \qquad (8.2)$$

Then, from (8.1) and (8.2)

$$\frac{\delta E}{E} = \frac{4f_1 \cdot d\varepsilon}{a} . \qquad \qquad \qquad \qquad \qquad \qquad (8.3)$$

which is defined as the contrast δC.

Further, the sensitivity S is given by

$$S = \frac{dC}{d\varepsilon} = \frac{4f_1}{a} . \qquad \qquad \qquad \qquad \qquad \qquad (8.4)$$

To keep the sensitivity as defined by (8.4) the maximum range of displacement of the image ($\overline{\delta\varepsilon}$) cannot exceed the height of the image h, and, further, the sensitivity should be the same for deflections either on to or away from the knife edge K_1. Then

$$a = \frac{1}{2} h; \; E = \frac{1}{2} E_0 \text{ and } 4f_1 \overline{\delta\varepsilon} = h . \qquad \qquad \qquad \qquad (8.5)$$

From (8.4) and (8.5) we have $S = \dfrac{2}{\overline{\delta\varepsilon}}$, $\qquad \qquad \qquad \qquad \qquad (8.6)$

the sensitivity is inversely proportional to the maximum range of the system, a result which holds for all types of schlieren systems.

When a condenser lens is used, the magnification of the source m_c is given by

$$m_c = p/q \quad \ldots \quad \ldots \quad \ldots \quad \ldots \quad \ldots \quad \ldots \quad \ldots \quad \ldots \quad (8.7)$$

and the focal length of the condenser lens f_c is given by

$$f_c = \frac{m_c q}{m_c + 1} \cdot \quad \ldots \quad \ldots \quad \ldots \quad \ldots \quad \ldots \quad \ldots \quad \ldots \quad (8.8)$$

Further, for maximum utilisation of the available light

$$\frac{f_1}{d} = \frac{p}{d_c} \, (see \text{ Fig. 49}) . \quad \ldots \quad \ldots \quad \ldots \quad \ldots \quad \ldots \quad \ldots \quad (8.9)$$

We may also note that the modified range is $m_c \overline{\delta \varepsilon}$, but the modified sensitivity

$$S = \frac{2}{m_c \overline{\delta \varepsilon}} \quad \ldots \quad \ldots \quad \ldots \quad \ldots \quad \ldots \quad \ldots \quad \ldots \quad (8.6A)$$

and the contrast remains unchanged. Thus the use of a condenser lens with $m_c > 1$ gives greater illumination of the image, greater range and smaller sensitivity.

Finally, the camera lens L_2 focusses an image of the disturbance in the working-section on to the camera plate C. Then

$$\frac{1}{f_2} = \frac{1}{(2f_1 + d)} + \frac{1}{e} \cdot \quad \ldots \quad \ldots \quad \ldots \quad \ldots \quad \ldots \quad \ldots \quad (8.10)$$

This lens is usually about $+ 1 \cdot 0$ dioptre power.

8.1.1. *Practical Details of Main System.*—It was found impossible to satisfy simultaneously the many requirements detailed above, and a system was set up using available components as follows :—

Main mirror M_1 diameter $d = 12$ in.

           focal length $f_1 = 6\frac{1}{2}$ ft

Condenser lens L_c diameter $d_c = 1 \cdot 25$ in.

           focal length $f_c = 5$ in.

Magnification of source $m_c = \dfrac{p}{q} = \dfrac{10}{9} = 1 \cdot 1$

Source size—*see* Section 8.2.

The plane mirror M_2 was necessary because of space considerations, likewise the 45-deg prism attached to the adjustable primary slit S. A 'pinhole'-type camera, constructed during earlier experiments, used Ilford Zenith $\frac{1}{4}$ plates in a special holder.

Camera lens L_2 focal length $= 39$ in. (that is, power in dioptres $= + 1 \cdot 0$).

The distances $d = 7$ in.

and $e = 52$ in. satisfy (8.10).

The image on the camera screen is approximately $\frac{1}{4}$ actual size—this is in accordance with N.P.L. practice.

When a point light source was used a graded filter[34]* was found preferable to the knife edge K_1.

* Supplied by the N.P.L.

8.2. *Light Sources.*—Various continuous sources were available for use with the above optical system and their salient properties are summarised in the following table :—

Type	Wattage	Efficiency lumens/watt	Source size (mm)	Life (hours)	Cost (including starting circuits) £	Operating current (Amps)
Tungsten lamp	50	10	$5 \times 1\frac{1}{2}$	50	$\frac{1}{2}$	5
FA–5	150	30	5×3	200	12	10
Mazdalux	250	50	$3\cdot75 \times 1\cdot5$	500	35	5
Pointolite	150*	10	2·5 mm dia.	200	7	2
Zirconium arc†	300	15	3 mm dia.	1,000	50	15

* Candle power.

† Not available, but included to complete table. Note small source size, very long life, good efficiency and prohibitive cost.

8.2.1. *Mazdalux Circuit.*—This source has a very high efficiency and light output, and may be started very easily. A special choke, in series with the lamp, is the only additional component required. Unlike the Pointolite or other tungsten filament projector lamps, the extreme brilliance of the Mazdalux allows an optical system to be set up without the need to darken the laboratory.

8.2.2. *Mazda FA–5 Circuit* (Fig. 50).—The FA–5, although primarily intended for flash operation (*see* Section 7.3), may also be used as a continuous source. This is very convenient in use, since we do not require the replacement of the 'setting-up' continuous source by a flash source and the consequent possibility of misalignment of the equipment is avoided. Connections to the anode and cathode of the FA–5 may be taken from the electronic flash unit or from the separate starting circuit (described below) whilst the lamp remains fixed.

For this continuous source application the FA–5 requires a special starting circuit to initiate the discharge, and, although this arrangement is a little tricky to operate, it has proved very satisfactory in service. The sequence of operations is as follows:—

(1) Commence with switch S_1 closed, switch S_2 open and R_1 adjusted to $2 \rightarrow 3$ ohms (*see* Fig. 50).

(2) By rapidly closing and opening switch S_3, apply a trigger pulse ($\simeq$ 5,000 volts) from the 6-volt car battery via the car ignition coil to the trigger electrode of the FA–5.

(3) Immediately the arc strikes, increase R_1 to 12 ohms, close switch S_2, open switch S_1 and decrease R_1 to 2–3 ohms again. This sequence must be carried out quickly, otherwise the FA–5 may pass a very large current (up to 30 amps). Under normal running conditions the resistance in the circuit $\simeq$ 22 ohms, hence limiting the current to the rated value 10 amps.

A photograph of this equipment appears as Fig. **51**.

8.3. *The Light Screens.*—During the development of these units several interesting features of schlieren systems were emphasised and are worthy of note.

42

Fig. 52 is a general arrangement drawing of a light screen and shows its position relative to the shock tube. P is a steel plate, measuring 42 in. by 3 in. by $\frac{5}{16}$ in., having three slits A, B and C each $\frac{1}{16}$ in. by 1 in. spaced symmetrically at $18 \pm 0\cdot001$ in. intervals along the plate, that is, AB $=$ BC $= \frac{1}{2}$AC $= 18$ in.

In this way we may deduce the acceleration of the shock over the distance AC from three separate measurements of its speed. Only two moveable light screens are required.

Again in Fig. 52, lenses L_1 and L_2 form a conventional schlieren system, complete with condenser lens L_c, slit S and knife edge K_1. The light beam, $\frac{1}{16}$ in. wide and 1 in. high, traverses the shock tube at right-angles to the direction of shock propagation. As is well known, when the shock passes the light screen the beam is deflected towards the region of higher density, that is, towards the chamber of the shock tube. Hence, with the arrangement shown, the beam is deflected off the knife edge K_1 and falls on to the photosensitive cathode of the photocell or photomultiplier tube P_1, thus operating the electronic chronometer as described in the previous Chapter 7. A specially constructed shield completely encloses the photocell except for a very small aperture which is placed adjacent to the knife edge.

When first set up the light screens were placed on the tables which support the shock tube (*see* Fig. 36) and the plate P was screwed to the shock tube so that the slits A, B, C were in alignment with the 'peephole' light screen windows $W_A W_B W_C$ respectively of the light screen section of the channel.

Calibration tests were commenced but the results obtained were incredibly erratic. These spurious results were traced to mechanical vibration of the shock tube, the table and the electronic equipment. Consequently the light screens and the plate P were attached to inverted optical benches for rigidity and easy adjustment and then mounted on a rigid 'Dexion' framework affixed to the wall of the laboratory. Later, the photomultiplier units were likewise mounted on this framework. This final arrangement is illustrated in Fig. 53.

It has previously been stated that when these vibration troubles had been overcome, but before the changeover from photocells to photomultiplier tubes, the light screens would not detect the passage of the shock. In an endeavour to obtain greater sensitivity from the optical system, an exhaustive analysis was made of the optics of the light screens and this proved most instructive.

Several of the more important points arising* are noted below.

(*a*) It is important to ensure that the light beam traverses the shock tube exactly at right-angles to the direction of shock propagation. Calculations based on work by Mair[35] indicate that if the beam is more than two degrees out, deflections due to the passage of the shock would be almost completely nullified. Great care was taken and a special checking plate made to achieve accurate alignment of the light beams.

(*b*) Lens quality does not matter and the aperture is important only as far as light gathering power is concerned. Further, there is no advantage in small lenses for these 'miniature' schlieren systems.

(*c*) Formula (8.4A) $S = \dfrac{2f_1}{m_c h}$ can be misleading. The quest for greater sensitivity would lead to making m_c very small. It is, however, most inefficient to use a condenser system at magnifications of less than unity; most of the light is being wasted.

(*d*) In the light screens, $f_1 = f_2$ and the above formula would appear to show that if f_2 were increased, the sensitivity would increase also. In fact, the change in illumination at the photocell is independent of the focal length of L_2 because increasing it increases the displacement for a given deflection, but it also increases the size of the image of the source and decreases its brightness in proportion.

Full details of the components used in the light screens are given by Fig. 52.

CHAPTER 9

Calibration of the Shock-Tube Installation

9.1. *Preliminary Experiments.*—9.1.1. *Leak Testing of Shock Tube, Gauges and Pipework.*—9.1.1.1. *Chamber.*—The end of the chamber which normally butts against the channel was blanked off by a steel cover plate and air at 250 lb per sq in. (gauge) was slowly admitted. No leaks were observed and the safety valve was adjusted to operate at 200 lb per sq in. When the chamber was examined after repeated tests of this nature, no sign of wood failure was noted; in particular, the ' bursting ' of wood cells which have been subjected to high pressures and then suddenly returned to atmospheric conditions was absent.

9.1.1.2. *Channel.*—High-pressure air was allowed to fill the shock tube to 10 lb per sq in. (gauge); note that this corresponds to the final pressure existing throughout the tube after a test run with $\bar{p}_0 = 200$ lb per sq in. and $p_0 = 1$ in. of mercury. Leaks in the channel were detected with soapy water in this manner and then sealed. Several channel joints exhibited leaks which were eliminated by fitting extra $\frac{1}{32}$-in. or $\frac{1}{16}$-in. thick rubber strips round the periphery of the joint. Shellac was found to be a useful sealing agent for small leaks along the longitudinal joints of the tube, whilst Plasticine was used freely when the exact location of a leak could not be found. Occasionally, a stethoscope was found useful for the detection of small leaks.

When the vacuum pumps were switched on for the initial evacuation of the channel, it was found that the leaks into the channel nullified the effects of the pumps. Many hours were spent searching for leaks and finally a stage was reached when no further improvement could be obtained using shellac, Plasticine and vacuum grease. The ultimate vacuum achievable in this way was 24 mm of mercury (*see* Fig. 55). It appears that, to some extent, wood will always remain porous, even when painted or varnished, and hence it is difficult to achieve low absolute pressures in the channel. An application of the air-tight ' cocooning ' material—' liquid envelope '—was made, but proved unsuccessful; it reacted chemically with the paintwork of the shock tube. Finally, the shock tube was given three coats of high gloss paint in an endeavour to minimise the effects of the porosity of the wood. Considerable effort was also made to improve the diaphragm joint, where leaks were suspected. Many types of gasket (for example, neoprene, pure gum rubber and ' sorbo ' rubber) were tried without any alteration in the ultimate achievable vacuum; further, in some tests, the channel and chamber were bolted together, but little improvement was noted over the usual clamped joint.

9.1.1.3. *The Working-Section.*—This section, 2 ft in length, was not used during the calibration of the shock-tube installation, since lower absolute channel pressures were then obtainable. However, leakage problems encountered with this section are dealt with here for completeness. For preliminary testing, ordinary plate glass windows were fitted to the working-section; these were later replaced by specially selected optical quality plate-glass windows. The ' Bostik ' sealing compound, used to fix the glasses in their frames, was found to be slightly porous ; these leakages were eliminated by thin shellac-coated fillets of Plasticine round the edges of the frames (*see* Fig. 35). The ' door ' of this section was the source of numerous leaks, but layers of scotch tape were applied in positions indicated by the soapy water technique until these leaks were minimised. Further, a $\frac{1}{64}$ in. sheet rubber gasket was attached to the shock-tube working-section on the mating face of the door joint. In its final form, the inclusion of the working-section in the channel increased the residual vacuum from 24 to 55 mm of mercury.

9.1.1.4. *Gauge Calibration.*—Leak testing of all pipework, gauge connections and leads to the shock tube was carried out using standard methods; first, each item was checked individually and then as part of the complete installation. ' Apiezon ' grease, which had been found useful for additional sealing at the channel joints, was freely applied to all pipework and gauge joints ; however, this material tended to be gradually sucked away when the channel was highly evacuated and frequently a coating of shellac was necessary to ensure a reliable seal.

Fig. 54 gives the calibration charts for the chamber gauges, which were tested by comparing gauge readings and known hydrostatic pressures applied via an oil column from a standard test set. From Fig. 54 a special chart was drawn which directly converted chamber gauge readings in lb per sq in. to absolute pressures in millimetres of mercury, and since the residual channel pressure was also measured in millimetres of mercury, calculation of the pressure ratio P across the diaphragm was facilitated.

Channel pressures were to be measured by the gauge G_3, scaled 0–30 in. of mercury, and the McLeod-type gauge G_4, scaled 0–10 mm of mercury. As previously stated, the lowest absolute channel pressure attainable during the calibration tests was 24 mm of mercury and hence gauge G_4 was redundant. Further, the Bourdon-type gauge G_3 was very unreliable and hence a simple U-tube mercury manometer was constructed. This instrument was very satisfactory over the range required, although its accuracy naturally diminished at low absolute channel pressures (of the order of 25–100 mm of mercury).

A chart was also drawn for this gauge in the form of up-going limb-reading against down-going limb-reading, subsequently only the up-going limb-reading was taken and the other reading estimated from this chart. This calibration chart is not reproduced herewith, since it depends on the amount of mercury in the U-tube, and, if some mercury is accidentally spilt, the calibration must be repeated.

9.1.2. *Performance of Vacuum Pumps.*—The volume of the channel (less working-section) is 3·1 cu ft, and the evacuating performance of the only vacuum pump (Edwards type 1SP30) available was inadequate—*see* Test 4, Fig. 55. The evacuation of the channel to a pressure of 50 mm of mercury took 13 minutes, a prohibitive time to wait for each test. A water-jet vacuum pump (Edwards type C20) was employed as a booster but little improvement was noted. Finally a further pump (Edwards type 1S50) was. obtained on loan and the performance curves for this pump alone (Test 5) and both pumps (Test 7) are also given in Fig. 55. In the latter case, the channel was evacuated to 50 mm of mercury in 4 minutes. Note, in passing, that the channel of the Toronto shock tube (volume 1 cu ft) was evacuated to 1 mm of mercury in 1 minute by a Kinney type CVD vacuum pump. The respective pump displacements of free air in cubic feet per minute are given in Fig. 55 for comparison.

9.1.3. *Diaphragm Materials.*—The present writer has previously reported[22] the results of a large number of tests of different diaphragm materials, and, in common with other investigators,[4, 12] found that cellulose acetate sheet is the most useful diaphragm material for moderate pressure ratios. Fig. 56 gives the natural bursting pressures of cellulose acetate sheet of various thicknesses. These results were obtained from the 4 in. by $1\frac{3}{4}$ in. shock tube; and, although it is known[4] that the natural bursting pressure depends on the diaphragm size, that is, on the cross-section of the shock tube, little significant variation from the values given in Fig. 56 was noted when using the 6 in. by $2\frac{1}{2}$ in. shock tube.

9.1.4. *Calibration of the Electronic Equipment.*—9.1.4.1. *The Light Screens.*—When the light screens were set up and adjusted correctly (*see* next Section 9.2), their difference in ' response ' time to a given change of illumination was measured in the following way. A Mullard LSD–2 flash tube, equidistant from the two photomultiplier tubes, was fired and the time interval between the responses of the two light screens recorded by the chronometer in the usual manner. This test was repeated with the flash tube at several different equal distances from the photoelectric cells. Fig. 57 illustrates the experimental arrangement of these tests. It was found that, for every test made, the chronometer reading was always + 2 microseconds; that is, all chronometer readings of shock speed are 2 microseconds too high (*see* Section 9.3).

9.1.4.2. *The Time-Delay Equipment.*—Although this equipment was not used during the calibration tests, it is described here for convenience. Initially, the nominal 10,000 microsecond phantastron time-delay unit was set up for calibration as shown by Fig. 58a. A positive pulse from a dry battery was applied simultaneously to the unit and the ' start ' terminals of the

chronometer; the delayed pulse generated by the unit was fed to the chronometer 'stop' terminals. The maximum time-delay obtainable from this unit was found to be 1,000 micro-seconds instead of the rated 10,000 microseconds. Reference to equation (7.2), $T_{max} \simeq \frac{1}{2} R_g C_g$, and the values quoted in Table 2 of Ref. 32 (from which the circuit was constructed), namely, $R_g = 1\cdot1$ MΩ and $C_g = 2,000$ $\mu\mu$F, show that $T_{max} \simeq \frac{1}{2} \times 1\cdot1 \times 2,000 \simeq 1,100$ μsec. [Note also that the quoted delay times for the other phantastron circuits given in Table 2 of Ref. 32 are ten times too large.] Hence the values of R_g and C_g were adjusted to $R_g = 1\cdot2$ MΩ, $C_g = 20,000$ $\mu\mu$F, consistent with a nominal maximum time-delay for the circuit given in Fig. 45 of $\simeq 12,000$ μsec. A typical calibration curve for this circuit is given as curve A, Fig. 59; the abscissa notation R_1 and R_3 corresponds to the variable resistance $R_{10} = 20$ KΩ in Fig. 45, that is '$R_1 + R_3$' $= R_{10} = 20$ KΩ.

It was necessary to find what inherent delay existed in the circuit used for the production of timed photographs of the flow (see Chapter 7), and Fig. 58b illustrates how the equipment was set up for this purpose. As before, a pulse was simultaneously applied to both the chronometer and the time delay unit; the delayed output pulse caused the light source to fire. A photo-multiplier tube responded to this light output and so generated the 'stop' pulse for the chrono-meter. For any given setting of the delay unit, the reading obtained with the equipment set up as in Fig. 58b was always 8 microseconds larger than the delay of the unit alone (Fig. 58a). Hence all timed photographs must be labelled with a value 8 microseconds less than the chrono-meter reading.

Curve B of Fig. 59 is a typical calibration curve corresponding to the block diagram of the equipment shown in Fig. 58b. The arithmetic means of large numbers of chronometer readings of the time-delays corresponding to given settings of R_1 and R_3 show excellent linearity until overloading of the circuit occurs; that is, the voltages applied to the grids of the pentagrid valve V_1 of Fig. 45 fall outside their normal 'linear' working range.

Although the overall linearity is good, the reproduceability of the time-delay at a given setting of the unit is unsatisfactory. Scatter limits for each average result are given in Fig. 59, Curve B; these show that the actual delay at a given setting may vary by about ± 1 per cent from the value interpolated from a straight line drawn between the maximum and minimum delays available with no overloading of the unit. [Note that in Ref. 32, the scatter is claimed to be less than $\pm 0\cdot01$ per cent for a number of tests at a given setting.] This scatter led to the abandonment of the previously-constructed 500 microsecond phantastron unit (which had been intended for use in series with the 10,000 microsecond unit to provide precision delays in the range 0–1,000 microseconds—see Fig. 59), and the associated amplifier and cathode follower units.

During the development of this equipment it was noted that the calibration curve of the unit (such as curve B of Fig. 59), changed considerably with temperature and humidity variations and, particularly, when a valve was replaced. It appears that component tolerances are very critical, and also that many resistors suffer from hysteresis-type changes from their nominal values. To sum up, it was not found possible to calibrate the time delay units in an absolute manner; and, consequently, the chronometer must be retained as an integral part of the timing equipment to give a direct reading of the delay in any given test.

9.2. *Operational Procedure.*—A brief résumé of the sequence of operations during a calibration test is given below :—

(1) Switch on electronic equipment and wait until the 'warming-up' period has elapsed. Check the operation of the chronometer by using the manual push buttons. 'Tune' the light screens by adjusting each thyratron bias control until each photomultiplier tube will detect a very small change of illumination (such as that produced by passing a thin sheet of celluloid across the light beam).

(2) Fit diaphragm to shock tube and clamp chamber to channel. Switch on vacuum pumps, and allow the channel pressure to reach the desired value; then adjust the valves in the vacuum pump lines so that this value is maintained.

46

(3) Allow high-pressure air to enter the chamber until the pressure reaches the desired value.

(4) Wait about half a minute to allow the air in both the chamber and the channel to reach thermal equilibrium; that is, room temperature. Close all valves, including the gauge-panel shut-off valves, and rupture diaphragm immediately.

(5) Open the channel 'air-inlet' valve, record pressures exhibited by gauges and note barometric pressure.

When a timed photograph is taken of a test, the plate is exposed for a short time interval, including the instant when the diaphragm is ruptured. It may be noted that a few preliminary tests may be required each day to adjust the light screens to their necessary sensitivity; it was customary to produce a very weak shock (say $P \simeq 1 \cdot 25$) and adjust the thyratron bias or the sensitivity controls of the photomultiplier units until satisfactory operation occurred.

9.3. *Calibration Results.*—9.3.1. *Early Tests.*—Some hundred calibration runs were made whilst the erratic operation of the light screens (*see* Chapter 8) was being investigated; these results are not reproduced here, although certain results are no doubt of value. In addition, the chronometer became unreliable at this stage; correct operation was restored (by the replacement of several faulty valves) before the calibration proper commenced.

9.3.2. *Experimental Data.*—Three series of tests, designed to determine shock speeds and accelerations, were undertaken; these are detailed in Fig. 60, where the distances of each light screen from the diaphragm are given for each series of tests. In Series 1, 36-in. base, some 140 tests were made, whilst in Series 2 and 3, 18-in. base, approximately 40 tests were made in each series.

It will be appreciated that the actual pressure ratio across the diaphragm for each test may differ slightly from the required nominal test pressure ratio (say P_1). So that mean results could be calculated easily, the procedure illustrated in Fig. 61 was used to convert chronometer readings corresponding to pressure ratios slightly different from P_1 into 'corrected' chronometer readings corresponding to P_1. All the data obtained during the calibration of the shock tube are given in Tables 9, 10 and 11, and displayed in graphical form as Figs. 62 to 69 inclusive. In all cases, each plotted experimental point or entry in a table is the arithmetic mean of three or more 'corrected' chronometer readings. The maximum and minimum values assigned to the diaphragm pressure ratio P are in accordance with the accuracy of the observations (*see* next Section 9.3.3) and the plotted points indicate these 'error-limits'. The Series 1A and 1C results are compared in Fig. 64 in a preliminary attempt to investigate Reynolds number effects on shock speed; the chamber pressure was atmospheric in Series 1A whilst in Series 1C the channel pressure was atmospheric. A slight tendency may be noted for a slower shock wave to occur when the absolute channel pressure (and hence Re) is increased (*see* Chapter 10).

Comparison of the mean experimental curves of Series 1, 2 and 3 tests, that is, Figs. 65, 66 and 67 respectively, give for $P = 60$, chronometer readings of 1,310, 650 and 660 microseconds respectively; with similar results for other values of P.

It is clear that the shock wave must be decelerating as it passes down the shock tube (*see* Fig. 60) and, moreover, assuming the rate of attenuation to be constant along the tube, the theoretical velocity would appear to be reached some 8 ft from the diaphragm. This is in accordance with Fig. 20 and the results reported in Ref. 12. Figs. 68 and 69 show that the actual shock wave velocity at approximately 19 ft from the diaphragm is considerably less than the theoretical value for the corresponding diaphragm pressure ratio P. For example, at $P = 60$ and for an 18-in. base measurement Series 1, 2 and 3 results give chronometer readings of 655, 650 and 660 microseconds respectively, whilst the corresponding theoretical value is 610 microseconds, namely, shock speed attenuations of 7, 6 and 8 per cent respectively.

9.3.3. *Survey of Probable Errors in Experimental Data.*—9.3.3.1. *Errors Affecting P.*—The channel gauge, namely the U-tube manometer, can be read to less than $\pm\,0\cdot05$ in. or $\pm\,1\frac{1}{4}$ mm of mercury whilst barometric pressure is determinable to $\pm\,0\cdot25$ mm of mercury. Hence the columns headed 'channel pressure', p_0, of Tables 9, 10, and 11 are subject to approximately $\pm\,1$ mm of mercury error.

The main chamber pressure gauge G_2, scaled 0–120 lb per sq in., may be read to $\pm\,0\cdot25$ lb per sq in. or $\pm\,15$ mm of mercury, and the columns of chamber pressure $\bar{p}_0$ of the Tables are in error by this amount. Since the gauges were calibrated when atmospheric pressure was 763 mm of mercury, some correction should be applied for other atmospheric conditions; however, these variations were very small, involved an error of less than 1 per cent and were ignored.

Hence
$$P = \left(\frac{\bar{p}_0}{p_0}\right) \text{ may vary between} \frac{\bar{p}_0 + 15}{p_0 - 1} \text{ and} \frac{\bar{p}_0 - 15}{p_0 + 1}\,.$$

In this manner the columns of $P_{\max}$ and $P_{\min}$ given in Tables 9 to 11 were derived.

Taking the smallest values of $\bar{p}_0$ and p_0 recorded and allowing for the above errors we have

$$\frac{\delta P}{P} = \pm\,\sqrt{\left\{\left(\frac{\delta \bar{p}_0}{\bar{p}_0}\right)^2 + \left(\frac{\delta p_0}{p_0}\right)^2\right\}} = \sqrt{\left\{\left(\frac{15}{763}\right)^2 + \left(\frac{1}{59}\right)^2\right\}} = 0\cdot026\,,$$

that is, the pressure ratio across the diaphragm is determinable to $\pm\,3$ per cent.

9.3.3.2. *Errors Affecting the Chronometer Reading.*—We have already noted (*see* Section 9.1.4.1) that the readings of shock speed are in error; the chronometer reads 2 microseconds too high. For an 18-in. base, and $P \simeq 56\cdot0$, Table 11, this error is 2 in 657 or $0\cdot3$ per cent.; whilst for a 36-in. base and lower pressure ratios the error is of the order of $0\cdot1$ per cent.

It is possible that the counter chronometer does not count 'microseconds'; however, this is extremely unlikely since the oscillator is controlled by a 1 M/C crystal having a very close tolerance.

It is pertinent to note that we have discussed shock-speed variations over consecutive measuring distances along the shock tube and found discrepancies of the order of 5 microseconds in 600. The measuring apparatus is sufficiently accurate (to two parts in 600) that one can guarantee the genuine nature of the shock retardation. Finally, the individual tests, from which the average results shown in the tables were prepared, showed very little scatter about the mean value. Indeed, chronometer readings were repeated with almost uncanny regularity; typical scatter limits were 2426^{+2}_{-0}; 2031^{+1}_{-0}; 769^{+0}_{-2}.

PART C—AN INVESTIGATION OF THE EFFECTS OF BOUNDARY - LAYER GROWTH ON SHOCK TUBE FLOW

CHAPTER 10

Operation of a Shock-Tube Installation—Experimental Results

The development of the apparatus, and principally that of the electronic instrumentation, took considerable time; but a detailed calibration of the shock tube was ultimately carried out (*see* Chapter 9). In this present chapter, data are presented from experiments designed to cover various aspects of shock-tube flow and the flow-observation equipment; in particular, studies were made of Reynolds number effects on the flow, the use of various light sources for flow photography and the influence of the state of the boundary layer on shock-tube flow. Finally, timed photographs of the transient diffraction of a shock wave over a 10-deg wedge were obtained; this illustrated the main application of the shock tube, that is, the study of unsteady flows.

Further experimental work was curtailed by failure and 'burning-out' of the power unit which supplied the photomultiplier equipment.

10.1. *Influence of Reynolds Number on Shock Speed.*—Ref. 16 claims that the shock retardation does not depend on the absolute pressure p_0 in the channel over a range of p_0 from 14 to 45 mm of mercury at constant diaphragm pressure ratio P. It is the opinion of the present writer that these results are inconclusive, since the measured retardations are obtained by a planimeter from photographs of the flow. Duff[16] claims that these areas are '*nearly constant*', but it is likely that the small influence of Reynolds number on the flow has been masked by the experimental methods. Fig. 70 shows that as the channel pressure is increased, the shock velocity decreases. Twenty-four separate tests were made, and the individual results converted by the method of Fig. 61 so that all chronometer readings corresponded to a diaphragm pressure ratio $P = 6 \cdot 10$. The probable error margins of the observations are here expressed in terms of the chronometer readings instead of the more usual $P_{max} - P_{min}$ form; the average corrected chronometer readings are subject to an error of ± 3 microseconds at $P = 6 \cdot 10$. Theoretically, the shock speed corresponding to $P = 6 \cdot 10$ would give a chronometer reading of 1,838 microseconds; hence the shock retardation is 3 per cent at the lowest and 4 per cent at the highest Reynolds number obtained in these tests. It is clear that the influence of Reynolds number (and hence boundary-layer thickness) is not negligible in shock-tube flow.

10.2. *Flow Photography using Various Light Sources.*—Figs. 71 to 75 inclusive illustrate some features of the diffraction of a shock wave over a 10-deg wedge, and also give comparisons between the various light sources and optical techniques employed.

10.2.1. *Discussion of the Flow Photographs.*—A comparison between shadow photographs taken with FA–5, LSD–2 and spark sources appears as Fig. 71. Clearly the FA–5 source has too long a duration to be useful for this work, whilst the LSD–2 source is only slightly inferior to the spark source and both give relatively satisfactory results. Nevertheless, all the photographs reproduced herewith are of insufficient density and suffer from various other faults, some of which are described below.

In these experiments the 10-deg wedge model was clamped between the glass walls of the working-section using Plasticine as a filler. A little of this material protruded beyond parts of the wedge periphery but was not noticed until the photographs were developed; this explains the irregularities appearing on the surfaces of the wedge. Further, the aluminising of the mirror was faulty and caused several dark patches observable on the photographs; whilst 'orange-peel' effects, caused by felt polishing of the windows of the working-section, were also present. [Note that this unwanted effect may be eliminated by pitch polishing the glasses using jeweller's rouge.]

D

Schlieren photographs were taken using both LSD–2 and spark sources; however photographs taken with the latter possessed insufficient density to be of any value. The LSD–2 schlieren photographs, such as those appearing as Fig. 72, were very variable in quality and were satisfactory only when the arc discharge did not wander round the glass envelope of the flash tube. Typical spark shadowgraphs of the flow over the 10-deg wedge are given in Fig. 73, with an enlargement of one photograph appearing as Fig. 74. Finally, Fig. 75 is a shadowgraph using the LSD–2 source and shows particles of the shattered diaphragm passing the wedge some time after the shock has passed.

Many experimental studies of the transient diffraction of a shock wave round a wedge have been made in shock tubes, and a theoretical solution of the problem has been given by Chester[39]. In the present experiments, the inclined surfaces of the wedge were at + 11 deg and − 1 deg to the flow direction and Mach reflection of the primary shock from the wedge surface inclined at + 11 deg is visible in Figs. 72 and 73. On the opposite side of the wedge, the shock has been diffracted round an angle of 1 deg and hence is no longer plane; further distortion occurs as the two 'halves' of the primary shock diffract round the base of the wedge. (Fig. 73b to 73d.) Vortices are shed from the base of the wedge, giving visible indication that aerodynamic lift is being generated; further, the flow appears to separate from the leading-edge of the wedge surface inclined at − 1 deg to the free-stream direction (Figs. 72f and 73). The successive reflections of the diffracted shock waves from the walls of the shock tube are visible in Fig. 74.

10.2.2. *Suggested Improvements in the Optical Techniques.*—In recent months new photographic plates, Ilford Special Type LN, have superseded Ilford Zenith plates as the standard plate for shadow/schlieren photography at the N.P.L. These new plates are nearly ten times as fast as the Zenith variety and, consequently, no difficulties are encountered due to insufficiently dense photographic images. Further increases of photographic density, by improved aluminising of the main concave mirror, removal of the 'orange-peel' effect from the working-section windows and the use of an improved optical layout without the plane mirrors shown in Fig. 49, would probably not be so critical now as they appeared when the experiments were made. Shorter spark and FA–5 flash tube light durations (and hence sharper photographs) may be obtained by reducing the energy dissipated in the discharge to 1 → 2 joules; and, in the spark discharge case, by increasing the operating voltage of the spark-gap to about 20 kilovolts.

In general, a balance must be made between the opposing criteria of sharpness and photographic density; in the present experiments, the density of the plates was so low that any further reduction of discharge energy was impossible. Unquestionably, the advent of the 'LN' photographic plates will improve the general standard of shadow/schlieren flow observations.

10.3. *Determination of the State of the Boundary Layer.*—Since we have established that the velocity of the shock wave down a shock tube decreases as the Reynolds number increases, we must determine the appropriate conditions for the occurrence of laminar or turbulent boundary layers. The direct-shadow method of flow photography can be used[40] to determine whether a two-dimensional boundary-layer flow is laminar or turbulent and to indicate the position where transition from laminar to turbulent flow takes place. This method is comprehensively described in Ref. 41; here, it is sufficient to note that a laminar boundary layer produces a characteristic white line running parallel to, but separated from, the surface under observation. Close to the transition point, this white line bends towards the surface since a turbulent boundary layer produces a white line which effectively touches the surface. [Geometric ray diagrams and photographs explaining these phenomena appear as Figs. 5 and 6 of Ref. 41.] The spark shadowgraphs of Fig. 73 were taken by removing the slit S from the single-mirror optical system described earlier (Fig. 49). It was not realised at the time that only a *direct* shadowgraph (that is, the photographic plate is placed directly behind the working-section) will give these characteristic white lines and hence determine the state of the boundary layer. The reasons for this unexpected anomaly are shown in Fig. 76.

50

Let X and Y be the conjugate focal planes of the camera lens L_c and let the light rays passing through the boundary layer be deflected so that a white line is produced in the X-plane; this is the correct plane for direct-shadow photography. Fig. 76 shows that some of the deflected rays will miss the camera lens (unless its diameter is very large) and hence not be recorded by a photographic plate placed in the Y-plane (as in Fig. 49). However, this is probably not the main reason for the non-appearance of the white line on photographs taken in plane Y. In practice, the camera lens L_c cannot possibly have discrete focal planes at X and Y; there must exist focal *regions*, albeit of small extent. Hence the camera screen placed in the Y-plane will show part of the image of the white line in the X-plane and *also* the superimposed distorted images from other ' focal ' planes x_1, x_2, x_3, etc. It is unlikely that any clear flow picture will result, and the state of the boundary layer will not be determinable from this type of shadowgraph—*see* Figs. 73 to 75.

Suggestions for Further Experimental Work.—A comprehensive programme of tests designed to evaluate Reynolds number effects on all aspects of shock-tube flow is required. Methods have been suggested above whereby the existing optical equipment may be modified to give flow photographs of consistent quality, in particular, adequate density and sharpness. The direct-shadow photographic method, utilising a spark source, should prove valuable for studies of boundary layer effects on shock-tube flow.

CHAPTER 11

A Preliminary Theoretical Investigation of the Effects of Boundary-Layer Growth on Shock-Tube Flow

11.1. *Introduction.*—Previous theoretical work[12, 21] on the effects of boundary-layer growth on shock-tube flow has been confined to the Rayleigh type of analysis which postulates a uniformly growing boundary layer over an infinite tube length, whereas real shock-tube flow involves a non-uniformly growing boundary layer over a finite length of the tube. It is not surprising that these theories do not give an accurate picture of the real flow pattern in a shock tube, and an adequate theory should consider the contact surface acceleration and the shock-wave retardation simultaneously and, further, include the dependence of the shock attenuation on as many parameters as possible of those discussed in Chapter 5, namely :—

the shock strength p_s

the Reynolds number of the flow Re

the size and roughness of the tube cross-section

and the elapsed time since the motion was started $t \left(= \dfrac{X_s}{V_+} \right)$.

A simple theory has been developed which provides evidence that the acceleration of the contact surface is a necessary consequence of the growth of boundary layers on the tube walls and that the subsequent changes in the flow pattern may be related to a shock retardation. This theory is based on the conventional semi-infinite-wall, steady-flow, boundary-layer theory applied to cases where the velocity of the wall is not equal to zero. In the present chapter, the analysis will be restricted to the simplest case ; namely that for which the tube wall boundary layers are assumed to be LAMINAR and INCOMPRESSIBLE.

Initially we must justify the use of the von Kármán momentum integral equation for the transformed shock-tube problem where the velocity of the wall is not equal to zero.

The full boundary-layer equations for unsteady flows are

$$\frac{\partial u}{\partial t} + u \frac{\partial u}{\partial x} + v \frac{\partial u}{\partial y} = \frac{\partial \bar{u}}{\partial t} + \bar{u} \frac{\partial \bar{u}}{\partial x} + \nu \frac{\partial^2 u}{\partial y^2} \quad \cdots \qquad \cdots \qquad \cdots \qquad \cdots \qquad (11.1)$$

and

$$\frac{\partial u}{\partial x} + \frac{\partial v}{\partial y} = 0 \quad \cdots \qquad \cdots \qquad \cdots \qquad \cdots \qquad \cdots \qquad \cdots \qquad (11.2)$$

where $\bar{u}$ is the free-stream velocity, and u and v are the boundary-layer velocities along the x and y axes respectively. From (11.1) we have

$$\frac{\partial u}{\partial t} - \frac{\partial \bar{u}}{\partial t} - \left\{ u \frac{\partial}{\partial x}(\bar{u} - u) + v \frac{\partial}{\partial y}(\bar{u} - u) \right\} - (\bar{u} - u)\frac{\partial \bar{u}}{\partial x} = \nu \frac{\partial^2 u}{\partial y^2} \quad \cdots \qquad \cdots \qquad (11.3)$$

where we have introduced the quantity $\frac{\partial \bar{u}}{\partial y}$ which is zero by definition.

Then, using (11.2), (11.3) becomes

$$\frac{\partial u}{\partial t} - \frac{\partial \bar{u}}{\partial t} - \left\{ \frac{\partial}{\partial x}[u(\bar{u} - u)] + \frac{\partial}{\partial y}[v(\bar{u} - u)] \right\} - (\bar{u} - u)\frac{\partial \bar{u}}{\partial x} = \nu \frac{\partial^2 u}{\partial y^2}. \quad \cdots \qquad \cdots \qquad (11.4)$$

Integrate (11.4) across the boundary layer from $y = 0$ to $y = \delta$, where δ is the boundary-layer thickness.

Then

$$\int_0^\delta \frac{\partial u}{\partial t}\, dy - \int_0^\delta \frac{\partial \bar{u}}{\partial t}\, dy - \frac{\partial}{\partial x}\int_0^\delta u(\bar{u} - u)\, dy - \frac{\partial \bar{u}}{\partial x}\int_0^\delta (\bar{u} - u)\, dy = -\nu\left(\frac{\partial u}{\partial y}\right)_0. \qquad \cdots \qquad (11.5)$$

Note that although we put $v = 0$ at $y = 0$ and $(\bar{u} - u) = 0$ at $y = \delta$ to obtain (11.5), we do *not* postulate that $u = 0$ at $y = 0$ or $v = 0$ at $y = \delta$.

Fig. 77 illustrates how we transform the moving-shock problem of the shock tube to an equivalent stationary shock problem. The following analysis depends on the assumption that at a given distance behind the shock wave the boundary layer will always have the same thickness. Thus, consider the two instantaneous pictures of shock-tube flow shown in Fig. 78; we assume that at a given distance ξ from the shock (defined by $\xi = 0$) the boundary-layer thickness is δ_ξ.

Later, in an exactly analogous treatment of the rarefaction wave in a shock tube, we assume that at a given distance ζ from the rarefaction wave (assumed to be infinitely thin and defined by $\zeta = 0$) the boundary-layer thickness is δ_ζ.

Hence we may put $\frac{\partial u}{\partial t} = 0$ in equation (11.5). For the shock-tube problem, equation (11.5) further simplifies since $\frac{\partial \bar{u}}{\partial t} = 0$ and $\frac{\partial \bar{u}}{\partial x} = 0$.

Thus (11.5) becomes

$$\bar{u}^2 \frac{d\theta}{dx} = \nu\left(\frac{\partial u}{\partial y}\right)_0 \quad \cdots \qquad \cdots \qquad \cdots \qquad \cdots \qquad \cdots \qquad \cdots \qquad (11.6)$$

where θ, the momentum thickness of the boundary layer, is defined by

$$\theta = \int_0^\delta \frac{u}{\bar{u}}\left(1 - \frac{u}{\bar{u}}\right) dy . \qquad \cdots \qquad \cdots \qquad \cdots \qquad \cdots \qquad (11.7)$$

The displacement thickness of the boundary layer, δ^*, is defined by

$$\delta^* = \int_0^\delta \left(1 - \frac{u}{\bar{u}}\right) dy . \qquad \cdots \qquad \cdots \qquad \cdots \qquad \cdots \qquad (11.8)$$

52

The subsequent analysis yields two expressions for the boundary-layer thickness at the contact surface, one derived from consideration of the flow region between the shock and the contact surface and the other derived in a similar way from the region between the contact surface and the 'linearized' rarefaction wave.

11.2. Consideration of the Flow Region Between the Shock and the Contact Surface (Fig. 77).—

If we refer to the transformed shock-tube problem shown in Fig. 77b, we must consider the growth of a boundary layer to the left of the shock (defined by $\xi = 0$), when the wall is travelling with a non-dimensional velocity V_+ and the fluid with a non-dimensional velocity $v_- = V_+ - v_+$. Let any non-dimensional velocity in the boundary layer be $\dfrac{u}{a_0}$ and call $v_- = \dfrac{\bar{u}}{a_0}$ for convenience; then we assume (as usual) that the velocity profile of the boundary layer may be defined in terms of a one-parameter family. Hence $\dfrac{u}{\bar{u}} = f(\eta) = f\left(\dfrac{y}{\delta}\right)$ where $\eta = \dfrac{y}{\delta}$, and δ is the boundary-layer thickness (see Fig. 77c).

Suppose we express the velocity distribution in the boundary layer as a polynomial in η, then

$$\frac{u}{\bar{u}} = a + b\eta + c\eta^2 + d\eta^3 + e\eta^4 + \ldots \qquad \qquad \qquad (11.9)$$

The relevant boundary conditions are

(1) $y = 0$, $\quad \eta = 0 \quad u = a_0 V_+$

(2) $y = 0$, $\quad \eta = 0 \quad \dfrac{\partial^2 u}{\partial y^2} = 0$ since $\dfrac{\partial u}{\partial x} = 0$

$\qquad\qquad\qquad$ (cf. equation (11.1) in which $\dfrac{\partial u}{\partial x} = 0$ at $y = 0$ since the wall has a constant velocity V_+.)

(3) $y = \delta$, $\quad \eta = 1 \quad \dfrac{u}{a_0} = \dfrac{\bar{u}}{a_0} \quad$ .. .. (11.10)

(4) $y = \delta$, $\quad \eta = 1 \quad \dfrac{\partial u}{\partial y} = 0$

(5) $y = \delta$, $\quad \eta = 1 \quad \dfrac{\partial^2 u}{\partial y^2} = 0$.

Now, by definition, the momentum thickness θ is given by

$$\theta = \delta \int_0^1 \frac{u}{\bar{u}}\left(1 - \frac{u}{\bar{u}}\right) d\eta . \qquad \qquad \qquad \qquad (11.11)$$

Using (11.9) and (11.10) we get

$$\frac{u}{\bar{u}} = 1 - e(1 - 2\eta + 2\eta^3 - \eta^4) \qquad \qquad \qquad \qquad (11.12)$$

where $\qquad\qquad e = \tfrac{1}{2}b = -\tfrac{1}{2}d = -c = 1 - a = 1 - \dfrac{a_0 V_+}{\bar{u}}$

or $\qquad\qquad e = 1 - \dfrac{V_+}{v_-} = -\dfrac{1}{\dfrac{V_+}{v_+} - 1} \cdot \ldots \qquad .. \qquad .. \qquad .. (11.13)$

Hence for a given shock strength e is known.

53

Inserting equation (11.12) in (11.11) and evaluating we get

(5-term series) $\quad .. \quad \theta = \left(\dfrac{3}{10}e - \dfrac{23}{126}e^2\right)\delta \,.$ $\qquad .. \qquad .. \qquad .. \qquad .. \qquad ..$ (11.14)

If the above procedure is repeated using only 4 or 3 terms of equation (11.9) and the appropriate number of boundary conditions we obtain

(4-term series) $\quad .. \quad \theta = \left(\dfrac{3}{8}e - \dfrac{33}{140}e^2\right)\delta$ $\quad .. \qquad .. \qquad .. \qquad .. \qquad .. \qquad ..$ (11.15)

and

(3-term series) $\quad .. \quad \theta = \left(\dfrac{1}{3}e - \dfrac{1}{5}e^2\right)\delta$ $\qquad .. \qquad .. \qquad .. \qquad .. \qquad .. \qquad ..$ (11.16)

In a similar way, by inserting (11.12) into (11.8) we get

(5-term series) $\quad .. \quad \delta^* = \dfrac{3}{10}e\delta \,,$ $\quad .. \qquad .. \qquad .. \qquad .. \qquad .. \qquad .. \qquad ..$ (11.17)

and for the other cases

(4-term series) $\quad .. \quad \delta^* = \dfrac{3}{8}e\delta$ $\qquad .. \qquad .. \qquad .. \qquad .. \qquad .. \qquad .. \qquad ..$ (11.18)

(3-term series) $\quad .. \quad \delta^* = \dfrac{1}{3}e\delta \,.$ $\qquad .. \qquad .. \qquad .. \qquad .. \qquad .. \qquad .. \qquad ..$ (11.19)

We must evaluate the boundary-layer thickness at the contact surface, taking the value of θ defined by equation (11.14).

Now, from equation (11.6)

$$\left(\frac{\partial u}{\partial y}\right)_{y=0} = \frac{\bar{u}^2}{\nu}\frac{d\theta}{d\xi} \qquad .. \qquad .. \qquad .. \qquad .. \qquad .. \qquad .. \qquad .. \quad (11.20)$$

and from (11.9)

$$\left(\frac{\partial u}{\partial y}\right)_{y=0} = 2e\frac{\bar{u}}{\delta}\,. \qquad .. \qquad .. \qquad .. \qquad .. \qquad .. \qquad .. \qquad .. \quad (11.21)$$

Combining (11.14), (11.20) and (11.21) we have

$$\left(\frac{3}{10}e - \frac{23}{126}e^2\right)\frac{d\delta}{d\xi} = \frac{2}{\delta}\cdot e\frac{\nu}{\bar{u}}$$

or

$$\delta\,d\delta = \frac{2\nu}{\bar{u}}\frac{d\xi}{\left(\dfrac{3}{10} - \dfrac{23}{126}e\right)}\,.$$

On integration this becomes

$$\frac{\delta^2}{2} = \frac{2\nu\xi}{\bar{u}}\frac{1}{\left(\dfrac{3}{10} - \dfrac{23}{126}e\right)} + \text{constant}.$$

Now $\delta = 0$ when $\xi = 0$ and hence the 'constant' $= 0$.

Finally

$$\delta = f\sqrt{\frac{\nu\xi}{\bar{u}}} \text{ where } f = \sqrt{\left\{\frac{4}{\left(\dfrac{3}{10} - \dfrac{23}{126}e\right)}\right\}}\,. \qquad .. \qquad .. \quad (11.22)$$

We elect to call δ the boundary-layer thickness *at the contact surface position*, $\xi_{cs} \equiv \xi$.

Again with reference to Fig. 77d, consider the case when the shock is in the working-section at X_s, and the contact surface is a distance $X_s - X_{cs}$, that is $\xi_{cs} \equiv \xi$ behind the shock.

Clearly
$$\frac{X_s}{V_+} = \frac{X_{cs}}{v_+} \quad \text{i.e.,} \quad \xi = \left(1 - \frac{v_+}{V_+}\right) X_s \, .. \qquad .. \qquad .. \qquad .. \quad (11.23)$$

and further
$$\frac{\bar{u}}{a_0} = v_- = V_+ - v_+ \, . \qquad .. \qquad .. \qquad .. \qquad .. \qquad .. \quad (11.24)$$

Substituting in (11.22) for ξ, $\bar{u}$ and e from (11.23), (11.24) and (11.13) respectively, we have

$$\delta^2 = \frac{40\nu}{3V_+ a_0} \cdot X_s \cdot \frac{\left\{1 - \dfrac{v_+}{V_+}\right\}}{\left\{1 - \dfrac{74}{189}\dfrac{v_+}{V_+}\right\}} \cdot \qquad .. \qquad .. \qquad .. \qquad .. \quad (11.25)$$

If we refer all quantities to the reference state ahead of the moving shock and also assume

$$\frac{\mu}{\mu_0} = \left(\frac{T}{T_0}\right)^{3/4}$$

we obtain then

$$\delta^2 = \frac{40}{3} \cdot \frac{\mu_0}{\rho_0 a_0} \cdot \frac{X_s}{V_+} \left(\frac{T}{T_0}\right)^{3/4} \left(\frac{\rho_0}{\rho}\right) \frac{\left\{1 - \dfrac{v_+}{V_+}\right\}}{\left\{1 - \dfrac{74}{189}\dfrac{v_+}{V_+}\right\}} \cdot \qquad .. \qquad .. \quad (11.26)$$

Hence δ^2 is a function of $\dfrac{1}{Re}$; $\dfrac{1}{t}$ and p_s, $\left\{t = \dfrac{V_+}{X_s}\right\}$, that is, Reynolds number, shock strength and time. Note that $\delta \propto \dfrac{1}{t^{1/2}}$ agrees with the well-known result for motions which have just started from rest[42]. With the working-section at a distance X_s from the diaphragm, and given $\mu_0 \rho_0$ and a_0 ahead of the shock, we may calculate the thickness of the boundary layer at the contact surface position when the shock is in the working-section. As $V_+ \to 1 \cdot 0$ (11.26) shows δ is not equal to zero. In fact, this corresponds to a sound wave propagating down a tube, leaving the fluid at rest behind it. Then, in the transformed picture, the walls and the fluid both move at speed a_0. Hence as $v_+ \to 0$, $v_- \to 1$, $V_+ \to 1$, δ^* and θ both vanish, but δ has a finite, non-zero value; that is, within the boundary layer the velocity is constant and equal to the free-stream value v_-.

We have evaluated θ, δ^* and δ at the contact surface and particular attention is drawn to the *sign* if δ^*, the displacement thickness. Now $\delta^* = \dfrac{3}{10} e\delta$ where $e = -\dfrac{1}{\left(\dfrac{V_+}{v_+} - 1\right)}$, and since

$\dfrac{u}{U} \equiv \dfrac{v_+}{V_+}$ is a function of V_+, the shock speed, and is tabulated (Table 3, column 2), a curve of e against V_+ may be drawn. This curve is labelled A in Fig. 79. Since e is always *negative*, δ^* must be negative, implying that the flow $v_- = \dfrac{\bar{u}}{a_0} = (V_+ - v_+)$ will decrease in velocity as we move to the left of Fig. 77b. Resuperposing the velocity to the right V_+ means that the velocity v_+ will increase; that is, *the contact surface will accelerate*. In a similar manner, the momentum thickness θ must be negative, since $\theta = \left(\dfrac{3}{10} e - \dfrac{23}{126} e^2\right) \delta$. This is added confirmation that the contact surface must accelerate as a direct consequence of the formation of the shock-tube boundary layers. Next, we bring the rarefaction wave to rest in a similar manner and again calculate the boundary-layer parameters at the contact surface.

11.3. *Simplified Consideration of the Flow Region between the Contact Surface and the Head of the Rarefaction Wave.*—In the following simplified theory, we assume that the rarefaction wave has zero thickness, an assumption which is valid for weak shock-wave conditions in the shock tube. Fig. 80 shows the transformation from the unsteady shock-tube problem to the equivalent stationary rarefaction wave problem. The calculation of δ^*, θ and δ at the contact surface is performed using the boundary-layer theory derived previously.

In this case, the wall is moving with velocity $\bar{a}_0$ and the free stream with velocity $\bar{u} + \bar{a}_0$, or, using the non-dimensional approach as in Section 11.2, velocities of unity and $(v_+ + 1)$ respectively. This follows since $\bar{a}_0 = a_0$ and $\bar{u} = u$ by the standard shock-tube assumptions—*see* Chapter 3.

Equations (11.9) and (11.10) hold for this solution but the boundary conditions (1) and (3) of equation (11.10) become

(1) $y = 0$; $\eta = 0$ $\dfrac{u}{a_0} = \dfrac{\bar{a}_0}{a_0} = 1$

(3) $y = \delta$; $\eta = 1$ $\dfrac{u}{a_0} = \dfrac{\bar{u}'}{a_0} = (v_+ + 1)$.   .. .. (11.27)

As before, we obtain

$$\frac{u}{\bar{u}'} = 1 - e'(1 - 2\eta + 2\eta^3 - \eta^4) \qquad .. \qquad .. \qquad .. \qquad .. \quad (11.28)$$

where

$$e' = 1 - \frac{a_0}{\bar{u}'} = \left(\frac{v_+}{v_+ + 1}\right). \qquad .. \qquad .. \qquad .. \qquad .. \quad (11.29)$$

Table 1, column 4, gives values of v_+ for a range of shock speeds V_+, and enables a curve of e' against V_+ to be drawn.   (Curve B of Fig. 79.)

Now $\delta^* = \dfrac{3}{10}e'\delta$ and $\theta = \left(\dfrac{3}{10}e' - \dfrac{23}{126}e'^2\right)\delta$ as before, but e' is always *positive*, hence δ^* and θ are always positive. This implies that the flow $(v_+ + 1)$ will increase in velocity as we move to the right of Fig. 80b. If we now revert to the shock-tube problem, clearly the velocity v_+ must increase and hence *the contact surface will accelerate*. In an analogous manner to the derivation of equation (11.22) we may deduce the boundary-layer thickness at the contact surface. Let $\zeta = 0$ define the position of the 'linearized' rarefaction wave (Fig. 80b) and note that if $\zeta = 0$, $\delta = 0$. Then we have

$$\delta = \sqrt{\left\{\frac{4}{\left(\frac{3}{10} - \frac{23}{126}e'\right)}\right\}}\sqrt{\left(\frac{\bar{v}\zeta}{\bar{u}'}\right)} \qquad .. \qquad .. \qquad .. \qquad .. \quad (11.30)$$

where $\bar{v}$ is the kinematic viscosity corresponding to the flow region between the contact surface and the rarefaction wave.

Let δ be the boundary-layer thickness at the contact surface, defined by $\zeta = \zeta_{cs}$. We require an expression for ζ in terms of the known velocities of the contact surface and rarefaction wave and the position of the shock at any given instant. If we refer to Fig. 80d, and note that X_R is a negative quantity we have

$$\frac{|X_R|}{1} = \frac{X_s}{V_+} = \frac{X_{cs}}{v_+}$$

and hence

$$X_{cs} + |X_R| = \frac{(v_+ + 1)}{V_+} \cdot X_s = \zeta = \zeta_{cs}. \qquad .. \qquad .. \qquad .. \qquad .. \quad (11.31)$$

56

Now substitute in (11.30) for e', $\bar{u}'$ and ζ using equations (11.29), (11.27) and (11.31) respectively. We obtain

$$\delta^2 = \frac{40}{3} \frac{\bar{\nu}}{a_0} \cdot \frac{X_s}{V_+} \frac{\{1 + v_+\}}{\left(1 + \dfrac{74}{189} v_+\right)} \cdot \qquad \qquad \qquad \qquad \text{(11.32)}$$

Now $\bar{\nu} = \dfrac{\bar{\mu}}{\bar{\rho}}$ and we assume $\dfrac{\bar{\mu}}{\bar{\mu}_0} = \left(\dfrac{\bar{T}}{T_0}\right)^{3/4}$ as before.

Then $\qquad\qquad \bar{\nu} = \left(\dfrac{T}{T_0}\right)^{3/4}\left(\dfrac{\bar{T}}{T}\right)^{3/4} \dfrac{\mu_0}{\rho_0} \cdot \dfrac{\rho_0}{\rho} \cdot \dfrac{\rho}{\bar{\rho}} \cdot$

Finally, for the contact surface $\dfrac{\rho}{\bar{\rho}} = \dfrac{\bar{T}}{T}$ and hence

$$\bar{\nu} = \left(\frac{T}{T_0}\right)^{3/4}\frac{\mu_0}{\rho_0} \cdot \frac{\rho_0}{\rho} \cdot \left(\frac{\bar{T}}{T}\right)^{7/4} = \nu \cdot \left(\frac{\bar{T}}{T}\right)^{7/4} \cdot \qquad \qquad \qquad \text{(11.33)}$$

Substitute in (11.32) for $\bar{\nu}$ and consider the two expressions (11.26) and (11.32) for the boundary-layer thickness, δ, at the contact surface. We get

<p align="center">From Shock Solution $\delta_{\xi cs}$</p>

$$\frac{40}{3} \frac{\mu_0}{\rho_0 a_0} \cdot \frac{X_s}{V_+} \cdot \left(\frac{T}{T_0}\right)^{3/4} \left(\frac{\rho_0}{\rho}\right) \left\{ \frac{1 - \dfrac{v_+}{V_+}}{1 - \dfrac{74}{189}\dfrac{v_+}{V_+}} \right\}$$

<p align="center">From Rarefaction Solution $\delta_{\zeta cs}$</p>

$$\frac{40}{3} \frac{\mu_0}{\rho_0 a_0} \cdot \frac{X_s}{V_+} \cdot \left(\frac{T}{T_0}\right)^{3/4} \left(\frac{\rho_0}{\rho}\right) \left\{ \frac{1 + v_+}{1 + \dfrac{74}{189} v_+} \left(\frac{\bar{T}}{T}\right)^{7/4} \right\} \cdot$$

Hence :—

$$\frac{\delta_{\xi cs}}{\delta_{\zeta cs}} = \frac{\left(1 - \dfrac{v_+}{V_+}\right)}{\left(1 - \dfrac{74}{189}\dfrac{v_+}{V_+}\right)} \Bigg/ \left\{ \frac{(1 + v_+)}{\left(1 + \dfrac{74}{189} v_+\right)} \times \left(\frac{\bar{T}}{T}\right)^{7/4} \right\} \cdot \qquad \qquad \text{(11.34)}$$

Tabulated values of $\dfrac{v_+}{V_+}$; v_+ and $\dfrac{\bar{T}}{T}$ are available for given values of the shock speed V_+, and a graph of δ_ξ plotted against δ_ζ is given in Fig. 81. Specimen calculations are given in the following Table.

V_+	From shock solution δ_ξ	From R. W. solution δ_ζ
1·0	1·0	1·0
1·1	0·89	0·88
1·25	0·78	0·73
1·5	0·64	0·50
2·0	0·48	0·23
3·0	0·35	0·04
4·0	0·30	0·006

It is seen that the two solutions are compatible for weak shock waves.

<p align="center">57</p>

We can now draw the profile of the boundary layer along the tube at any given instant, under the simplified conditions specified by Fig. 82. For a given shock velocity, the functions e, e', $\bar{u}$ and $\bar{u}'$ are known and ν and $\bar{\nu}$ (which depend on the absolute density and the shock strength) are calculable. Then, between the shock and the contact surface δ_ξ is proportional to $\sqrt{\xi}$ and between the contact surface and the 'line' rarefaction wave δ_ζ is proportional to $\sqrt{\zeta}$; that is, the solution shows that the boundary layers on the walls of a shock tube grow in a parabolic manner.

11.4. *General Discussion of the Problem.*—11.4.1. *The Significance of Equation* (11.34).—In the preceding sections we have made the very reasonable assumption that the boundary-layer thicknesses at given distances from the shock and the rarefaction wave remain constant as the shock and the rarefaction wave move further apart (*see* Fig. 78). Equation (11.34) shows that such an assumption leads to plausible results when the shock wave is weak.

Since discontinuous derivatives of the flow variables exist at the contact surface it is improbable that the initial assumption would be accurate in the neighbourhood of the contact surface, and, further, in the early stages of the flow when the shock, contact surface and rarefaction wave are very close together, discontinuities of velocity gradient might give rise to serious errors. The velocity gradients due to the growth of the boundary layers on the walls of the shock tube may be ignored in a 'first-order' theory.

11.4.2. *The Effects of a Rarefaction Wave of Finite Thickness.*—If we consider the head of the rarefaction wave to be brought to rest, the tail of the wave will more with a known velocity away from the head, and the linear free-stream velocity gradient will become less steep as the extent of the rarefaction wave region increases. Since the distance from the head to the tail of the rarefaction wave is known for a shock wave of a given strength and at any given time, we would like to compute the boundary-layer thickness at the tail of the rarefaction wave and then match this solution with that given in section 11.3 and hence calculate the boundary-layer thicknesses at the contact surface.

Unfortunately, this is not possible by the methods employed previously, since within the rarefaction wave region it cannot be assumed that the boundary-layer thickness is only a function of the distance from the head of the wave.

Fig. 83 illustrates qualitatively the influence of the finite rarefaction wave on the boundary-layer thickness δ_ζ. The favourable velocity gradient through the rarefaction wave will cause a less rapid growth of the boundary layer and hence a larger discrepancy between the two values of the boundary-layer thickness at the contact surface, that is $\delta_\zeta \ll \delta_\xi$. However, it is relevant to note that the effects of heat transfer (which will be considerable for the strong shock-wave case) are such that δ_ζ is increased and δ_ξ is decreased, and hence the boundary-layer thicknesses at the contact surface may be approximately the same, even in the strong shock case. Furthermore, the ideal contact surface will diffuse into a contact region by turbulent mixing and heat conduction and hence it is plausible to assume that no severe discontinuities occur at the contact surface; consequently, the type of analysis developed in Sections 11.2 and 11.3 would be applicable to the strong shock case if a solution for the finite rarefaction wave region could be found, and the effects of compressibility and heat transfer were taken into account.

11.4.3. *Correlation of Shock Velocity and Contact Surface Velocity.*—In the above analysis we have shown that, relative to a stationary shock wave, the contact surface will accelerate due to the formation of boundary layers on the walls of the shock tube. To confirm experimental results, it is necessary to show that this acceleration of the contact surface implies a deceleration of the shock wave; indeed, one might intuitively expect that the departures from the inviscid solution would be averaged out between the shock and the contact surface, so that if the latter moves faster, the former must move slower. It would be instructive if such a result could be demonstrated by a simple analysis, and several attempts were made using crude assumptions in place of the exact energy equation of the flow. For example, we might assume that the rate of generation of kinetic energy is a constant or a decreasing function of time.

All these assumptions lead to analyses which show that an accelerating contact surface implies a decelerating shock wave; in particular, the assumption that the rate of generation of kinetic energy is a constant leads to the conclusion that the percentage deceleration of the shock wave is twice the percentage acceleration of the contact surface. These analyses are not reproduced herewith since the assumptions on which they are based are highly speculative; nevertheless, the results so obtained lead the present writer to hope that a more refined analysis would also agree with the observed motions of the shock wave and the contact surface.

In the opinion of the present writer, the heat transfer from the hot gas behind the shock to the walls of the shock tube is the premier cause of shock attenuation and until ' viscous ' solutions for shock-tube flow incorporate the effects of heat transfer, it is likely that theoretical results for the attenuation will show serious quantitative disagreement with observed values.

CHAPTER 12

Conclusions

12.1. *Review of Work done at Bristol* 1952–1954.—A survey of existing shock-tube theory and experimental results has been conducted; particular emphasis was placed on the features of actual shock-tube flow which diverged from ideal non-viscous theory. A basic ideal shock-tube theory has been formulated in detail, using those parameters which have greatest practical significance, and subsequently, performance charts affording a rapid method for the aerodynamic design of shock tubes using air as the working fluid have been developed. These charts appear as Figs. 13 to 18 inclusive.

Experimental results diverge from the simple ideal theory mentioned above, principally because viscous effects are present in actual shock tube flow. Careful analysis of available experimental data yielded a series of important parameters which influence the actual flow; in particular it was noted that the shock attenuation INCREASES with INCREASE of

(1) $\dfrac{X_s}{H}$; the ratio $\dfrac{\text{length of tube traversed by shock}}{\text{hydraulic radius of tube}}$,

(2) V_+ ; the shock speed,

(3) $[Re]$; the Reynolds number of the test,

(4) $\dfrac{vt}{A} = \dfrac{vX_s}{AV_+}$; a parameter introduced in Ref. 21, and

(5) ———— ; tube roughness.

A new analytical approach led to the development of a theory of shock-tube flow which included the effects of boundary-layer growth on the walls of the shock tube and explained several features of the actual flow patterns which are at variance with ideal non-viscous theory. As a direct consequence of the boundary-layer growth, the contact surface was found to accelerate and this may be shown to be accompanied by a retardation of the shock wave. Moreover, the acceleration of the contact surface—which is related to the boundary-layer thickness at the contact surface and the size of the shock tube—depends on all the parameters mentioned above.

As presented herein, the theory is restricted to shock-tube flows where the shock wave is weak, and the boundary layers on the walls of the tube are laminar and incompressible. The complete solution of shock-tube flow involving the effects of viscosity is a formidably difficult problem, but it is hoped that the present analysis may be a useful first step towards the full solution.

As a parallel study with the above theoretical work, the design and construction of a shock-tube installation was undertaken. Low cost was one of the main criteria of this design, and a shock tube made of mahogany was finally selected. The shock tube is 34 ft in length and has a cross-section measuring 6 in. by $2\frac{1}{2}$ in. Ancillary equipment was developed for the installation and particular attention was given to the optical and electronic equipment. The development

of the apparatus, and principally that of the electronic instrumentation, took considerable time; but a detailed calibration of the shock tube was ultimately carried out. Experimental results are given in Figs. 62 to 69. To illustrate one main application of the shock tube, that is, the study of unsteady flows, timed photographs of the transient diffraction of a shock wave over a 10-deg wedge were obtained (Figs. 72 to 75); and the influence of the state of the boundary layer on the shock speed was investigated over a small range of Reynolds number (Fig. 70). Several improvements to the existing Bristol shock-tube installation have been suggested in the light of operational experience.

12.2. *Future Development and Uses of Shock Tubes.*—Shock tubes have been employed in widely differing roles in many experimental aerodynamic investigations. Some of these applications have been reviewed in Chapter 1, and the following remarks are intended to clarify the present position of the shock tube as a general purpose research tool.

Detailed investigations[12, 13] of actual shock-tube flow have made clear that the flow region between the shock and the contact surface cannot be described as truly quasi-steady; for example, at a given channel station the Mach number M of the flow behind the shock increased from $1 \cdot 20$ to $1 \cdot 25$ before the passage of the contact surface. Furthermore, if the transverse waves occur, they will cause fluctuations superimposed on the steady rise of Mach number between the shock and the contact surface. Hence this flow region is not truly quasi-steady and, if the transverse waves occur, neither is it uniform. The reasons for the persistence of the transverse waves under certain conditions of operation of the shock tube are not clear at present, but a systematic investigation of the state of the tube-wall boundary layers may help to clarify this problem.

Before the development of slotted walls for transonic wind tunnels, the shock tube was thought[6] to be uniquely suited for transonic investigations; however, it is not now seriously considered as an alternative to a conventional wind tunnel for speeds below $M \simeq 5$, since the flow is not truly steady. The functions of the shock tube in aerodynamic research are now thought to be, firstly, the study of unsteady flow problems such as the diffraction and reflection of shock waves, particularly in the transonic flow region, and secondly, the study of hypersonic flow. In the latter case, the potential development of the shock tube is considerable, since free-flight stagnation temperatures may be achieved without the costly compressors and heaters of the conventional hypersonic wind tunnel. In hypersonic ' combustion-type ' shock tubes[36], the diaphragm pressure ratio is always large enough to produce supersonic flow behind the shock wave; and, if this supersonic flow is expanded by the use of a divergent nozzle in the channel, a flow at a Mach number up to 20 may be generated for a short period of time—say 500 μsec for a channel length of the order of 100 ft.

At the present time, there is growing interest in hypersonic shock tubes, and many such facilities are under development in the United States of America[36, 37] and the United Kingdom[38].

In conclusion, it is the opinion of the present writer that the shock tube is uniquely suited for high-temperature research at hypersonic Mach numbers and for the study of unsteady flow problems; furthermore, the shock tube offers the most economical way of demonstrating and investigating a large variety of steady and unsteady phenomena, and hence a small shock tube would be invaluable for general purpose demonstration and research work in university laboratories.

REFERENCES

No.	Author(s)	Title, etc.
1	P. Vieille	Sur les discontinuites produites par la detente brusque de gas comprimes. Comptes Rendus 129, 1228 (1899).
2	W. Payman and W. C. F. Shepherd	Explosion waves and shock waves. VI. The disturbances produced by bursting diaphragms with compressed air. Proc. Roy. Soc. A Vol. 186, p. 293 (1946).
3	C. I. H. Nicholl	Head-on collision of shock and rarefaction waves. University of Toronto UTIA Report 10 (1951).
4	J. Lukasciewicz	Shock tube theory and applications. N.R.C. (Canada) Report MT–10 (1950).
5	W. Bleakney, D. K. Weimer and C. H. Fletcher.	The shock tube—a facility for investigation in fluid dynamics. Rev. Sci. Instrum. Vol. 20, p. 807 (1949).
6	W. Griffith	Shock tube studies of transonic flow over wedge profiles. Jour. Aero. Sci. Vol. 19, p. 249 (1952).
7	A. Hertzberg	A shock tube method for generating hypersonic flow. Jour. Aero. Sci. Vol. 18, p. 803 (1951).
8	R. W. Perry and A. Kantrowitz	The production and stability of converging shock waves. Jour. Appld. Phys. Vol. 22, p. 878 (1951).
9	P. Wegener and G. Lundquist	Condensation of water vapour in a shock tube below 150° K. Jour. Appld. Phys. Vol. 22, p. 233 (1951).
10	R. Courant and K. O. Friedrichs	Supersonic flow and shock waves. Interscience Publishers, New York (1948).
11	R. C. Pankhurst and D. W. Holder	Wind tunnel technique. Pitman and Son, London (1952).
12	I. I. Glass, W. A. Martin and G. N. Patterson.	A theoretical and experimental study of the shock tube. University of Toronto. UTIA Report 2 (1953). A.R.C. 17, 243—T.P. 441 17th December, 1954.
13	R. J. Emrich and C. W. Curtiss	Attenuation in the shock tube. Jour. Appld. Phys. Vol. 24, p. 360 (1953).
14	R. K. Lobb	A study of supersonic flows in a shock tube. University of Toronto UTIA Report 8 (1950).
15	I. I. Glass	The design of a wave interaction tube. University of Toronto. UTIA Report 6 (1950).
16	R. E. Duff	The interaction of plane shock waves and rough surfaces. Jour. Appld. Phys. Vol. 23, p. 1373 (1952).
17	G. Lundquist	Shock wave formation in a shock tube. Jour. Appld. Phys. Vol. 23, p. 374 (1952).
18	P. W. Huber, C. W. Fitton and F. Delpino.	Experimental investigation of moving pressure disturbances and correlation with one-dimensional unsteady flow theory. N.A.C.A. TN 1903 (1949).
19	A. Hertzberg and A. Kantrowitz	Studies with an aerodynamically instrumented shock tube. Jour. Appld. Phys. Vol. 21, p. 874 (1950).
20	G. Uhlenbeck	Diffraction of shock waves around various obstacles. E.R.I. University of Michigan Project M720–4 (1950).
21	C. du P. Donaldson and R. D. Sullivan	The effect of wall friction on the strength of shock waves in tubes and hydraulic jumps in channels. N.A.C.A. TN 1942 (1949).
22	B. D. Henshall	The construction and operation of a shock tube. Unpublished B.Sc. Thesis, University of Bristol (1952).

61

REFERENCES—*continued*

No.	Author(s)	Title, etc.
23	J. G. Hall	The transition through a contact region. University of Toronto. UTIA Report 26 (1953).
24	P. Niordson	Transmission of shock waves in thin walled cylindrical tubes. Trans. Royal Inst. Tech. Stockholm. No. 57 (1952).
25	E. K. Parks	Supersonic flow in a shock tube of divergent cross-section. University of Toronto. UTIA Report 18 (1952).
26	F. K. Elder and N. de Hass	Experimental study of the formation of a vortex ring at the open end of a cylindrical shock tube. Jour. Appld. Phys. Vol. 23, p. 1065 (1952).
27	D. Bernstein	A double diaphragm shock tube to produce transient high Mach number flows. Jour. Ae. Sc., p. 790, November, 1953.
28	A. Kantrowitz, E. Resler and C. Lin	The production of high temperature gases in shock tubes. Jour. Appld. Phys., Vol. 23, p. 1390 (1952).
29	A. Sommer	Photoelectric tubes. Methuen (1951).
30	R. M. Davies, J. D. Owen and D. H. Trevena.	The measurement of the velocities of bullets with a counter chronometer. Brit. Jour. Appld. Phys., Vol. 2, p. 271, September, 1951.
31	L. F. Lawrence, S. F. Schmidt and F. W. Looschen.	A self-synchronising stroboscopic schlieren system for the study of unsteady air flows. N.A.C.A. TN 2509. October, 1951.
32	R. N. Close and M. T. Lebenbaum	Design of phantastron time delay circuits. Electronics, pp. 100–107. April, 1948.
33	D. W. Holder and R. J. North	The Toepler Schlieren apparatus. R. & M. 2780 (1953).
34	R. J. North	Schlieren systems using graded filters. A.R.C. 15,099—F.M. 1769. 1st August, 1952.
35	W. A. Mair	The sensitivity and range required in a Toepler Schlieren apparatus for photography of supersonic air flow. Communicated by P.D.S.R.(A), M.O.S. A.R.C. 13,861. 13th March, 1951.
36	A. Hertzberg and W. E. Smith	A method for generating strong shock waves. Jour. Appld. Physics, Vol. 25, No. 1. January, 1954.
37	J. A. Dodge	Ultra-high temperature aerodynamic testing facilities. Arnold Engineering Development Centre Report AEDC–TN–54–61 (1954).
38	B. D. Henshall and D. W. Holder	Note on a proposed hypersonic shock tube installation at the N.P.L. Unpublished. January, 1955.
39	W. Chester	The diffraction and reflection of shock waves. Quart. Jour. Mech. and Appld. Maths., Vol. VII, Pt. I (1954).
40	H. H. Pearcey	The indication of boundary-layer transition on aerofoils in the N.P.L. 20 in. × 8 in. high-speed tunnel. A.R.C. Current Paper No. 10 (1950).
41	D. W. Holder and R. J. North	Schlieren methods for observing high-speed flows. A.R.C. Current Paper No. 167 (1954).
42	L. Prandtl	The essentials of fluid dynamics. Blackie and Son, Ltd. (1953).

TABLE 1

Normal Shock Functions

$$\gamma = 1\cdot4$$

$V_+ = \dfrac{U}{a_0}$	$\dfrac{T}{T_0}$	$\dfrac{a}{a_0}$	$\dfrac{u}{a_0}$	$\dfrac{\rho}{\rho_0}$
Given	$(2\cdot27)$	$(2\cdot27)$	$(2\cdot26)$	$(2\cdot28)(3\cdot4)$
1·000	1·000	1·000	0	1·000
1·050	1·033	1·016	0·0813	1·084
1·100	1·065	1·032	0·1591	1·169
1·150	1·097	1·047	0·2337	1·256
1·200	1·128	1·062	0·3055	1·342
1·250	1·159	1·076	0·3750	1·429
1·300	1·191	1·091	0·4423	1·516
1·350	1·223	1·106	0·5079	1·602
1·400	1·255	1·120	0·5715	1·690
1·450	1·287	1·134	0·6335	1·777
1·500	1·320	1·149	0·6945	1·862
1·550	1·354	1·164	0·7539	1·948
1·600	1·388	1·178	0·8125	2·032
1·650	1·423	1·193	0·8699	2·115
1·700	1·459	1·208	0·9265	2·198
1·750	1·494	1·222	0·9821	2·279
1·800	1·532	1·238	1·037	2·359
1·850	1·570	1·253	1·091	2·438
1·900	1·607	1·268	1·145	2·515
1·950	1·647	1·283	1·198	2·592
2·000	1·688	1·299	1·250	2·667
2·10	1·770	1·330	1·353	2·812
2·20	1·857	1·363	1·455	2·951
2·30	1·947	1·395	1·554	3·085
2·40	2·040	1·428	1·653	3·212
2·50	2·138	1·462	1·750	3·333
2·60	2·238	1·496	1·846	3·449
2·70	2·343	1·531	1·942	3·559
2·80	2·452	1·566	2·036	3·664
2·90	2·563	1·601	2·129	3·763
3·00	2·679	1·637	2·222	3·862
3·20	2·922	1·709	2·406	4·031
3·40	3·180	1·783	2·588	4·188
3·60	3·453	1·858	2·768	4·330
3·80	3·743	1·935	2·947	4·456
4·00	4·047	2·012	3·125	4·571

63

TABLE 2

Shock-Tube Flow

$$\gamma = \bar{\gamma} = 1\cdot 4 \qquad T_0 = \bar{T}_0$$

$V_+ = \dfrac{U}{a_0}$	$P = \dfrac{\bar{p}_0}{p_0}$	M	$\overline{M}$	$ps = \dfrac{p}{p_0}$
Given	Eqn. (3.1)	(3.2)	(3.3)	(3.4)
1·000	1·000	0	0	1·000
1·050	1·258	0·0797	0·0827	1·120
1·100	1·560	0·1542	0·1643	1·245
1·150	1·925	0·2228	0·2451	1·377
1·200	2·354	0·2878	0·3254	1·514
1·250	2·862	0·3480	0·4054	1·657
1·300	3·453	0·4054	0·4852	1·805
1·350	4·148	0·4593	0·5651	1·959
1·400	4·958	0·5101	0·6452	2·120
1·450	5·900	0·5583	0·7256	2·287
1·500	7·004	0·6044	0·8064	2·459
1·550	8·282	0·6483	0·8879	2·637
1·600	9·758	0·6897	0·9702	2·820
1·650	11·47	0·7294	1·053	3·010
1·700	13·45	0·7670	1·137	3·205
1·750	15·73	0·8033	1·222	3·407
1·800	18·39	0·8383	1·308	3·614
1·850	21·47	0·8709	1·396	3·827
1·900	24·99	0·9028	1·485	4·045
1·950	29·03	0·9331	1·575	4·270
2·000	33·71	0·9622	1·667	4·500
2·10	45·30	1·017	1·855	4·979
2·20	60·80	1·068	2·051	5·480
2·30	81·38	1·114	2·256	6·005
2·40	108·8	1·138	2·469	6·554
2·50	145·4	1·197	2·692	7·125
2·60	198·5	1·234	2·927	7·720
2·70	260·3	1·268	3·174	8·339
2·80	349·1	1·300	3·434	8·980
2·90	469·1	1·330	3·709	9·645
3·00	633·2	1·358	4·000	10·37
3·20	1,166	1·408	4·639	11·78
3·40	2,190	1·451	5·366	13·32
3·60	4,242	1·490	6·203	14·96
3·80	8,493	1·523	7·179	16·68
4·00	17,740	1·553	8·333	18·50

TABLE 3

Position and Duration of Quasi-steady Flow behind the Shock

$V_+ = \dfrac{U}{a_0}$	$\dfrac{u}{\bar{U}}$	$\dfrac{V_-}{V_+}$	$\dfrac{X_0}{X_2}$	$\dfrac{X_0}{\tau}$
Given	(3.6)	(3.7)	(3.8)	(3.9)
1·000	0	1·000	∞	0·5
1·050	0·0774	0·9381	6·768	0·5963
1·100	0·1446	0·8843	3·776	0·7021
1·150	0·2032	0·8375	2·787	0·8174
1·200	0·2546	0·7963	2·298	0·9419
1·250	0·3000	0·7600	2·008	1·076
1·300	0·3402	0·7278	1·817	1·218
1·350	0·3762	0·6991	1·682	1·370
1·400	0·4082	0·6735	1·584	1·529
1·450	0·4369	0·6505	1·508	1·697
1·500	0·4630	0·6296	1·448	1·873
1·550	0·4864	0·6109	1·400	2·056
1·600	0·5078	0·5937	1·361	2·247
1·650	0·5272	0·5783	1·329	2·445
1·700	0·5450	0·5640	1·301	2·649
1·750	0·5612	0·5510	1·278	2·860
1·800	0·5761	0·5391	1·258	3·077
1·850	0·5899	0·5281	1·240	3·300
1·900	0·6025	0·5180	1·225	3·528
1·950	0·6142	0·5087	1·212	3·762
2·000	0·6250	0·5000	1·200	4·000
2·10	0·6444	0·4845	1·180	4·491
2·20	0·6612	0·4711	1·164	4·999
2·30	0·6758	0·4604	1·151	5·519
2·40	0·6887	0·4491	1·140	6·054
2·50	0·7000	0·4400	1·131	6·597
2·60	0·7101	0·4319	1·123	7·153
2·70	0·7191	0·4248	1·117	7·717
2·80	0·7270	0·4184	1·110	8·282
2·90	0·7342	0·4126	1·106	8·857
3·00	0·7407	0·4074	1·101	9·438
3·20	0·7520	0·3984	1·094	10·61
3·40	0·7612	0·3910	1·088	11·80
3·60	0·7690	0·3848	1·083	12·98
3·80	0·7756	0·3795	1·080	14·18
4·00	0·7813	0·3750	1·076	15·38

65

TABLE 4

Position and Duration of Quasi-steady Flow behind the Contact Surface

$\bar{M}$	X_1	X_2	$t_2 = 2t_1$	$\bar{\tau}$
Table 2	Eqn. (3.14)	(3.15)	(3.16)	(3.13) $\bar{M} < 1$ (3.17) $\bar{M} > 1$
0	— 1·0	0	1·0	2·000
0·0827	— 0·9476	0·1709	1·050	1·940
0·1643	— 0·8917	0·3506	1·102	1·893
0·2451	— 0·8304	0·5392	1·154	1·854
0·3254	— 0·7650	0·7380	1·208	1·823
0·4054	— 0·6950	0·9478	1·263	1·797
0·4852	— 0·6193	1·167	1·320	1·778
0·5651	— 0·5388	1·400	1·379	1·762
0·6452	— 0·4524	1·645	1·439	1·749
0·7256	— 0·3597	1·902	1·502	1·741
0·8064	— 0·2612	2·176	1·566	1·734
0·8879	— 0·1555	2·463	1·633	1·730
0·9702	— 0·0425	2·767	1·702	1·728
1·053	0·0776	3·085	1·774	1·685
1·137	0·2064	3·427	1·849	1·626
1·222	0·3439	3·786	1·927	1·577
1·308	0·4903	4·165	2·008	1·535
1·396	0·6479	4·568	2·093	1·499
1·485	0·8158	4·996	2·182	1·469
1·575	0·9942	5·446	2·274	1·444
1·667	1·186	5·928	2·371	1·422
1·855	1·607	6·975	2·577	1·389
2·051	2·090	8·159	2·804	1·367
2·256	2·645	9·502	3·056	1·355
2·469	3·277	11·02	3·333	1·350
2·692	4·005	12·74	3·641	1·353
2·927	4·843	14·71	3·985	1·361
3·174	5·811	16·97	4·369	1·376
3·434	6·925	19·54	4·799	1·397
3·709	8·219	22·51	5·284	1·425
4·000	9·720	25·92	5·832	1·458
4·639	13·52	34·48	7·164	1·544
5·366	18·77	46·13	8·911	1·661
6·203	26·12	62·28	11·25	1·814
7·179	36·66	85·19	14·45	2·013
8·333	52·14	118·5	18·96	2·275

TABLE 5

Shock-Tube Flow : Reynolds Numbers and Conditions at the Contact Surface

V_+	$\dfrac{M}{\overline{M}} = \dfrac{a}{\overline{\overline{a}}}$	$\dfrac{T}{\overline{\overline{T}}}$	$\dfrac{\rho}{\overline{\overline{\rho}}}$	$\dfrac{[Re]_{\overline{M}}}{[Re]_M}$
Given	Table 2	Eqn. (4.3)	(4.3)	(4.6)
1·000	1·000	1·000	1·000	1·000
1·050	1·038	1·077	0·9285	1·138
1·100	1·065	1·135	0·8811	1·249
1·150	1·100	1·210	0·8264	1·396
1·200	1·131	1·278	0·7825	1·537
1·250	1·165	1·357	0·7369	1·707
1·300	1·197	1·432	0·6983	1·875
1·350	1·230	1·514	0·6605	2·066
1·400	1·265	1·600	0·6250	2·276
1·450	1·300	1·689	0·5921	2·505
1·500	1·334	1·780	0·5618	2·743
1·550	1·370	1·876	0·5330	3·007
1·600	1·407	1·979	0·5053	3·301
1·650	1·444	2·084	0·4798	3·616
1·700	1·482	2·198	0·4550	3·965
1·750	1·521	2·314	0·4322	4·342
1·800	1·560	2·435	0·4107	4·745
1·850	1·603	2·569	0·3893	5·214
1·900	1·645	2·706	0·3695	5·708
1·950	1·688	2·849	0·3510	6·247
2·000	1·732	3·002	0·3331	6·845
2·10	1·824	3·327	0·3006	8·196
2·20	1·920	3·688	0·2711	9·815
2·30	2·025	4·101	0·2438	11·82
2·40	2·170	4·707	0·2124	15·04
2·50	2·249	5·058	0·1977	17·06
2·60	2·372	5·626	0·1777	20·55
2·70	2·503	6·266	0·1596	24·81
2·80	2·642	6·978	0·1433	29·96
2·90	2·789	7·777	0·1286	36·22
3·00	2·946	8·676	0·1153	43·86
3·20	3·295	10·86	0·09208	64·92
3·40	3·698	13·68	0·07310	97·26
3·60	4·163	17·33	0·05770	147·2
3·80	4·714	22·22	0·04500	227·4
4·00	5·366	28·79	0·03473	357·8

E *

TABLE 6

Shock-Tube Flow : Reynolds Numbers/Foot $[Re] \times 10^{-7}$

Specimen Case : $\bar{p}_0 = 200$ lb/sq in. (Gauge)

$[Re]_{\bar{M}\,\text{max}} = 48 \times 10^6$; $[Re]_{M\,\text{max}} = 17 \cdot 8 \times 10^6$

$\bar{M}$	$[Re]_{\bar{M}}$	$[Re]_{M}$	$\dfrac{[Re]_{\bar{M}}}{[Re]_{M}}$
Table 2	Eqn. (4.7)	Eqn. (4.8)	Eqn. (4.6)
0	0	0	1·000
0·0827	0·7998	0·7028	1·138
0·1643	1·478	1·183	1·249
0·2451	2·057	1·473	1·396
0·3254	2·551	1·660	1·537
0·4054	2·972	1·741	1·707
0·4852	3·330	1·776	1·875
0·5651	3·634	1·759	2·066
0·6452	3·891	1·710	2·276
0·7256	4·107	1·640	2·505
0·8064	4·288	1·563	2·743
0·8879	4·423	1·471	3·007
0·9702	4·548	1·378	3·301
1·053	4·631	1·280	3·616
1·137	4·715	1·189	3·965
1·222	4·762	1·097	4·342
1·308	4·778	1·007	4·745
1·396	4·801	0·9208	5·214
1·485	4·797	0·8404	5·708
1·575	4·781	0·7653	6·247
1·667	4·760	0·6954	6·845
1·855	4·668	0·5695	8·196
2·051	4·550	0·4636	9·815
2·256	4·398	0·3721	11·82
2·469	4·220	0·2806	15·04
2·692	4·038	0·2367	17·06
2·927	3·836	0·1867	20·55
3·174	3·614	0·1457	24·81
3·434	3·398	0·1134	29·96
3·709	3·177	0·08771	36·22
4·000	2·956	0·06740	43·86
4·639	2·517	0·03877	64·92
5·366	2·101	0·02160	97·26
6·203	1·710	0·01162	147·2
7·179	1·361	0·00599	227·4
8·333	1·049	0·00293	357·8

TABLE 7

Shock Tube : Entropy Variations

Let $\bar{s} = 0$; then by (4.12) $\dfrac{s}{C_v} > \dfrac{s - s_0}{C_v}$

V_+	$\dfrac{s}{C_v}$	$\dfrac{s - s_0}{C_v}$	$\dfrac{s_0}{C_v}$
Given	Eqn. (4.11)	(4.10)	Cols. 2 and 3
1·000	0	0	0
1·050	0·1039	0·00012	0·1038
1·100	0·1773	0·00051	0·1768
1·150	0·2669	0·0017	0·2652
1·200	0·3434	0·0027	0·3407
1·250	0·4274	0·0046	0·4228
1·300	0·5027	0·0085	0·4942
1·350	0·5807	0·0129	0·5678
1·400	0·6580	0·0174	0·6406
1·450	0·7338	0·0224	0·7114
1·500	0·8073	0·0289	0·7784
1·550	0·8808	0·0364	0·8444
1·600	0·9556	0·0443	0·9113
1·650	1·028	0·0531	0·9749
1·700	1·103	0·0631	1·040
1·750	1·175	0·0719	1·103
1·800	1·246	0·0833	1·163
1·850	1·321	0·0947	1·226
1·900	1·394	0·1051	1·289
1·950	1·466	0·1180	1·348
2·000	1·539	0·1315	1·408
2·100	1·683	0·1573	1·526
2·200	1·827	0·1861	1·641
2·300	1·976	0·2159	1·760
2·400	2·169	0·2460	1·923
2·500	2·269	0·2786	1·990
2·600	2·418	0·3105	2·108
2·700	2·569	0·3436	2·225
2·800	2·720	0·3780	2·342
2·900	2·872	0·4114	2·461
3·000	3·025	0·4444	2·581
3·200	3·339	0·5144	2·825
3·400	3·662	0·5840	3·078
3·600	3·993	0·6530	3·340
3·800	4·341	0·7221	3·619
4·000	4·704	0·7900	3·914

TABLE 8

Shock-Tube Performance

$$\gamma = \bar{\gamma} = 1\cdot40; \quad T_0 = \bar{T}_0 \qquad\qquad \bar{p}_0 \text{ measured in lb/sq in. absolute}$$

$$[Re]_{M\,\max} = 82{,}770\bar{p}_0 \text{ at } \bar{M} = 0\cdot391 \qquad\qquad [Re]_{\bar{M}\,\max} = 223{,}600\bar{p}_0 \text{ at } \bar{M} = 1\cdot429$$

1	2	3	4	5	6	7	8	9	10	11	12
V_+	P	M	$\bar{M}$	p_s	$X_1 = 2X_1'$	X_2	$\bar{\tau}$	$\dfrac{\tau}{\tau}$	$\tau = 2\tau'$	$X_0 = 2X_0'$	$\dfrac{[Re]_{\bar{M}}}{[Re]_M}$
Given	Eqn. (3.1)	(3.2)	(3.3)	(3.4)	(3.14)	(3.15)	(3.13) (3.17)	(3.19)	Cols. 8 and 9	(3.9) and Col. 10	(4.6)
1·000	1·000	0	0	1·000	—1·0	0	2·000	1·000	2·000	1·000	1·000
1·050	1·258	0·0797	0·0827	1·120	—0·9476	0·1709	1·940	0·9988	1·939	1·157	1·138
1·100	1·560	0·1542	0·1643	1·245	—0·8917	0·3506	1·893	0·9959	1·886	1·324	1·249
1·150	1·925	0·2228	0·2451	1·377	—0·8304	0·5392	1·854	0·9921	1·839	1·503	1·396
1·200	2·354	0·2878	0·3254	1·514	—0·7650	0·7380	1·823	0·9880	1·801	1·696	1·537
1·250	2·862	0·3480	0·4054	1·657	—0·6950	0·9478	1·797	0·9838	1·768	1·903	1·707
1·300	3·453	0·4054	0·4852	1·805	—0·6193	1·167	1·778	0·9799	1·742	2·120	1·875
1·350	4·148	0·4593	0·5651	1·959	—0·5388	1·400	1·762	0·9765	1·720	2·355	2·066
1·400	4·958	0·5101	0·6452	2·120	—0·4524	1·645	1·749	0·9735	1·703	2·606	2·276
1·450	5·900	0·5583	0·7256	2·287	—0·3597	1·902	1·741	0·9715	1·691	2·868	2·505
1·500	7·004	0·6044	0·8064	2·459	—0·2612	2·176	1·734	0·9700	1·683	3·151	2·743
1·550	8·282	0·6483	0·8879	2·637	—0·1555	2·463	1·730	0·9698	1·677	3·448	3·007
1·600	9·758	0·6897	0·9702	2·820	—0·0425	2·767	1·728	0·9698	1·676	3·766	3·301
1·650	11·47	0·7294	1·053	3·010	+0·0776	3·085	1·685	0·9957	1·677	4·100	3·616
1·700	13·45	0·7670	1·137	3·205	0·2064	3·427	1·626	1·034	1·682	4·459	3·965
1·750	15·73	0·8033	1·222	3·407	0·3439	3·786	1·577	1·072	1·692	4·839	4·342
1·800	18·39	0·8383	1·308	3·614	0·4903	4·165	1·535	1·110	1·703	5·240	4·745

TABLE 8—*continued*

1	2	3	4	5	6	7	8	9	10	11	12
V_+	P	M	$\overline{M}$	p_s	$X_1 = 2X_1'$	X_2	τ	$\dfrac{\tau}{\overline{\tau}}$	$\tau = 2\tau'$	$X_0 = 2X_0'$	$\dfrac{[Re]_{\overline{M}}}{[Re]_M}$
Given	Eqn. (3.1)	(3.2)	(3.3)	(3.4)	(3.14)	(3.15)	(3.13) (3.17)	(3.19)	Cols. 8 and 9	(3.9) and Col. 10	(4.6)
1·850	21·47	0·8709	1·396	3·827	0·6479	4·568	1·499	1·145	1·716	5·664	5·214
1·900	24·99	0·9028	1·485	4·045	0·8158	4·996	1·469	1·180	1·734	6·120	5·708
1·950	29·03	0·9331	1·575	4·270	0·9942	5·446	1·444	1·215	1·755	6·601	6·247
2·000	33·71	0·9622	1·667	4·500	1·186	5·928	1·422	1·249	1·777	7·114	6·845
2·100	45·30	1·017	1·855	4·979	1·607	6·975	1·389	1·320	1·833	8·231	8·196
2·200	60·80	1·068	2·051	5·480	2·090	8·159	1·367	1·390	1·900	9·497	9·815
2·300	81·38	1·114	2·256	6·005	2·645	9·502	1·355	1·462	1·982	10·94	11·82
2·400	108·8	1·138	2·469	6·554	3·277	11·02	1·350	1·538	2·075	12·56	15·04
2·500	145·4	1·197	2·692	7·125	4·005	12·74	1·353	1·615	2·184	14·41	17·06
2·600	198·5	1·234	2·927	7·720	4·843	14·71	1·361	1·696	2·309	16·52	20·55
2·700	260·3	1·268	3·174	8·339	5·811	16·97	1·376	1·784	2·456	18·96	24·81
2·800	349·1	1·300	3·434	8·980	6·925	19·54	1·397	1·875	2·619	21·69	29·96
2·900	469·1	1·330	3·709	9·645	8·219	22·51	1·425	1·972	2·811	24·90	36·22
3·000	633·2	1·358	4·000	10·37	9·720	25·92	1·458	2·074	3·024	28·54	43·86
3·200	1,166	1·408	4·639	11·78	13·52	34·48	1·544	2·302	3·554	37·72	64·92
3·400	2,190	1·451	5·366	13·32	18·77	46·13	1·661	2·562	4·255	50·19	97·26
3·600	4,242	1·490	6·203	14·96	26·12	62·28	1·814	2·867	5·198	67·45	147·2
3·800	8,493	1·523	7·179	16·68	36·66	85·19	2·013	3·223	6·490	92·00	227·4
4·000	17,740	1·553	8·333	18·50	52·14	118·5	2·275	3·647	8·293	127·5	357·8

TABLE 9

Shock-Tube Calibration

Series 1A

Chamber pressure $\bar{p}_0$	Channel pressure p_0	Pressure ratio P		Corrected chronometer reading	Theoretical chronometer reading
mm Hg	mm . Hg	Max	Min	μ Sec	μ Sec
754	636	1·19	1·18	2,589	2,584
754	614	1·23	1·22	2,575	2,568
754	594	1·27	1·26	2,561	2,552
754	570	1·33	1·32	2,538	2,529
754	501	1·51	1·50	2,470	2,459
754	435	1·74	1·73	2,399	2,385
763	448	1·71	1·70	2,426	2,394
763	386	1·98	1·97	2,359	2,318
763	344	2·22	2·21	2,294	2,264
763	312	2·45	2·44	2,248	2,217
763	218	3·52	3·48	2,113	2,058
764	255	3·01	2·98	2,163	2,127
764	231	3·32	3·29	2,125	2,084
765	280	2·74	2·72	2,202	2,168
765	232	3·31	3·28	2,129	2,085
765	204	3·77	3·73	2,070	2,027
765	190	4·05	4·01	2,031	1,997
765	154	4·97	4·94	1,960	1,915
765	133	5·80	5·71	1,895	1,859
765	118	6·54	6·43	1,879	1,815
759	115	6·66	6·54	1,867	1,810
759	89	8·63	8·43	1,776	1,722
759	70	11·0	10·7	1,710	1,643

TABLE 10

Shock-Tube Calibration

Series 1B

Chamber pressure $\bar{p}_0$	Channel pressure p_0	Pressure ratio P		Corrected chronometer reading	Theoretical chronometer reading
mm Hg	mm Hg	Max	Min	μ Sec	μ Sec
1,380	161	8·72	8·43	1,792	1,718
1,540	166	9·42	9·13	1,769	1,695
1,850	164	11·4	11·1	1,699	1,633
1,605	121	13·5	13·0	1,658	1,584
1,740	127	13·9	13·5	1,631	1,573
2,780	157	17·9	17·5	1,567	1,502
2,365	125	19·2	18·7	1,556	1,483
3,035	136	22·6	22·0	1,517	1,440
3,245	118	27·9	27·1	1,477	1,388
3,440	99	35·3	34·3	1,419	1,335
3,090	63	50·1	48·0	1,336	1,262
3,465	59	60·0	57·5	1,292	1,227

Series 1C

935	765	1·24	1·20	2,572	2,569
960	765	1·27	1·24	2,565	2,556
990	765	1·31	1·27	2,561	2,542
1,020	765	1·35	1·31	2,550	2,527
1,045	765	1·39	1·35	2,536	2,511
1,075	765	1·42	1·39	2,520	2,498
1,100	765	1·46	1·42	2,501	2,484
1,160	765	1·54	1·50	2,479	2,453
1,325	762	1·76	1·72	2,399	2,382
1,540	762	2·04	2·00	2,340	2,305
1,745	762	2·31	2·27	2,282	2,248
1,950	762	2·58	2·54	2,229	2,197
1,950	762	2·58	2·54	2,233	2,197

TABLE 11

Shock-Tube Calibration

Series 2

Chamber pressure $\bar{p}_0$	Channel pressure p_0	Pressure ratio P		Corrected chronometer reading	Theoretical chronometer reading
mm Hg	mm Hg	Max	Min	μ Sec	μ Sec
1,050	761	1·40	1·36	1,258	1,252
761	515	1·48	1·47	1,236	1,233
761	381	2·00	1·99	1,168	1,158
757	267	2·84	2·82	1,089	1,073
761	187	4·09	4·05	1,022	997
761	135	5·68	5·60	954	932
761	98	7·85	7·69	902	875
761	71	10·9	10·6	840	822
2,780	174	16·2	15·8	806	763
3,040	144	21·4	20·9	769	726
3,040	102	30·2	29·4	725	684
3,040	78	39·7	38·3	694	654
3,325	61	55·7	53·4	657	620

Series 3

Chamber pressure $\bar{p}_0$	Channel pressure p_0	Pressure ratio P		Corrected chronometer reading	Theoretical chronometer reading
1,050	763	1·40	1·36	1,263	1,252
763	505	1·51	1·50	1,233	1,228
763	327	2·34	2·32	1,136	1,120
763	234	3·27	3·25	1,068	1,042
763	164	4·68	4·62	1,005	969
763	114	6·75	6·63	934	902
763	82	9·42	9·08	867	846
2,780	208	13·5	13·2	830	789
3,040	163	18·9	18·4	785	743
3,040	119	25·9	25·2	746	703
3,040	84	36·8	35·6	698	663
3,270	59	56·8	54·3	653	618

74
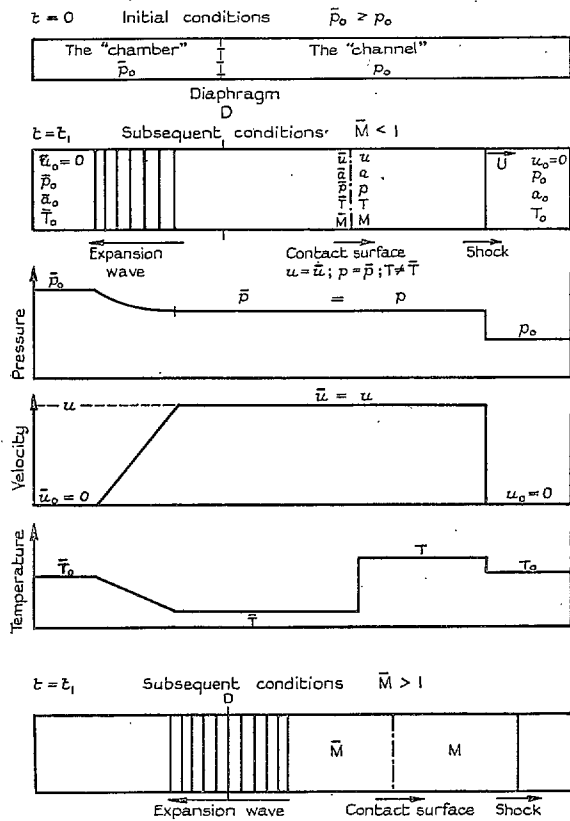
FIG 1. Flow variables in a shock tube.
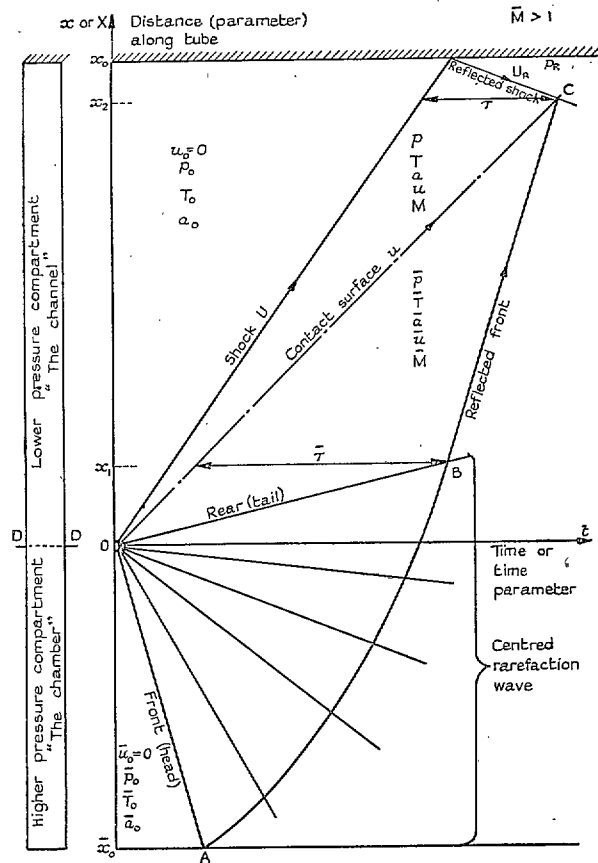
FIG. 2. Shock-tube flow: $t - x$ diagram.
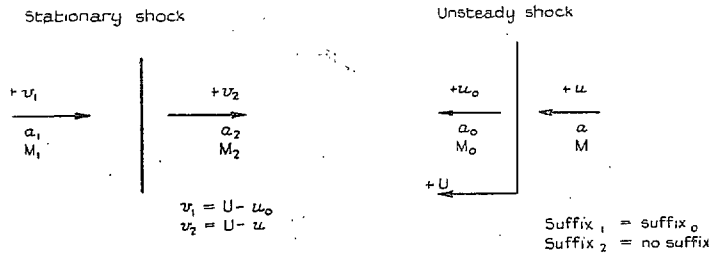
FIG. 3. Notation
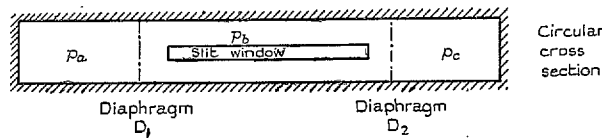
FIG. 4. 'Double' shock tube for the study of the interactions of shocks, rarefactions and temperature discontinuities.
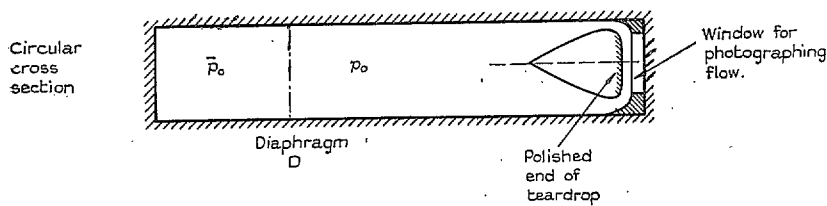
FIG. 5. Shock tube for the production of converging cylindrical shocks.
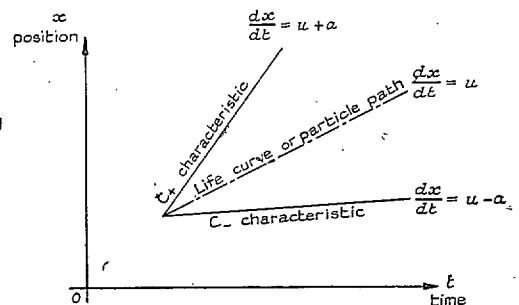
FIG. 6. Characteristics and life curves.

75
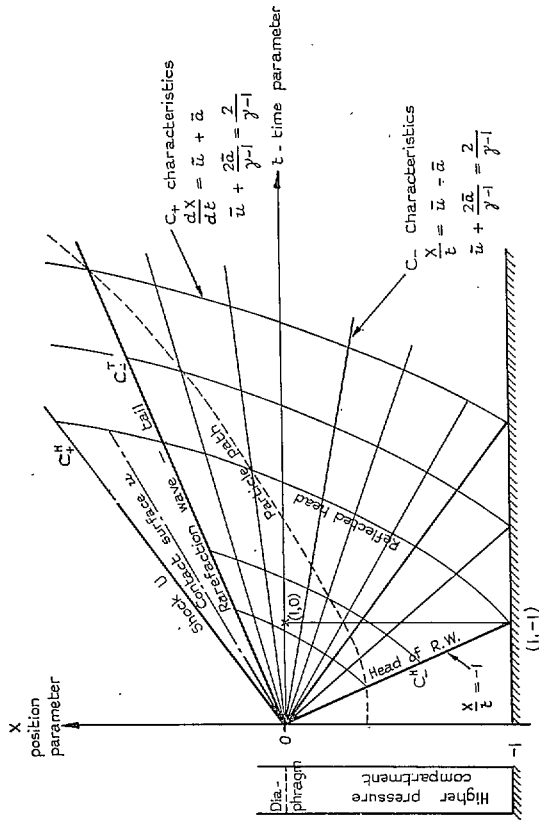
FIG. 7. Characteristics for a backward facing centred rarefaction wave.
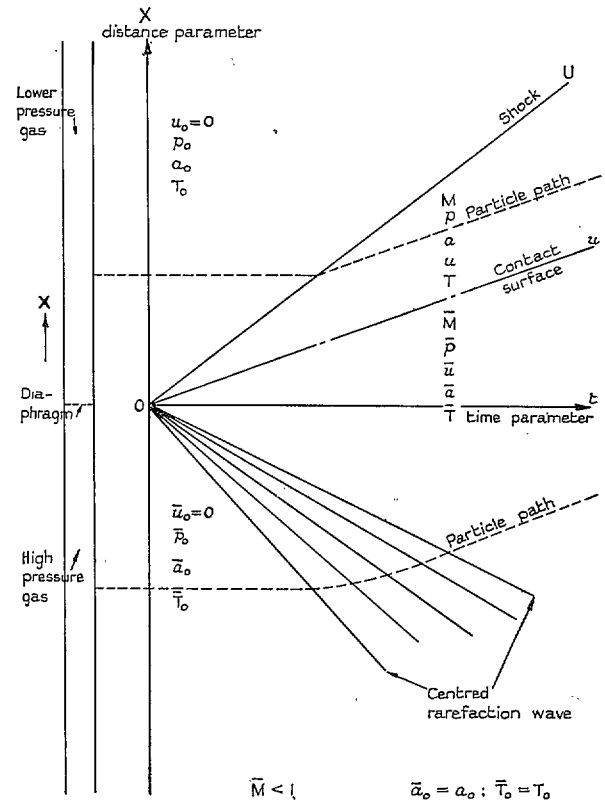
FIG. 8. Gas motion in a doubly infinite shock tube.
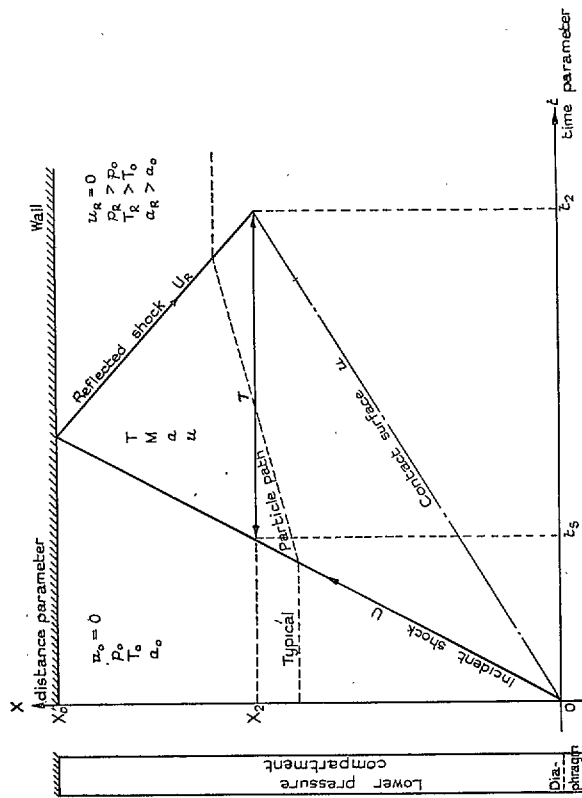
FIG. 9. Reflection of a normal shock from a rigid wall.
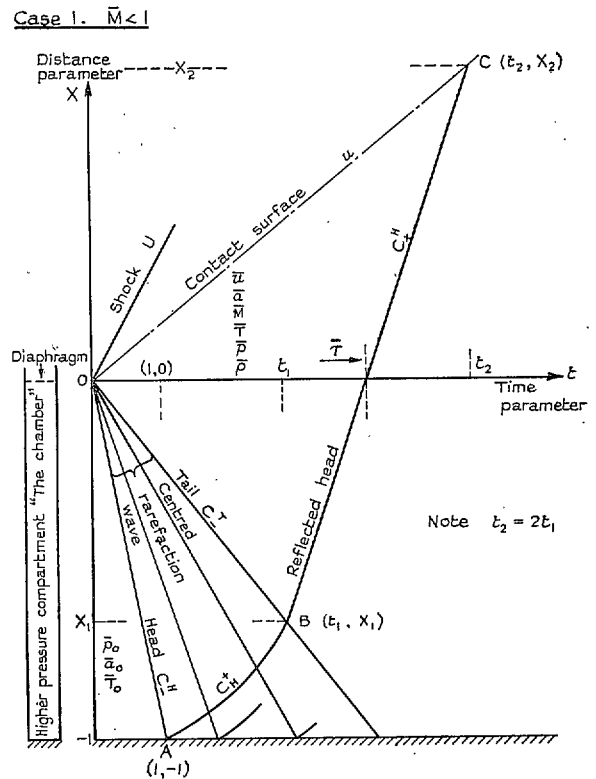
FIG. 10. Quasi-steady flow duration behind the contact surface.
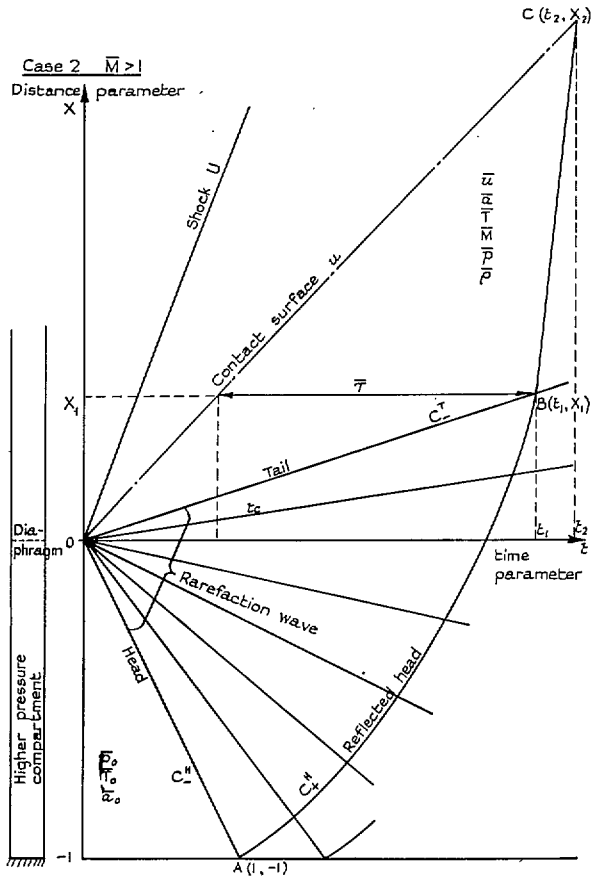
FIG. 11.   Quasi-steady flow duration behind the contact surface.
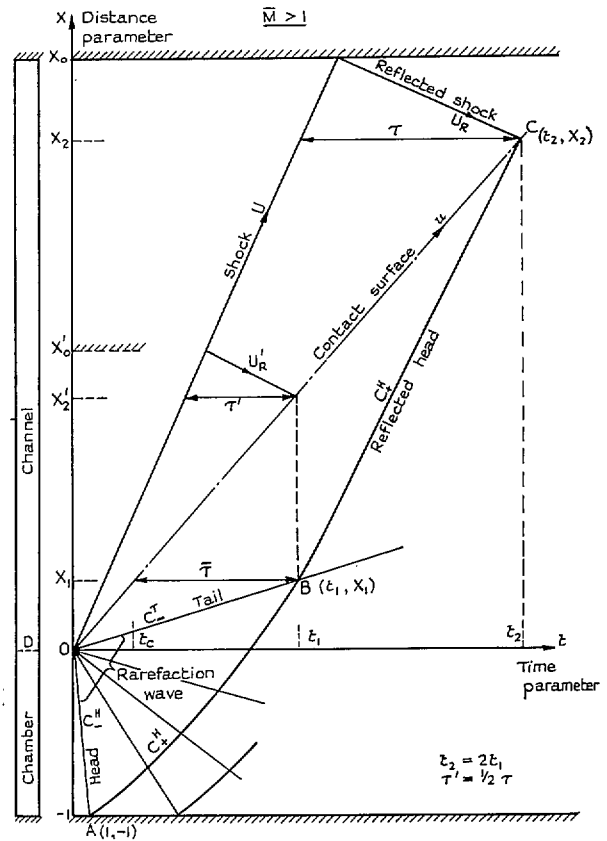
FIG. 12.   Correlation of quasi-steady flow durations.
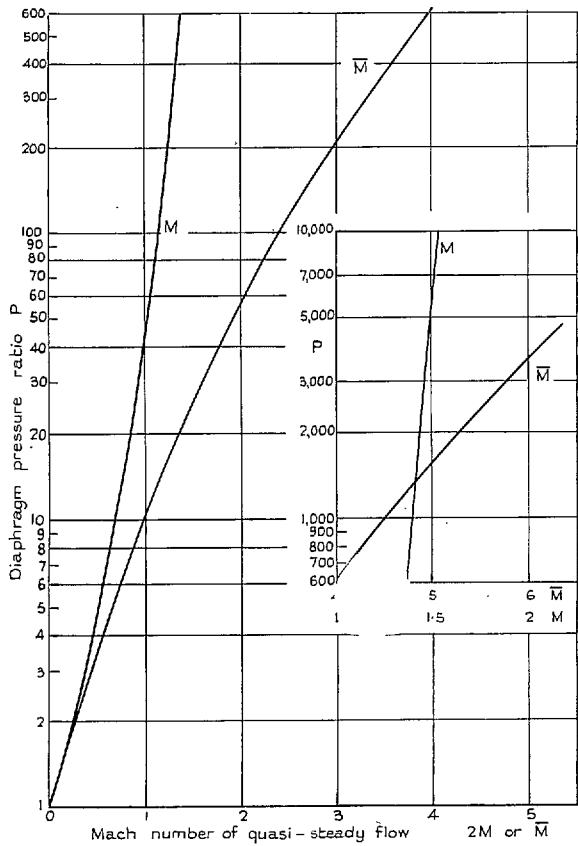
FIG. 13.   Shock tube—performance chart A.
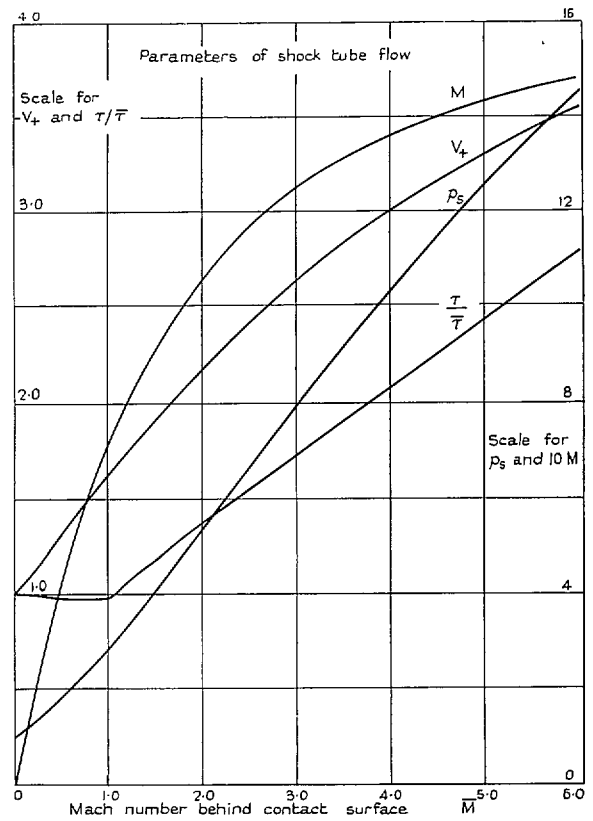
FIG. 14.   Shock tube—performance chart B.

77
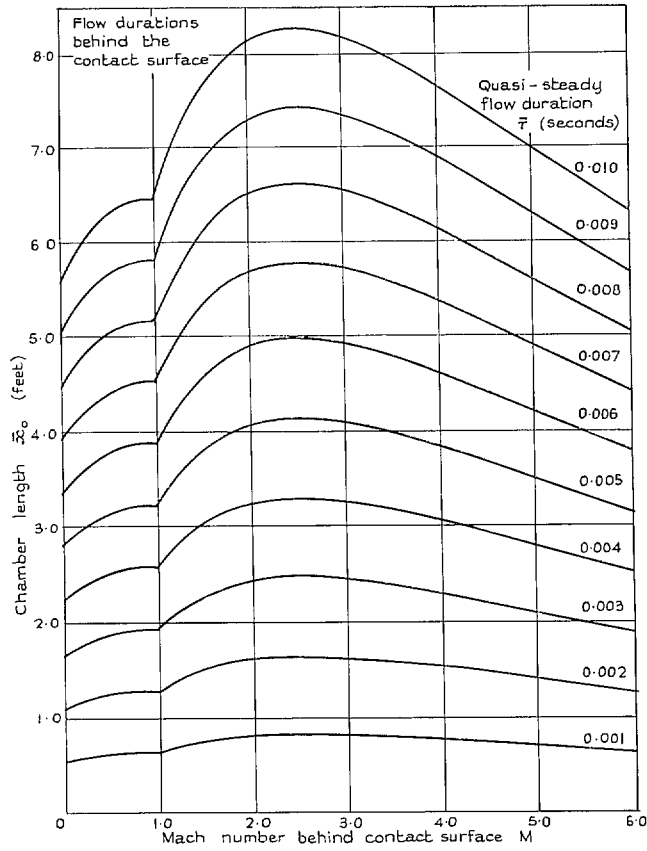
FIG. 15. Shock tube—performance chart C.
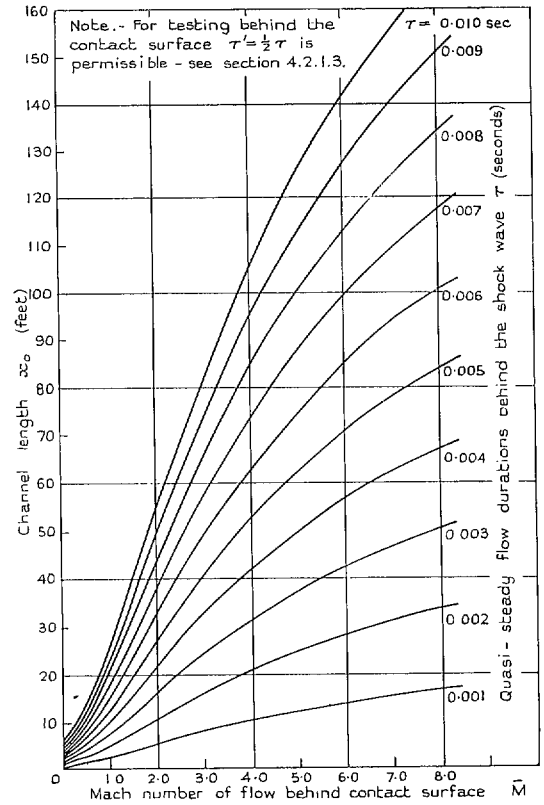
FIG. 16. Shock tube—performance chart D.
Flow durations behind the shock wave.
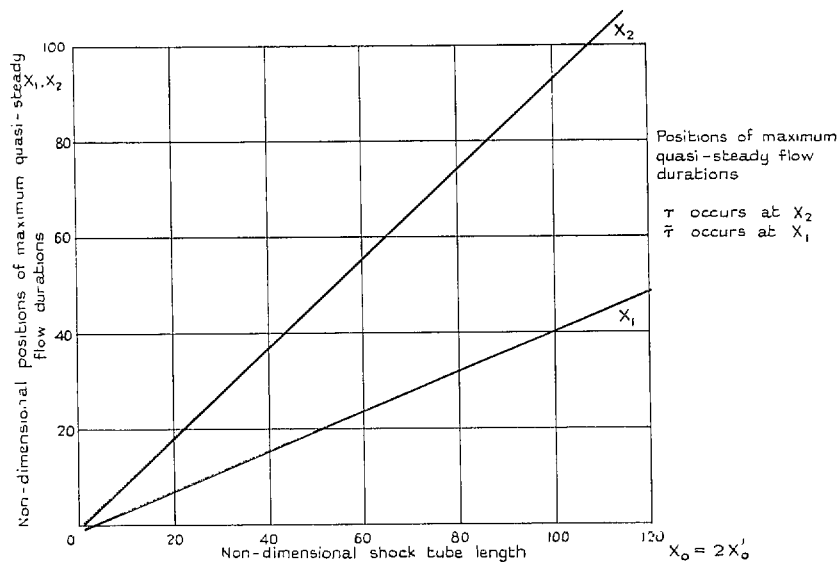
FIG. 17. Shock tube—performance chart E.

78
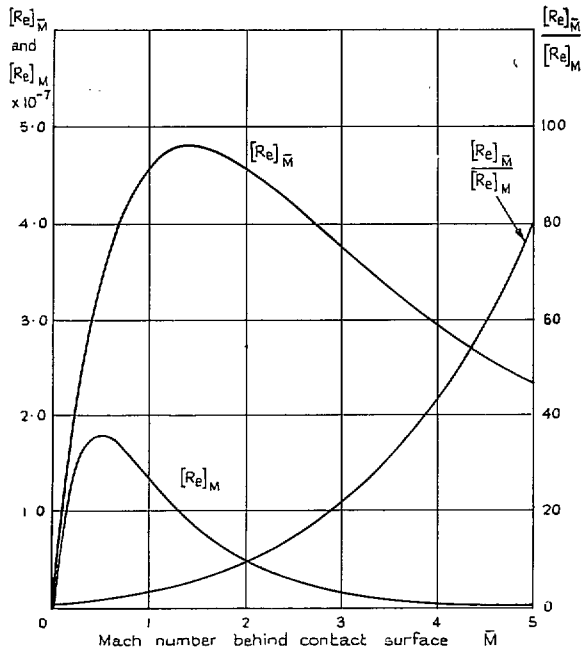
FIG. 18. Shock tube—performance chart F. Shock tube Reynolds numbers.

Values given are for chamber pressure of $\bar{p}_0 = 200$ lb/sq. in. (gauge). For other $\bar{p}_0$, the Reynolds numbers per foot are in direct proportion to those given above.

Case: $P = 17.0$ $\bar{p}_0 = 50$ lb/$\square''$ (gauge)
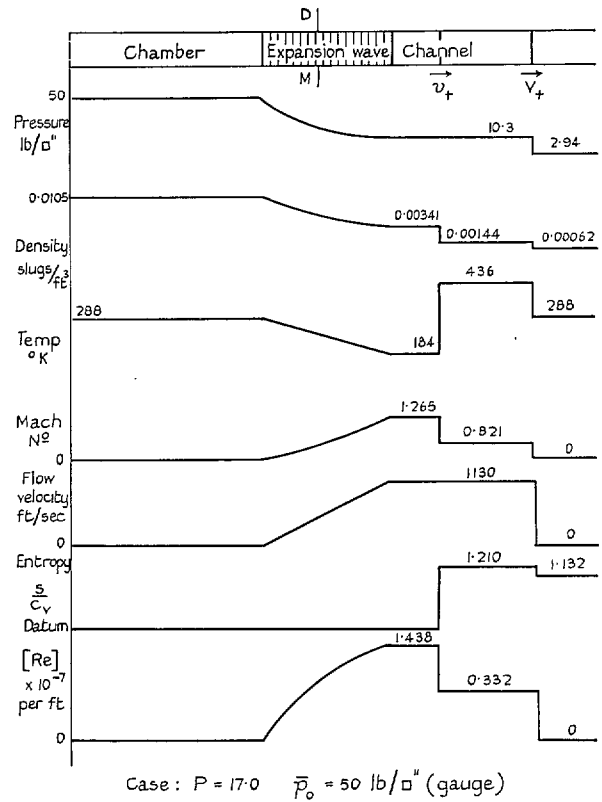
FIG. 19. Variation of flow parameters along a shock tube after diaphragm rupture.

(a) Weak waves. $V_+ < 1.7$

(b) Strong waves. $V_+ > 1.7$
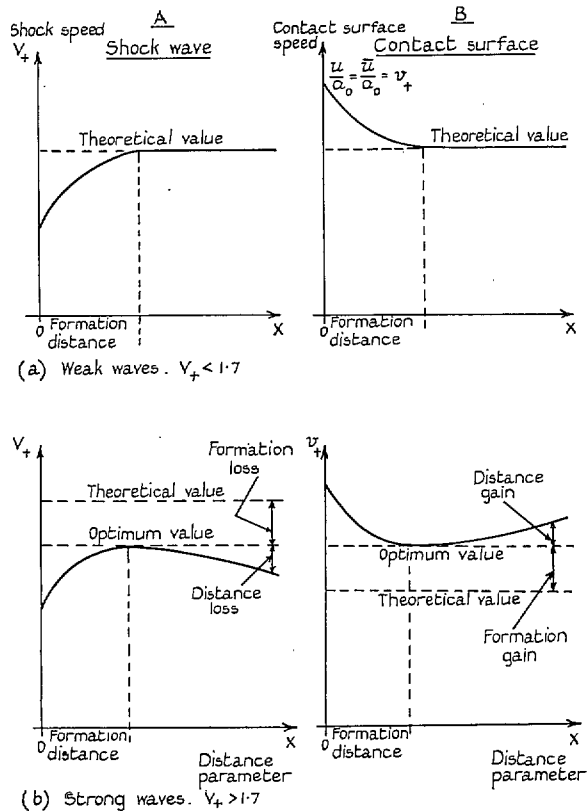
FIG. 20. Experimental data: shock wave and contact surface.
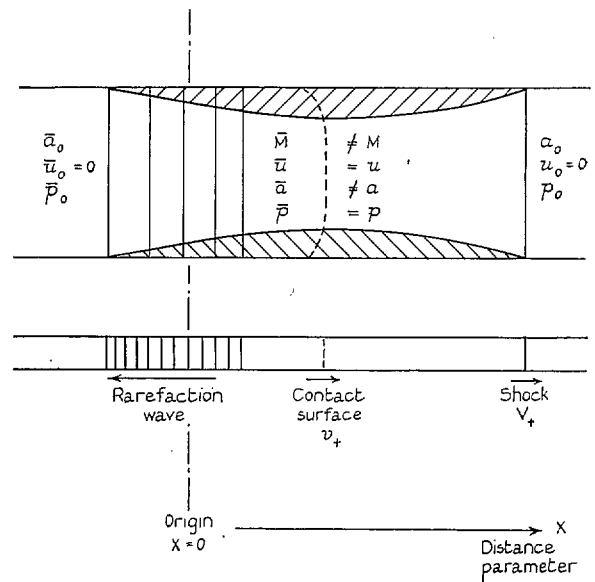
FIG. 21. Shock tube: boundary-layer growth.

Probable extent of shock tube boundary-layer at some instant t after diaphragm rupture.

79
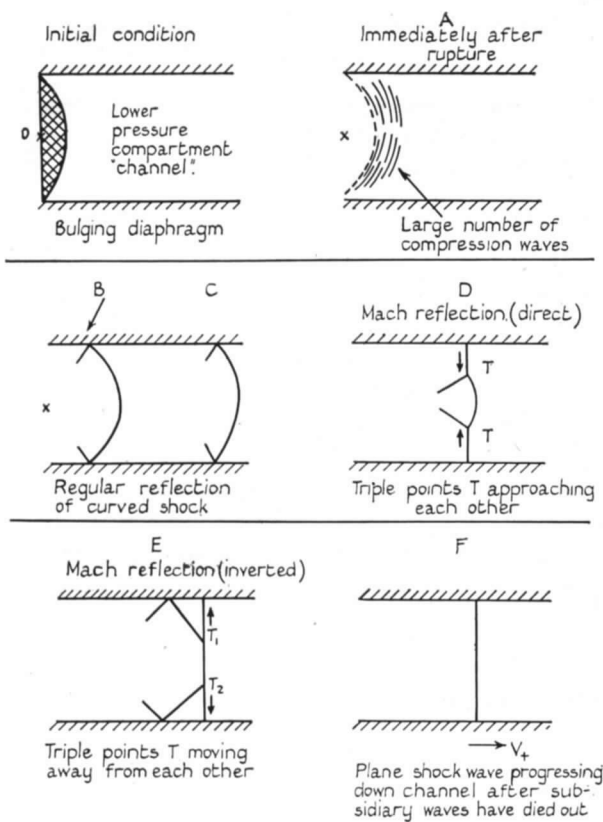
FIG. 22. Shock tube: the formation of a plane shock wave.
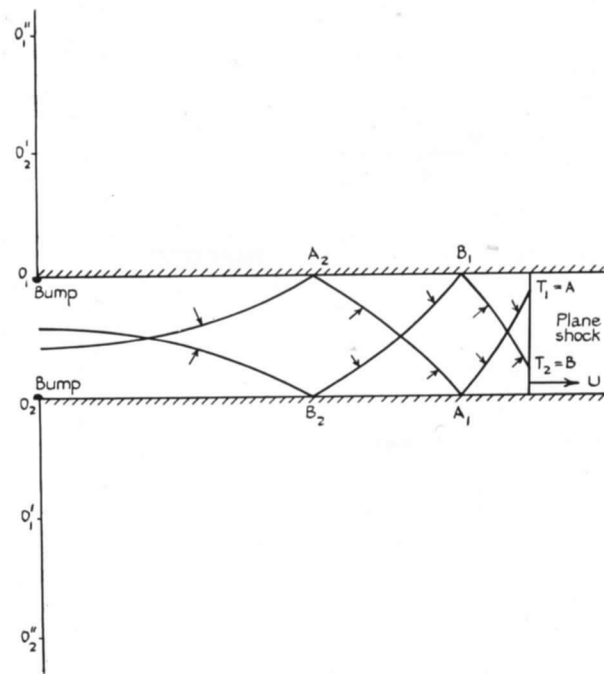
FIG. 23. Shock tube: transverse waves.

Geometrical drawing : pattern formed in a shock tube by successive reflections in the side walls of a cylindrical diffracted wave.
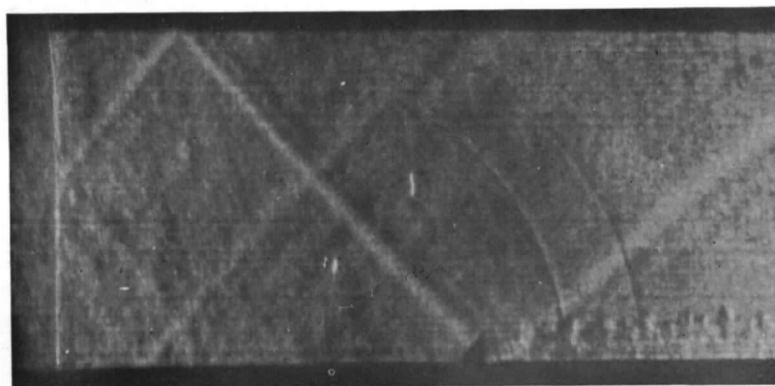
$V_+ = 1 \cdot 42$ $M = 0 \cdot 53$ $p_0 = 1$ atmosphere $[R_e]_M = 7 \cdot 06 \times 10^6$
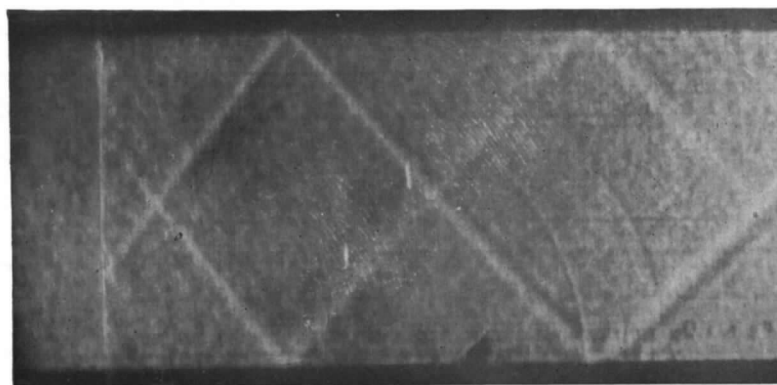
$V_+ = 1 \cdot 34$ $M = 0 \cdot 45$ $p_0 = 1$ atmosphere $[R_e]_M = 5 \cdot 33 \times 10^6$

FIG. 24. Photographs of transverse waves in a 4 in. $\times$ 1$\frac{3}{4}$ in. shock tube.

80
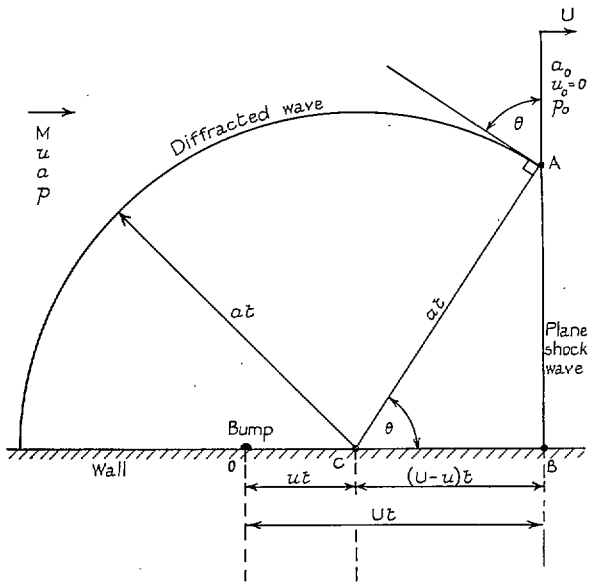
$t = 0$ plane shock hits bump at 0.
$t = t_1$ diffracted wave as shown.

FIG. 25.   Diffraction of a plane shock wave by a
small bump on a tube wall.
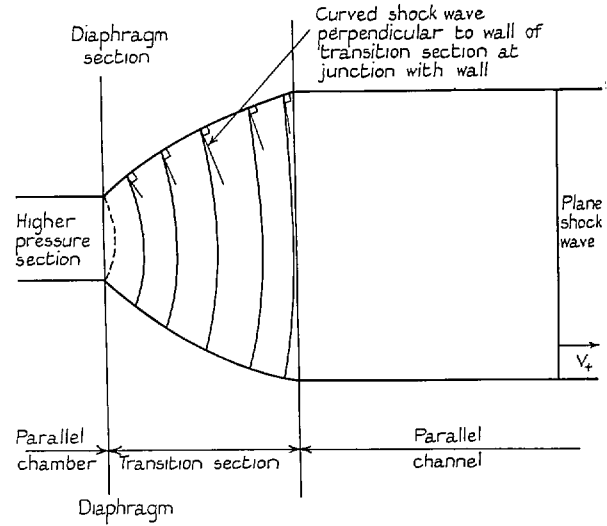
FIG. 27.   A proposed method for the elimination of the
transverse shock waves from shock-tube flow.

Two-dimensional representation only.
Three-dimensional   effects   may   be
included in a similar way.
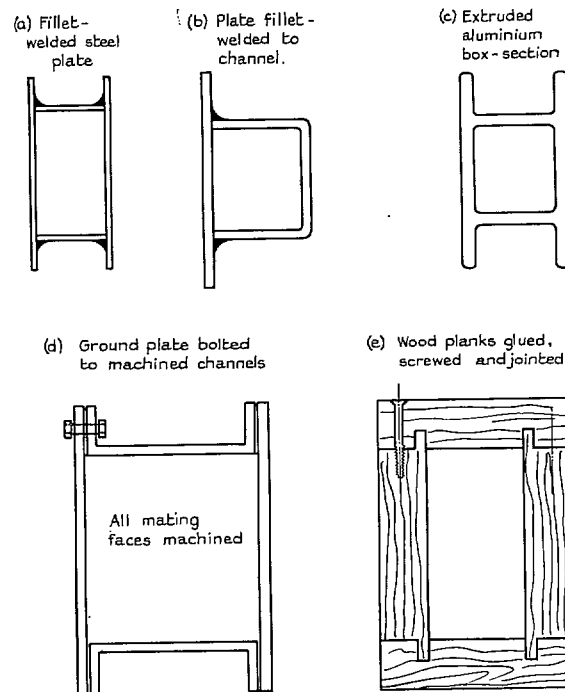
FIG. 28.   Possible methods of shock-tube construction.

81

FIG. 29.

Light screen section Working section

Chamber B Channel 12 5 4 2 2 1 5

Table A Table B Table C

Gauge control panel

Timing equipment Table D

Compressor and storage bottles 200 lb/sq. in.

Work bench

Induced flow tunnel

Stone floor

Optical Table E

System Table F

Table G

Steps

Cupboard 6 ft high

2 ft wind tunnel

Wood floor

Cupboard 4 ft high Work bench Cupboard 4 ft high

Door D₂

20 ft

Door D₁ Window w/s Window

Chamber 12 5 4 2 2 1 6

Floor level

Mirror stand

Table A Table B Table C

Scale ~ 1" = 5 ft

Wooden supports for channel marked ↑

3 ft

23 ft 20 ft

FIG. 29.   Schematic layout of shock tube in laboratory.

FIG. 30.

Diaphragm section

Safety valve S₂ 200 lb/sq. in.

V₄ Air inlet valve

High pressure section up to 200 lb/sq. in. "Chamber"

Low pressure section evacuated to >25 mm mercury "Channel"

V₂

Air storage bottle 200 lb/sq. in.

Safety valve S₁ 200 lb/sq. in.

Vacustat gauge G₄

9 mm vacuum tubing

V₃

Vacuum tap Edwards type 407

V₅ Type ISP 30

V₆ Type IS 50

V₇ Water jet C 20

0-250 lb/sq. in.

Saunders valve V₁

Air compressor 250 lb/sq. in.

Gauge control panel

G₁

G₂

G₃ P₂

P₁

Barometer (mercury)

Mercury U-tube vacuum gauge

Edwards vacuum pumps

G₁ 0-250 lb/sq in 6" diam
G₂ 0-120 lb/sq. in. 10" diam
G₃ 0-30 in Hg 6" diam
G₄ 0-10 mm Hg Type IB

P₁; P₂ Budenburg panel-shut-off valves

FIG. 30.   Schematic diagram: shock-tube installation—pipework.
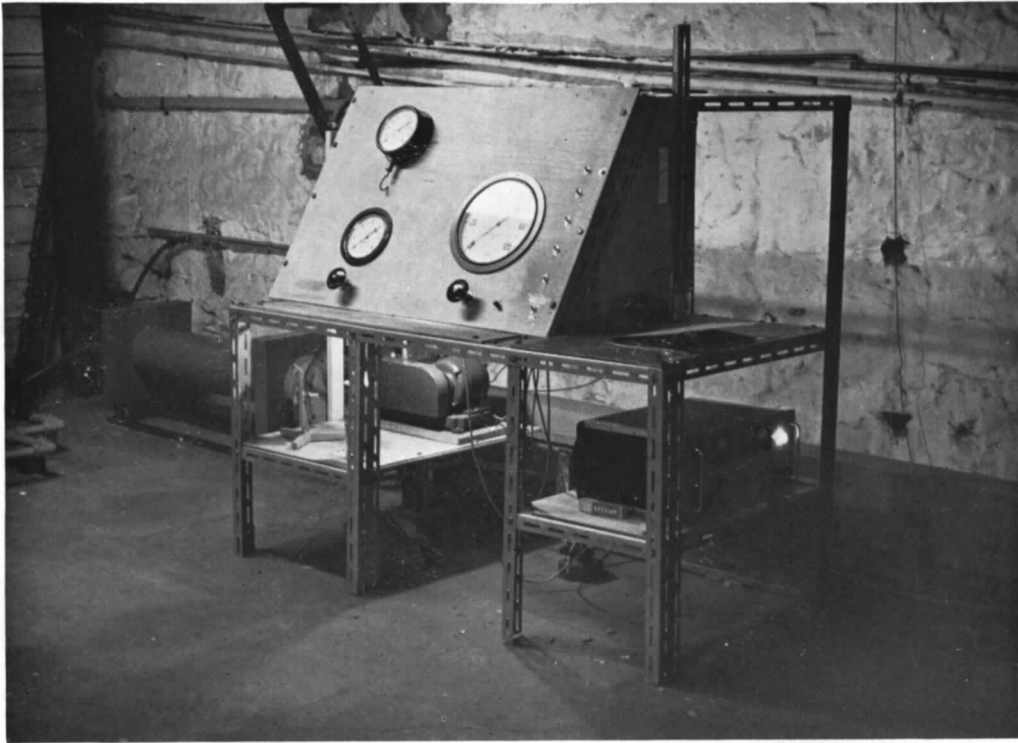
FIG. 31. Control panel of shock tube.
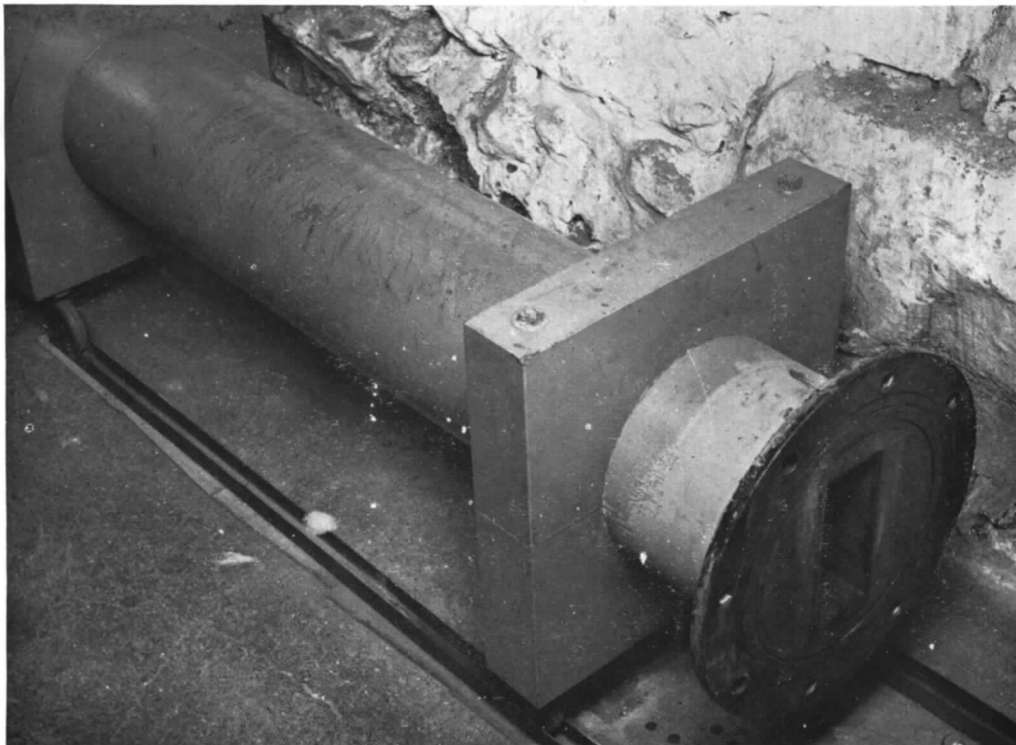
FIG. 32. Chamber of shock tube.

83
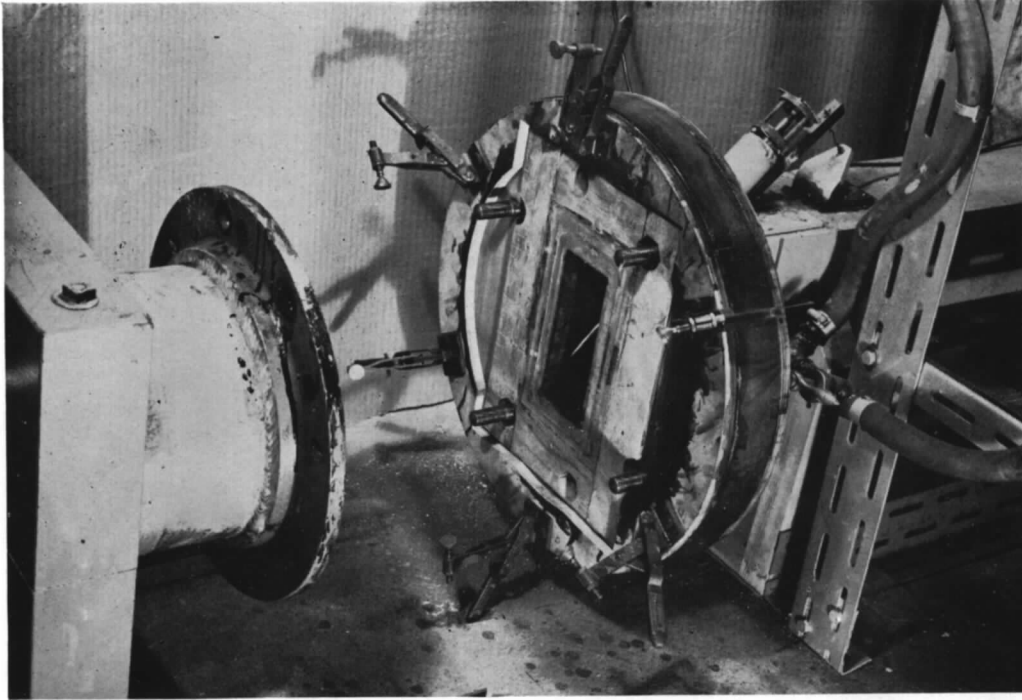
FIG. 33.   Diaphragm joint of shock tube.
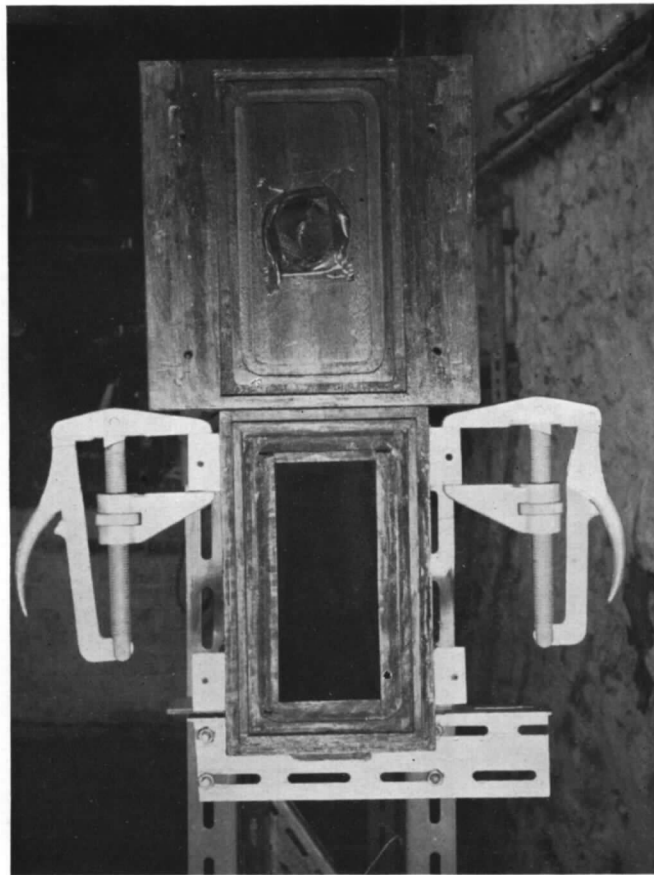
FIG. 34.   Channel joint of shock tube.

84
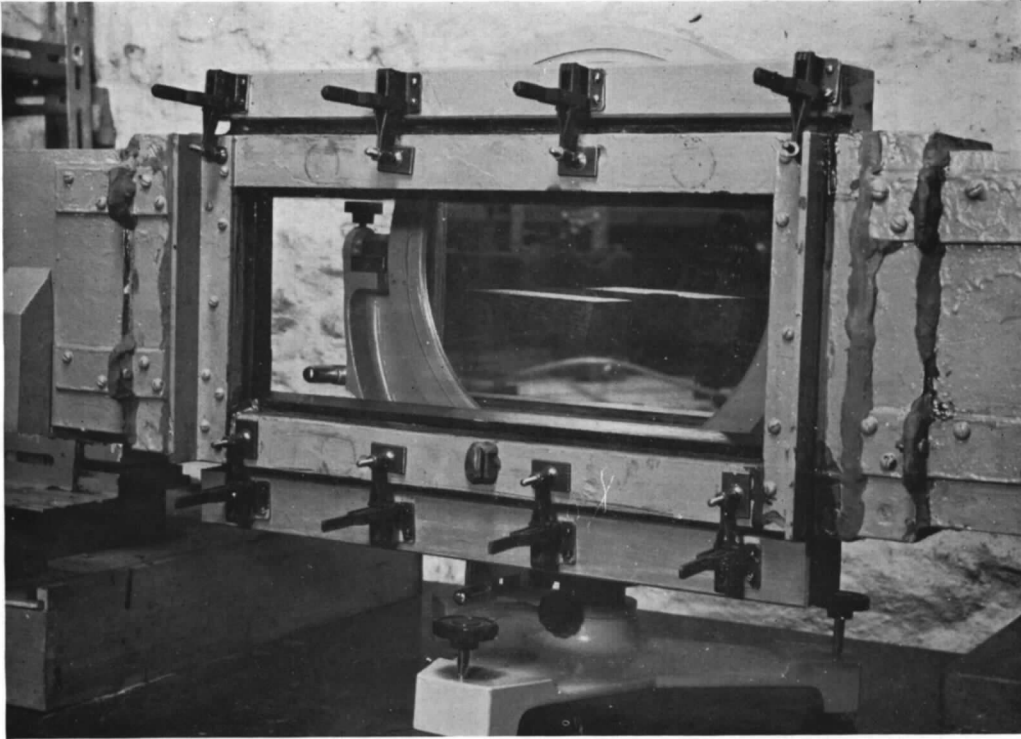
Fig. 35. Working-section of shock tube.
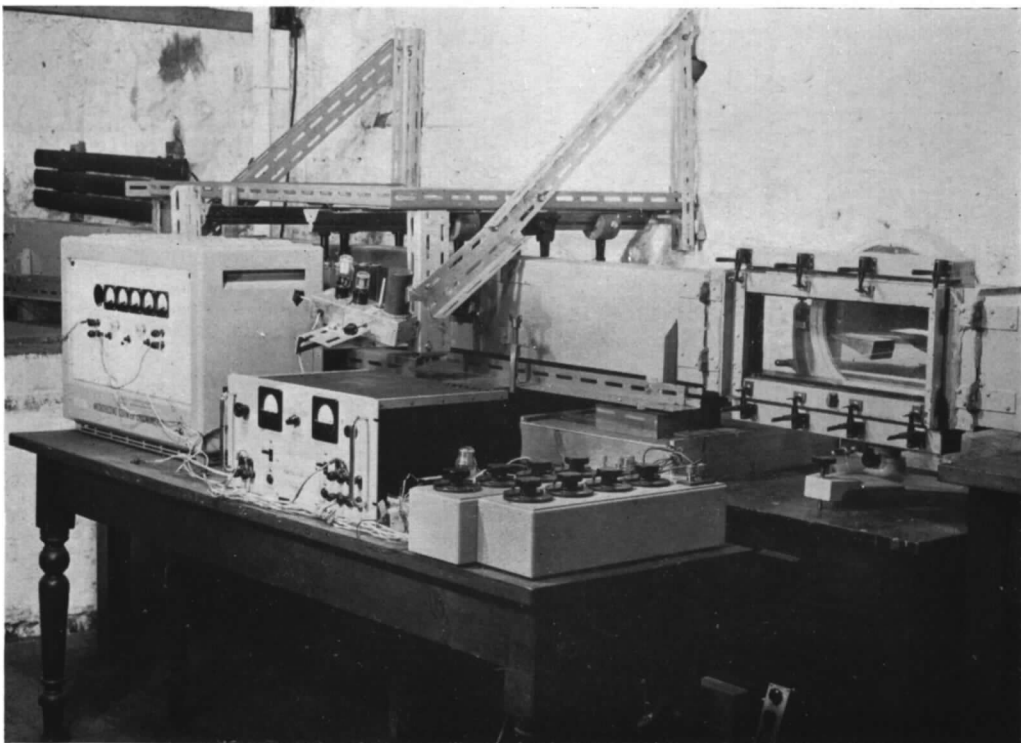
Fig. 36. Overall view of shock tube.
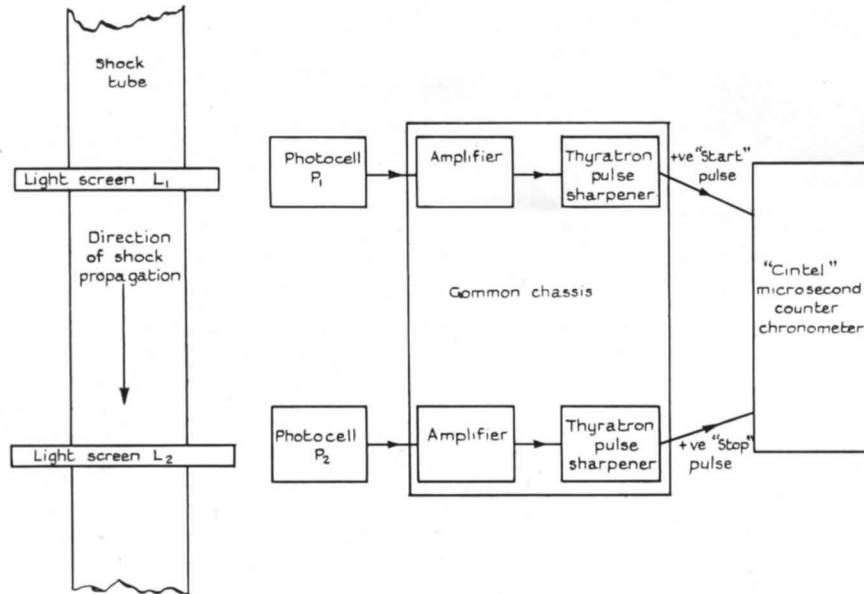
FIG. 37.   Measurement of shock speed by light screens (Schematic).
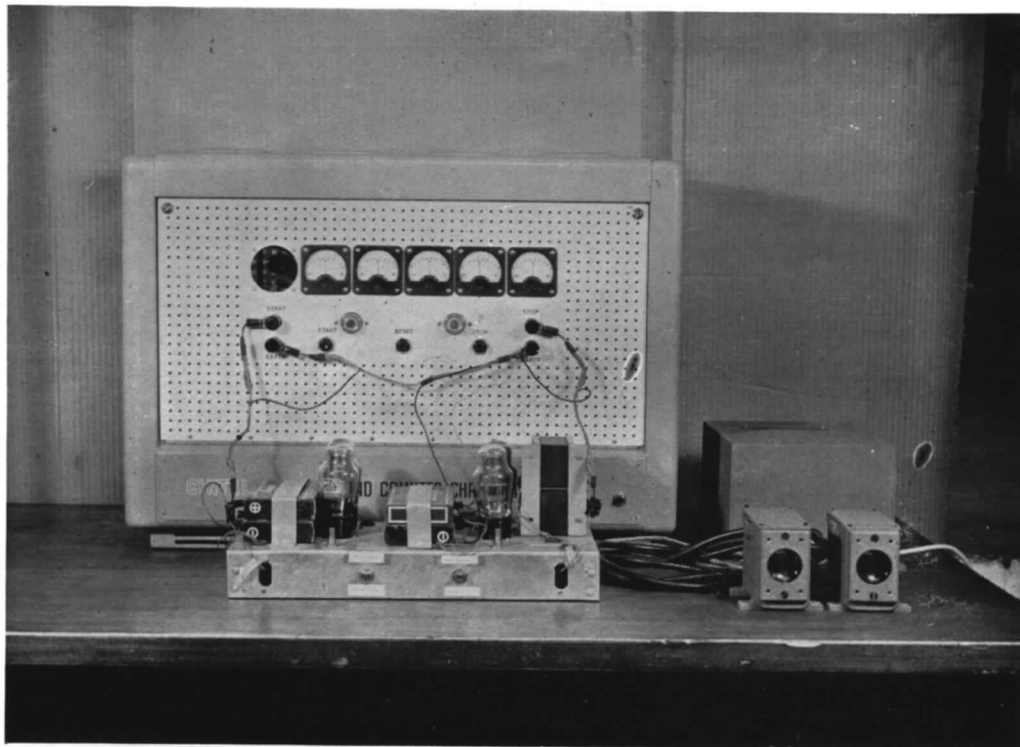
FIG. 38.   Photocell units and chronometer.
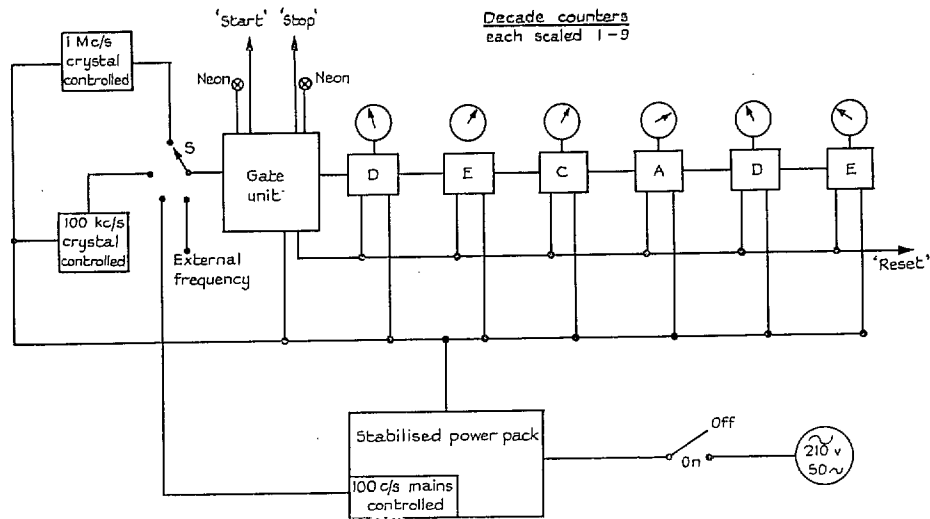
FIG. 39.   Schematic diagram : microsecond counter chronometer.
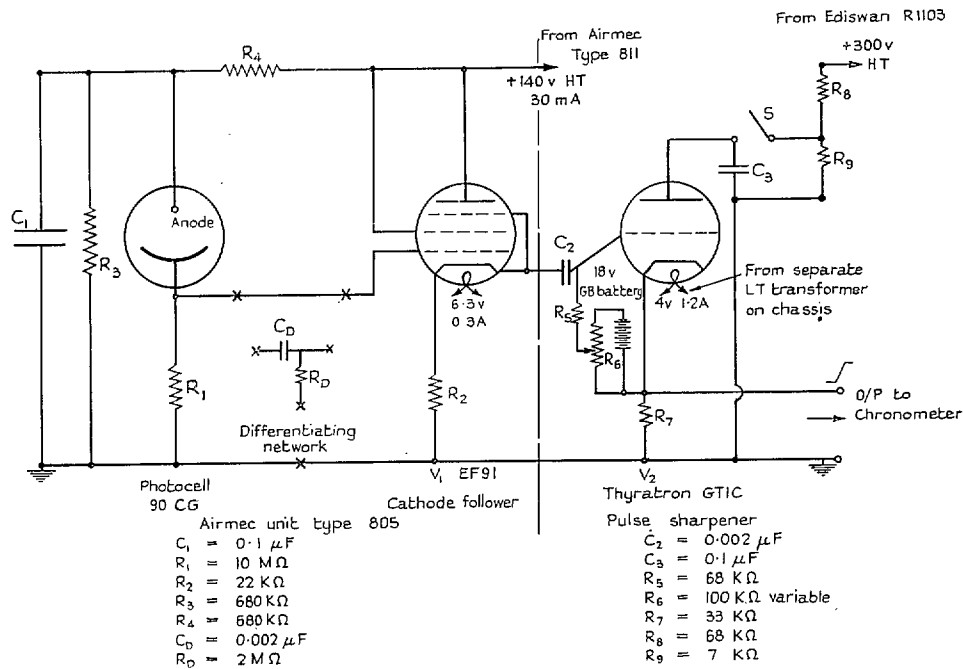
FIG. 40.   Photocell equipment—circuit diagram.
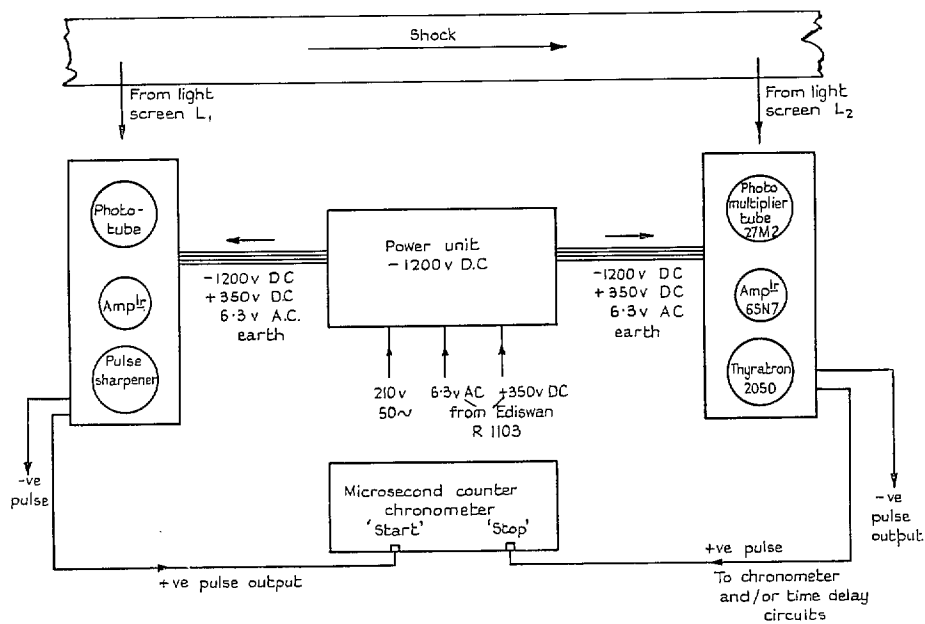
FIG. 41.   Block diagram of photomultiplier units.

87
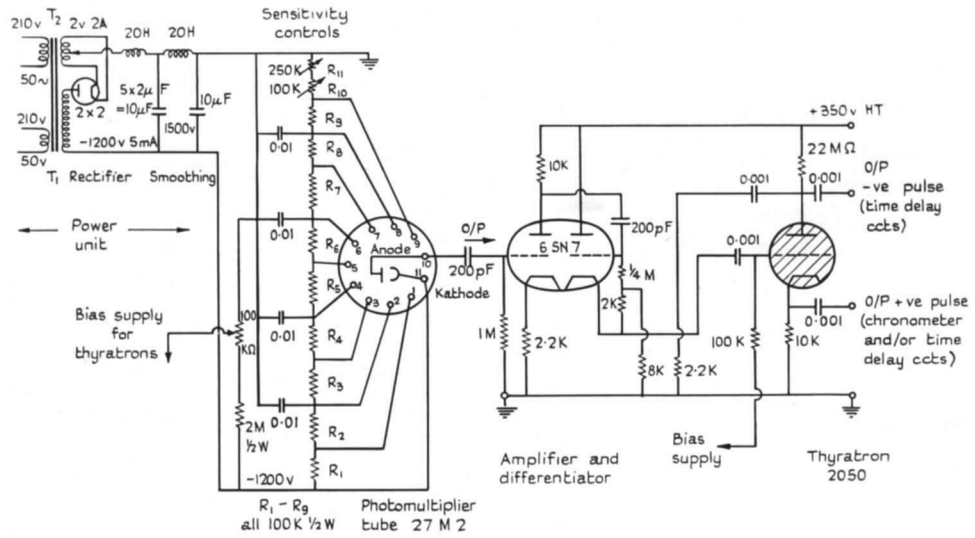
FIG. 42.   Photomultiplier units: circuit diagram.
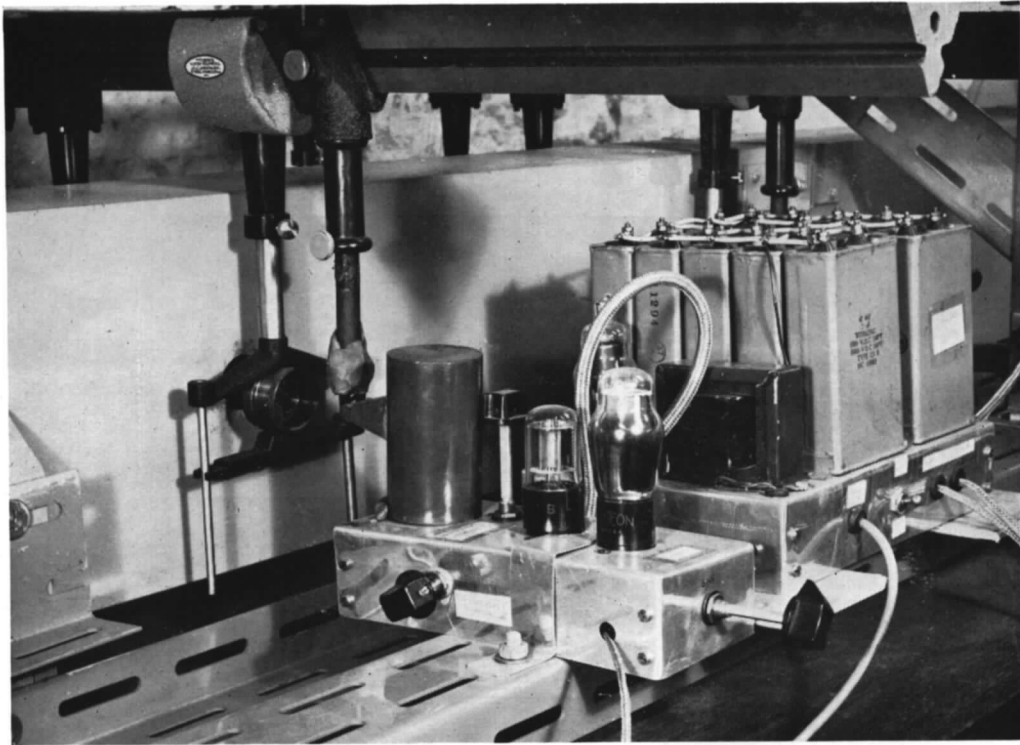
FIG. 43.   Light screen and photomultiplier unit.
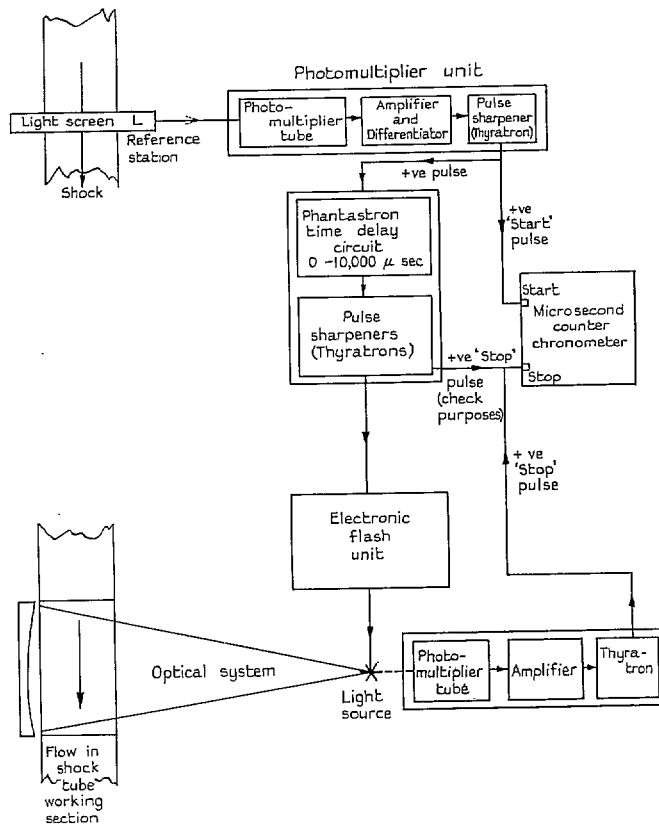
FIG. 44. Schematic diagram : Timed photographs of the flow patterns.
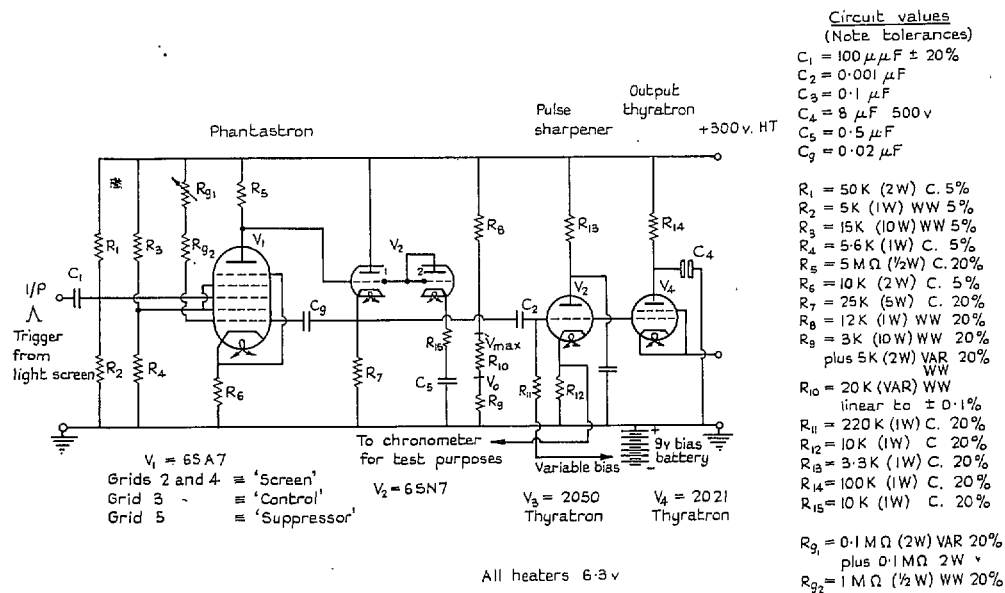
FIG. 45. Phantastron time delay circuit (10,000 μsec).

89
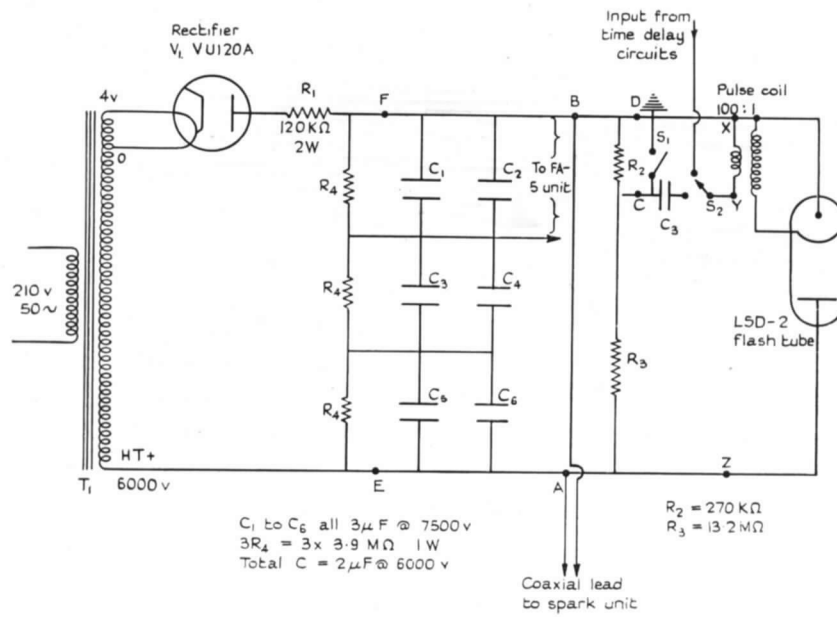
FIG. 46. Electronic flash unit.
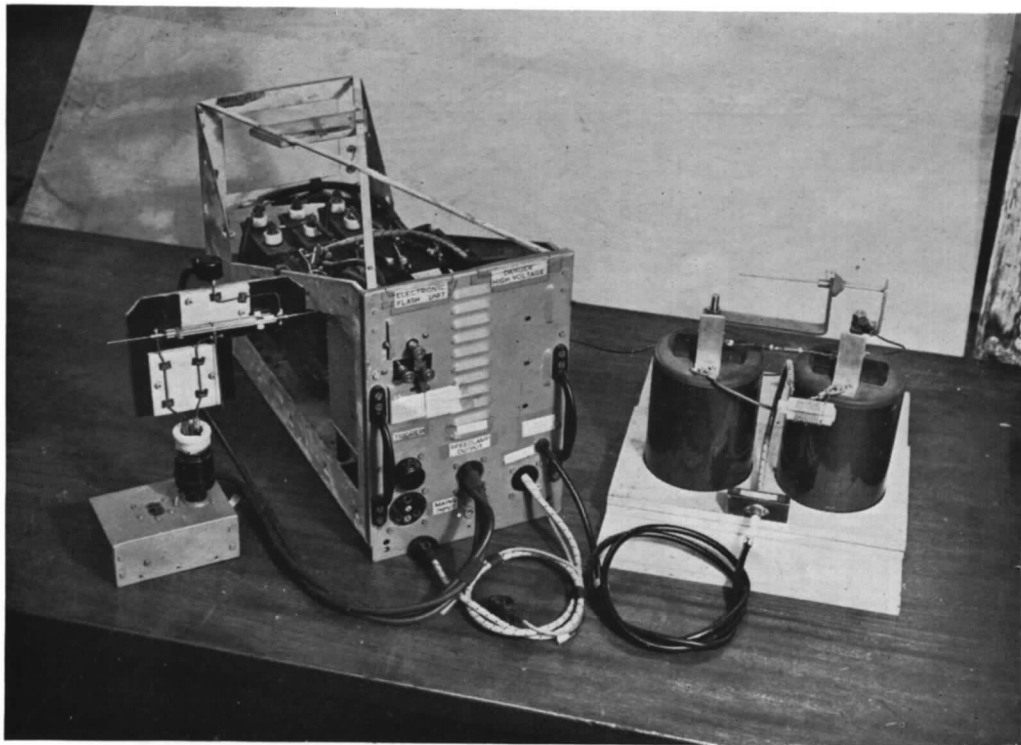
FIG. 47. Flash unit and spark unit.
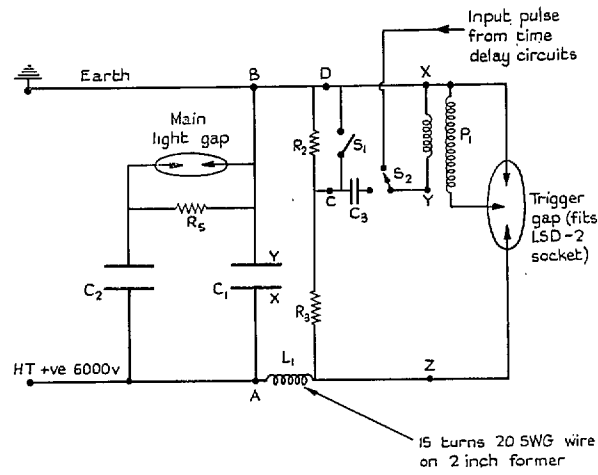
R_2 = 270 KΩ 1W
R_3 = 13·2 MΩ 1W
R_5 = 5 MΩ 1W

L_1 = 10 micro henries
P_1 = Pulse coil 100-1
C_3 = 2μF 1000 v

C_1 = C_2 = 0·1 μF 7500 v
Special DC pulse condensers

FIG. 48.   Circuit diagram: spark unit.

Distance from mirror to image I
or to slit S = $2f_1$
Distance from image to L_2 = d
Distance from L_2 to screen C = e
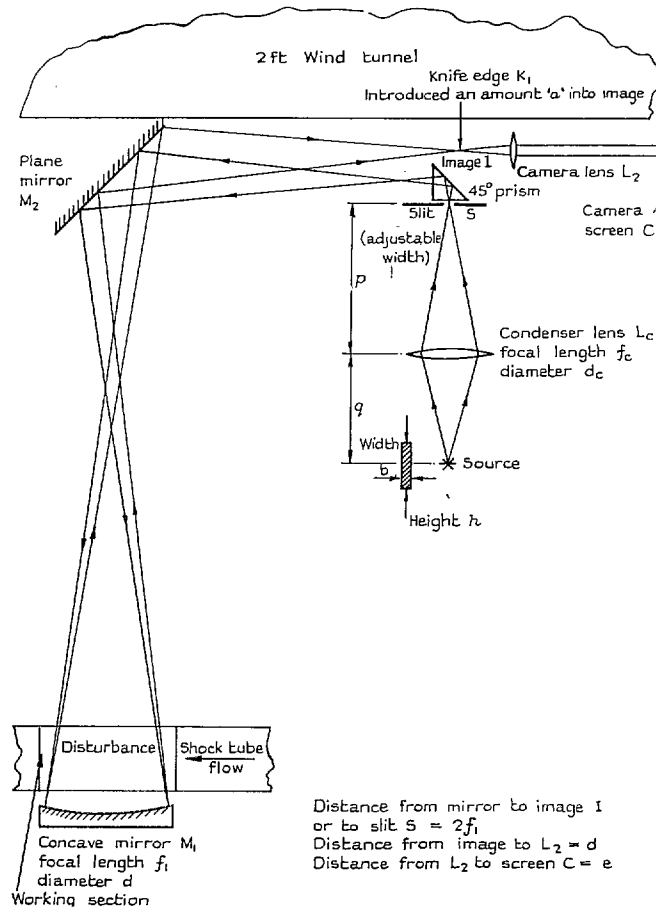
FIG. 49.   Schematic diagram: the main optical system.

91
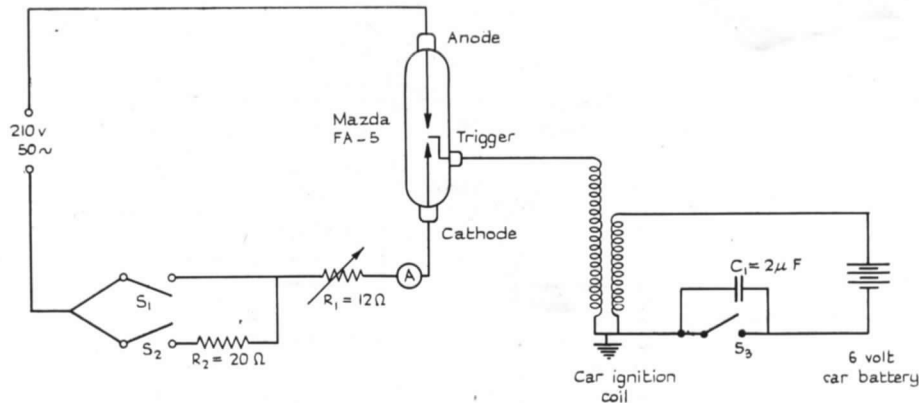
Fig. 50.   Circuit diagram: Mazda FA–5 starting circuit.
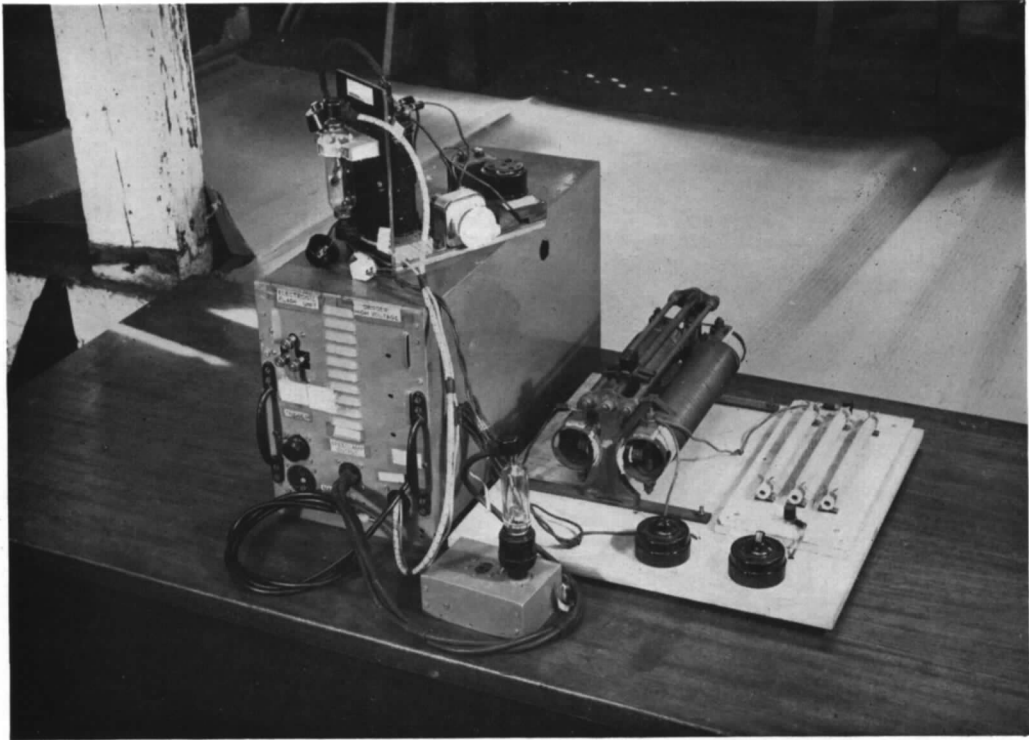
Fig. 51.   Mazda FA–5 units.
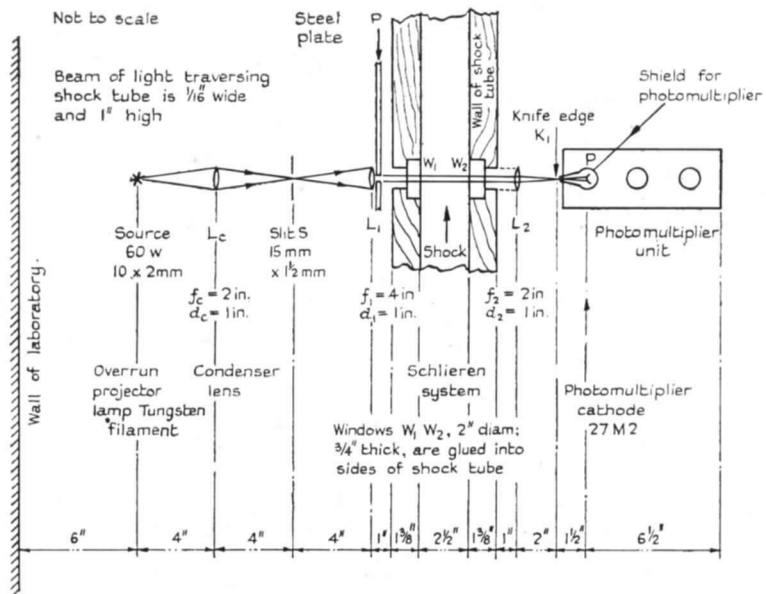
Fig. 52.   Schematic diagram: a light screen.
Plan view.

92
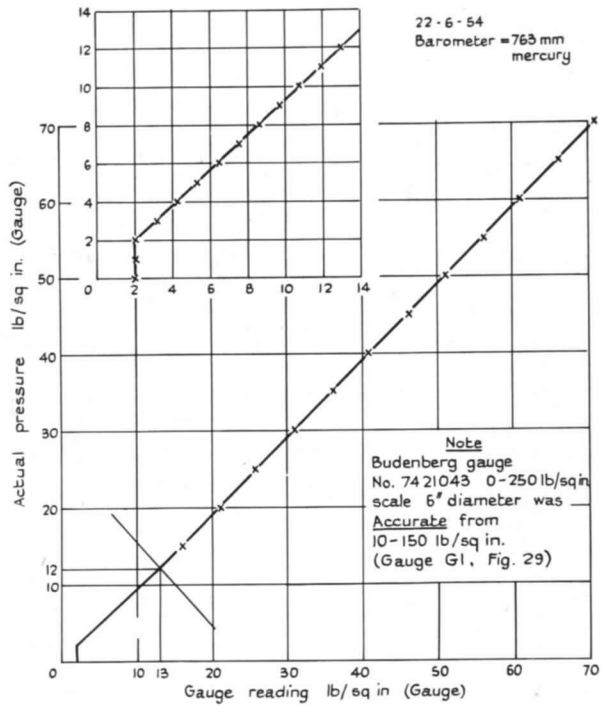
FIG. 54.   Calibration of high pressure chamber gauges.

Calibration chart for Budenberg gauge No. 7584116.
10 in. diam. : scaled 0–120 lb/sq in. (gauge G_2 Fig. 29).
From 12–100 lb/sq in.; gauge reads 1 lb/sq in. too high.
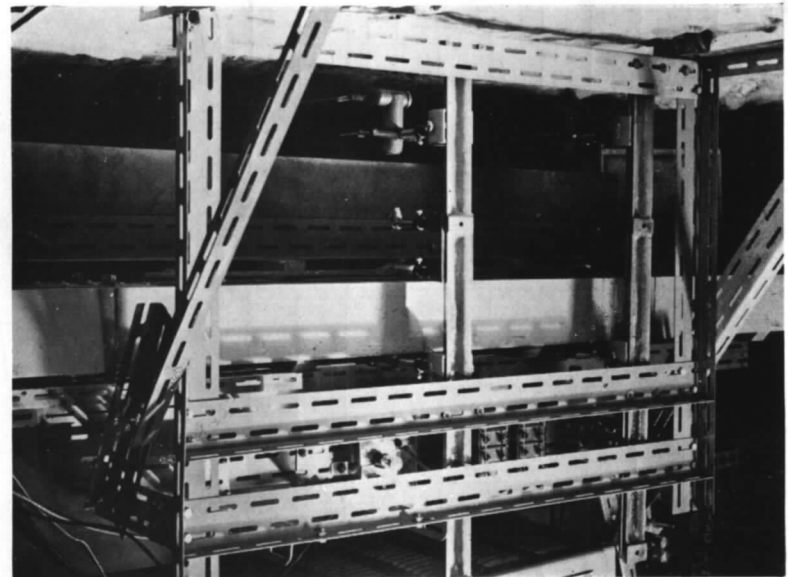
FIG. 53.   Mounting of light screens.
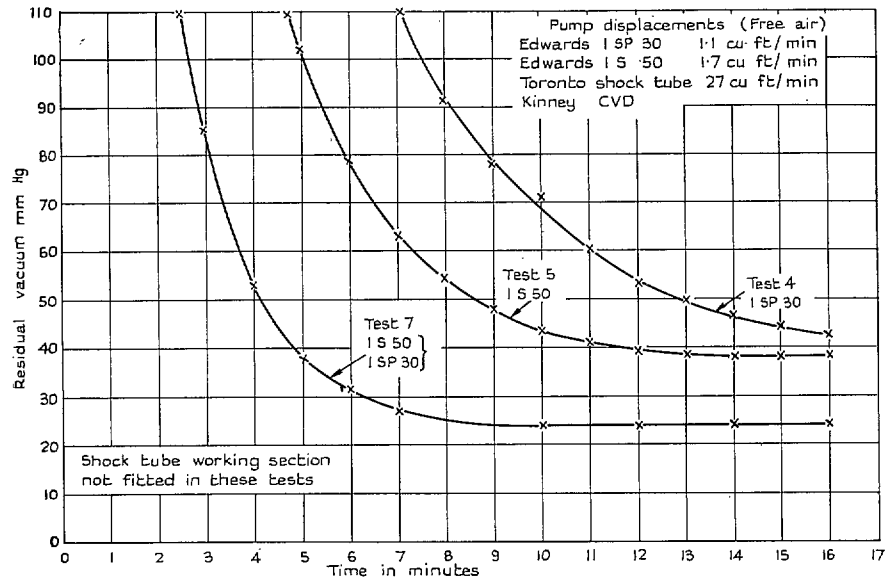
FIG. 55. Shock tube—channel evacuation—typical pump performance curves.
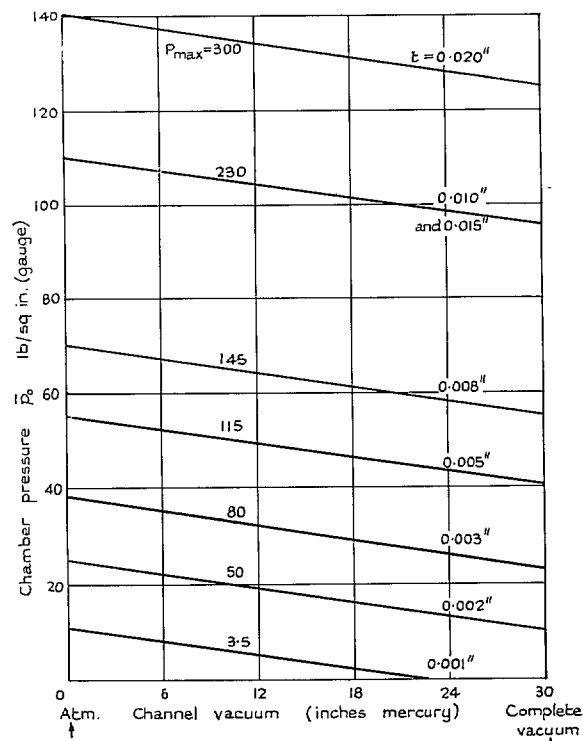
FIG. 56. Natural bursting pressures of various diaphragms.

All diaphragms were cellulose acetate sheet; thicknesses are specified above. (Assume atmospheric pressure = 30 in. mercury.) Assuming ultimate residual pressure in channel = 1 in. mercury, the maximum pressure ratios for each thickness are as given.
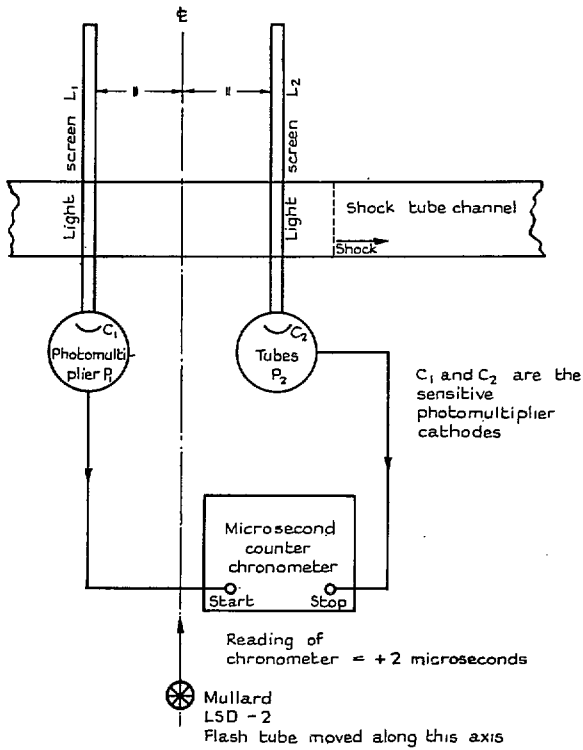
FIG. 57. Response times of light screens.

(a) Time delay unit alone

(b) Complete delay circuit
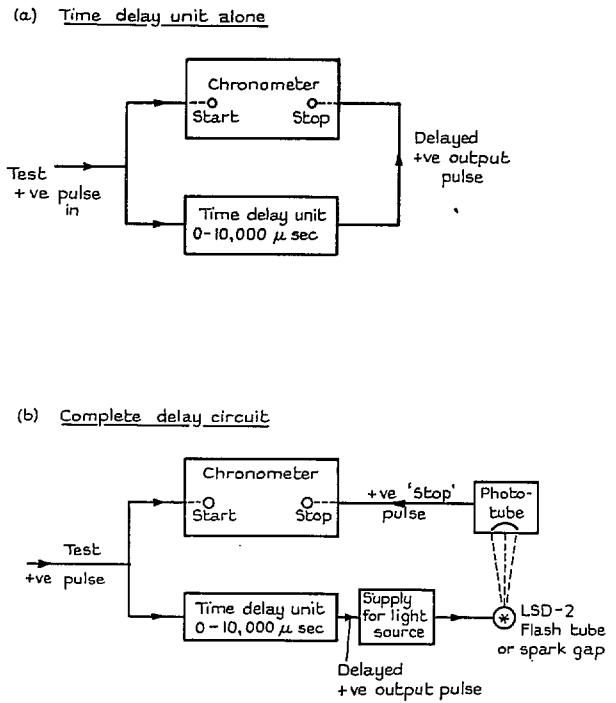
FIG. 58. Calibration of time-delay circuits. For a given delay unit setting. Reading (b) > reading (a) by 8 μ secs.
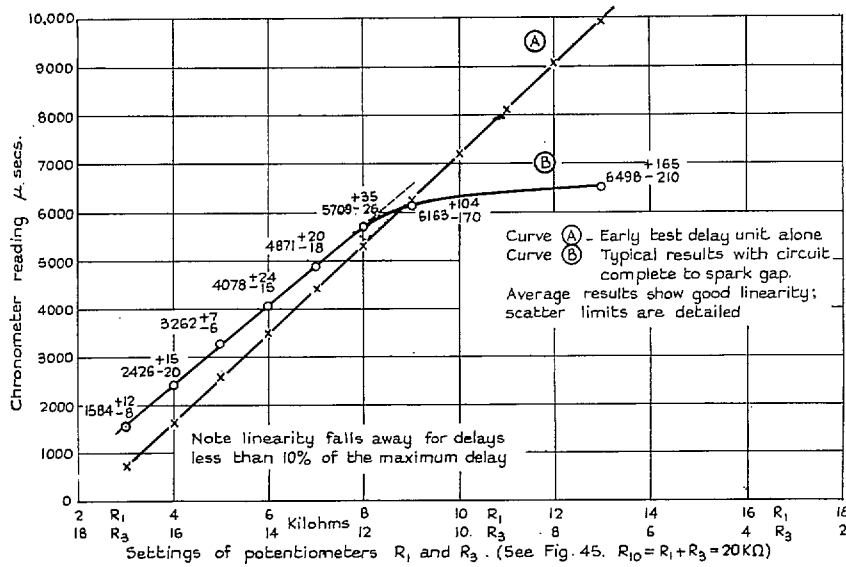
FIG. 59. Typical calibration results—Phantastron time-delay circuits.
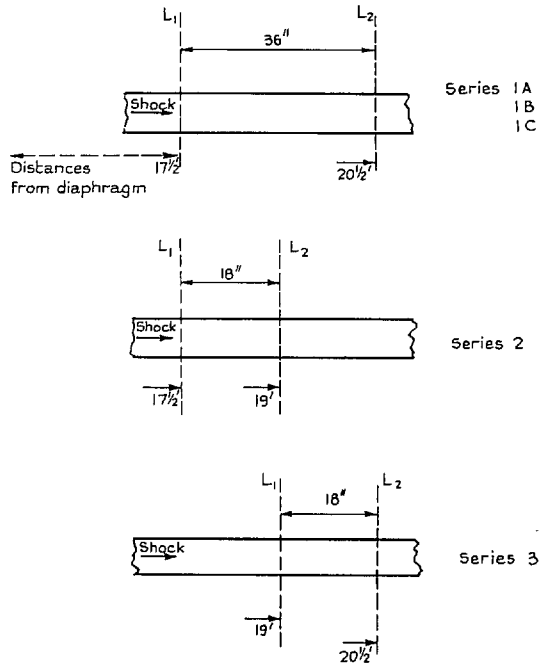
FIG. 60. Location of light screens during
calibration tests.

FIG. 61. Reduction of calibration results.

The chronometer readings C_1, C_2 corresponding to tests with pressure ratios P_X, P_Y may be converted to equivalent chronometer readings C_X, C_Y for a test with pressure ratio P_1 by drawing lines through experimental points X, Y, parallel to the tangent to the theoretical curve T at the point B.

FIG. 62. Shock-tube calibration—Series 1A results.
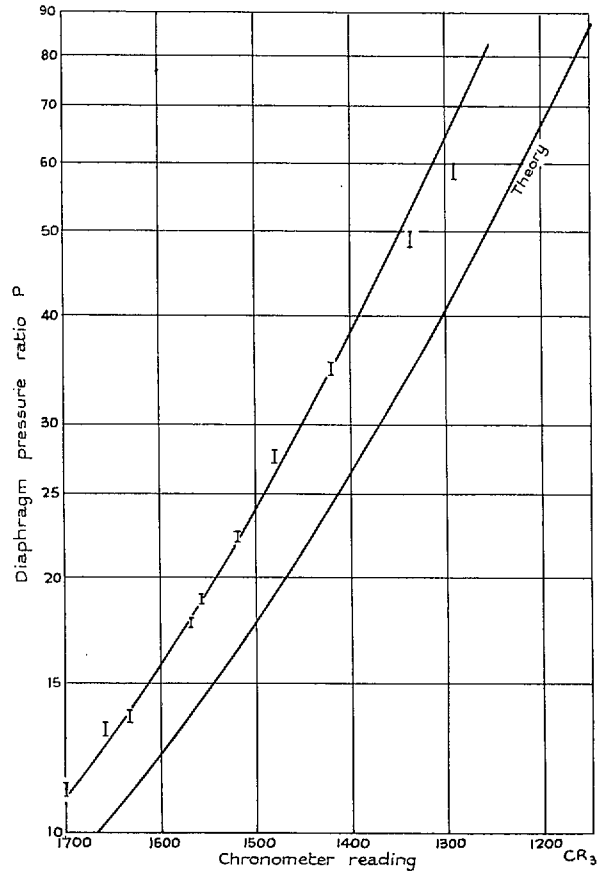
FIG. 63. Shock-tube calibration—Series 1B results.

96
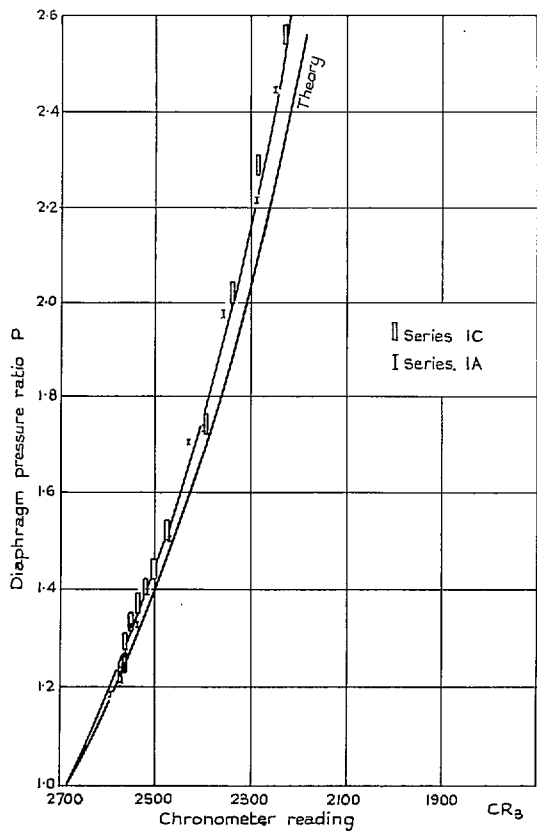
FIG. 64. Shock-tube calibration—Series 1A, 1C.
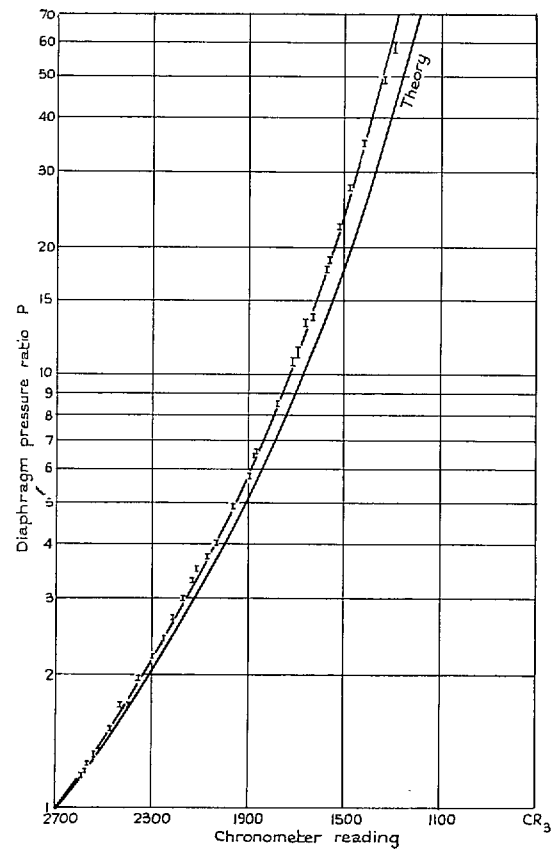
FIG. 65. Shock-tube calibration—Series
1A, 1B results.
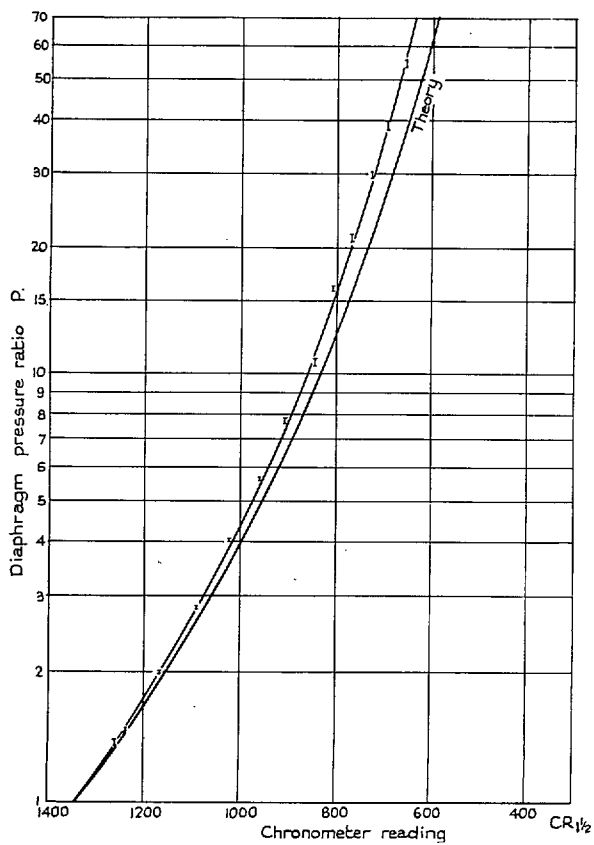
FIG. 66. Shock-tube calibration—Series 2 results.
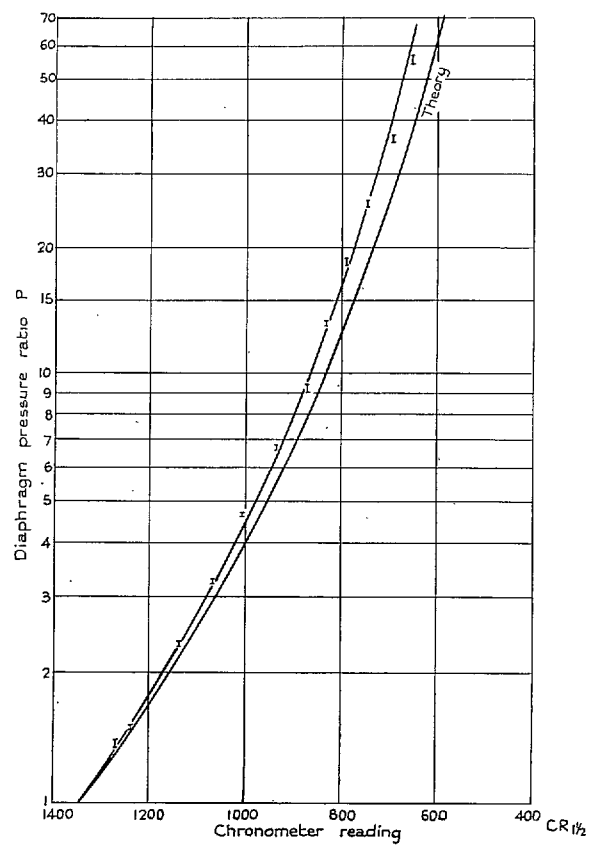
FIG. 67. Shock-tube calibration—Series 3 results.

97
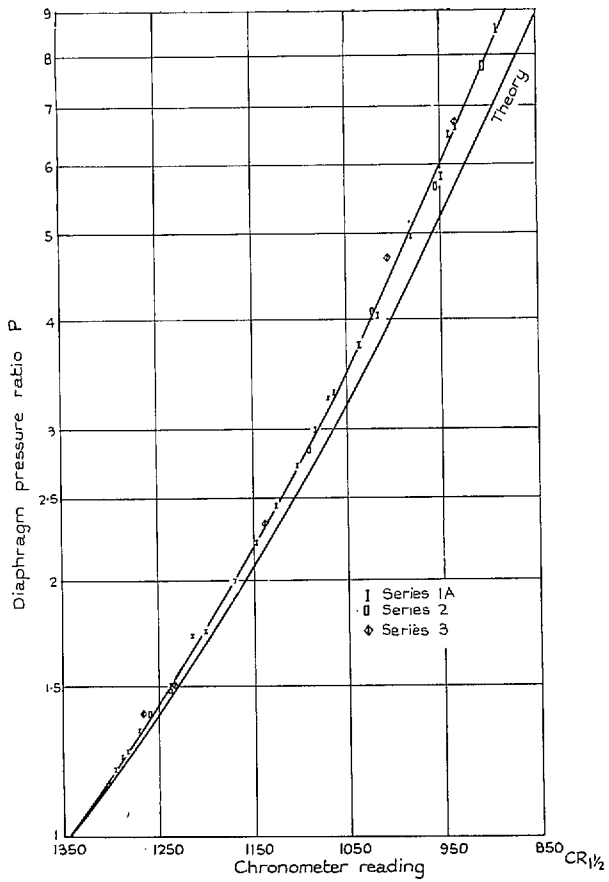
FIG. 68.   Shock-tube calibration—comparison
of results.
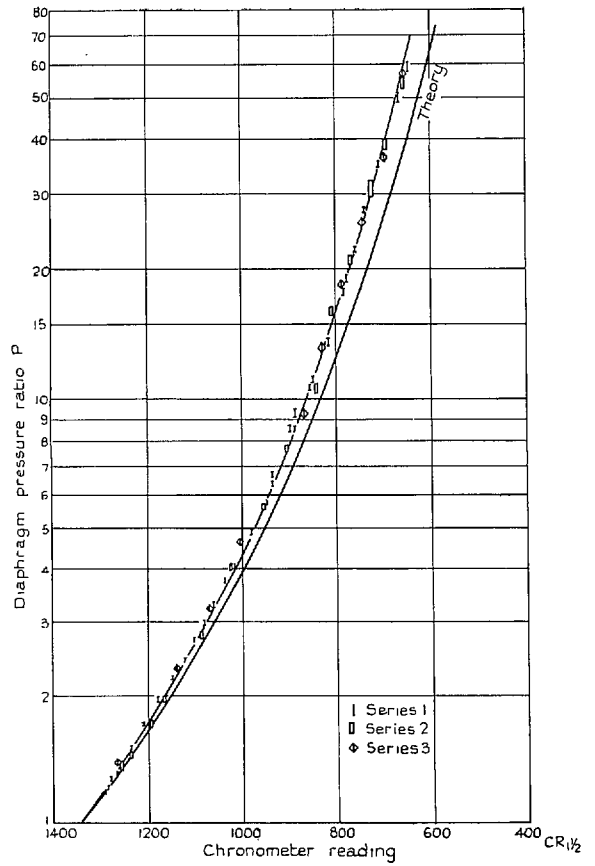
FIG. 69.   Shock-tube calibration—comparison
of results.
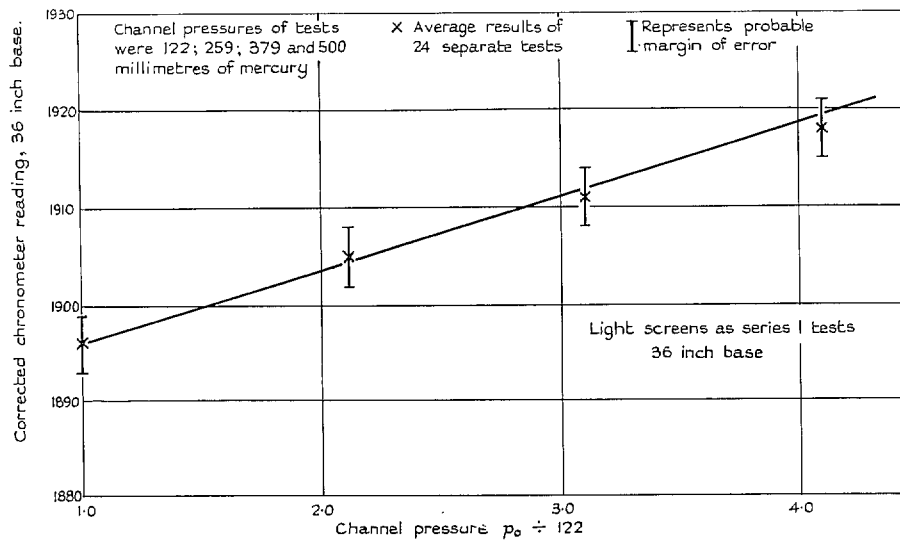
FIG. 70.   Shock tube: Reynolds number effects: diaphragm pressure ratio $P = 6 \cdot 10$.

98
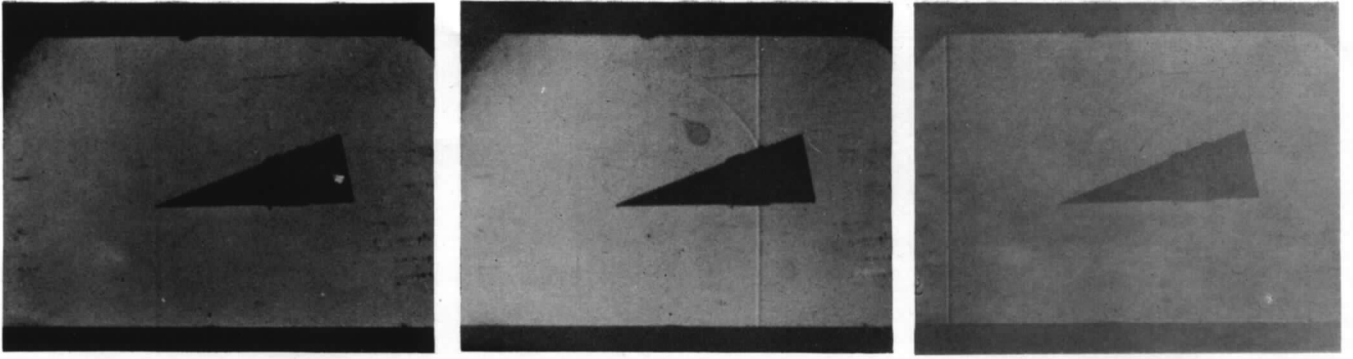
FA—5. Flash tube source. $P = 1 \cdot 30$;   LSD—2. Flash tube source. $P = 1 \cdot 33$;   Spark source. $P = 1 \cdot 37$;
$t = 4138\ \mu$ sec. $t = 4344\ \mu$ sec. $t = 3944\ \mu$ sec.

FIG. 71.   Shadow photographs: various light sources.
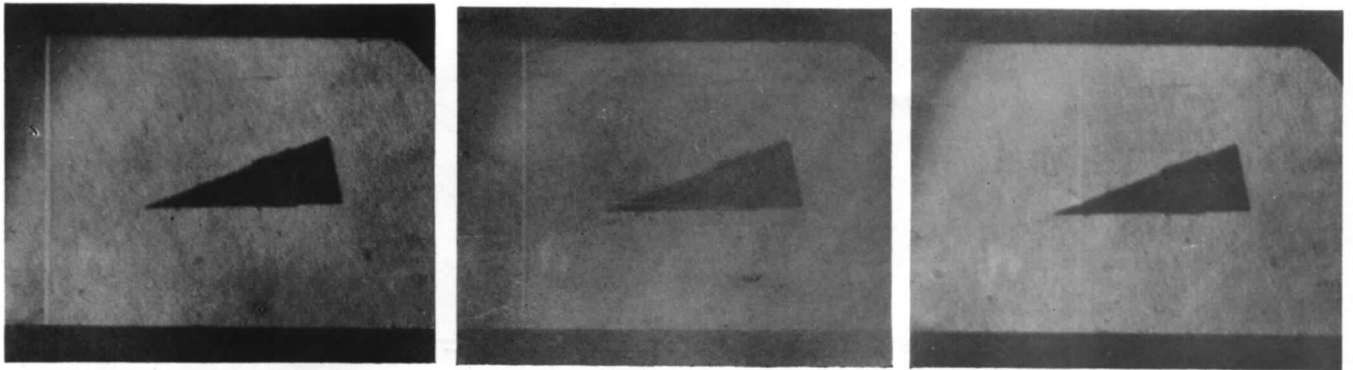
(a) $P = 1 \cdot 37$; $t = 4017\ \mu$ sec.   (b) $P = 1 \cdot 37$; $t = 4024\ \mu$ sec.   (c) $P = 1 \cdot 37$; $t = 4170\ \mu$ sec.
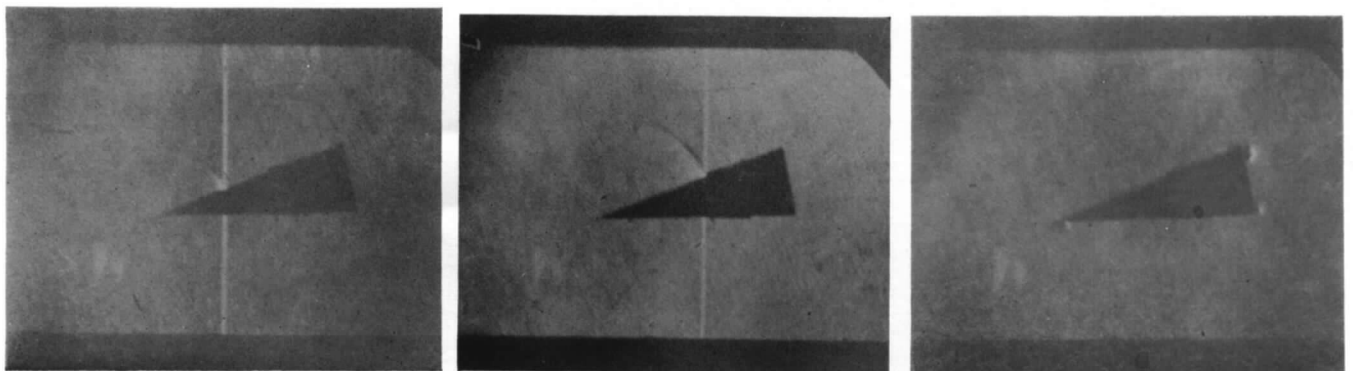
(d) $P = 1 \cdot 37$; $t = 4201\ \mu$ sec.   (e) $P = 1 \cdot 37$; $t = 4298\ \mu$ sec.   (f) $P = 1 \cdot 37$; $t = 4753\ \mu$ sec.

FIG. 72.   Schlieren photographs: LSD–2 source.   Flow over a 10-deg wedge.
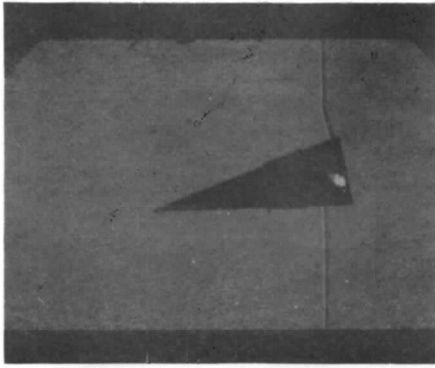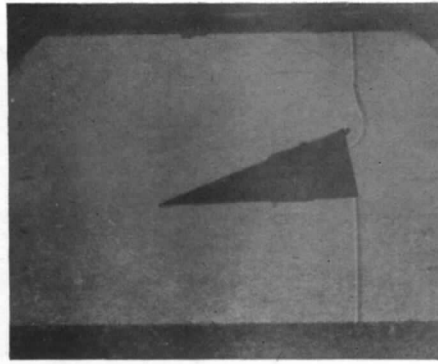
(a) $P = 4 \cdot 47$; $t = 3399\ \mu$ sec.   (b) $P = 3 \cdot 82$; $t = 3616\ \mu$ sec.   (c) $P = 4 \cdot 35$; $t = 3566\ \mu$ sec.
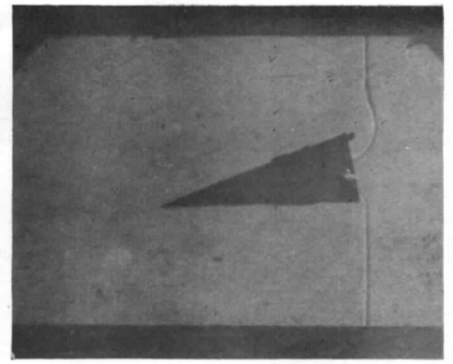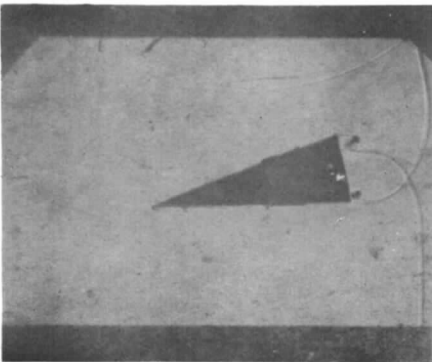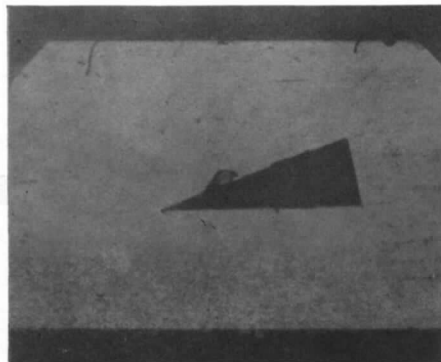
(d) $P = 4 \cdot 23$; $t = 3606\ \mu$ sec.   (e) $P = 4 \cdot 41$; $t = 3888\ \mu$ sec.   (f) $P = 3 \cdot 88$; $t = 3972\ \mu$ sec.
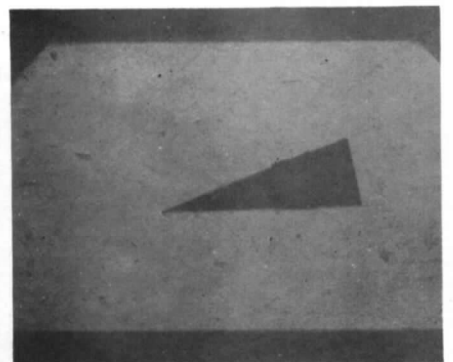
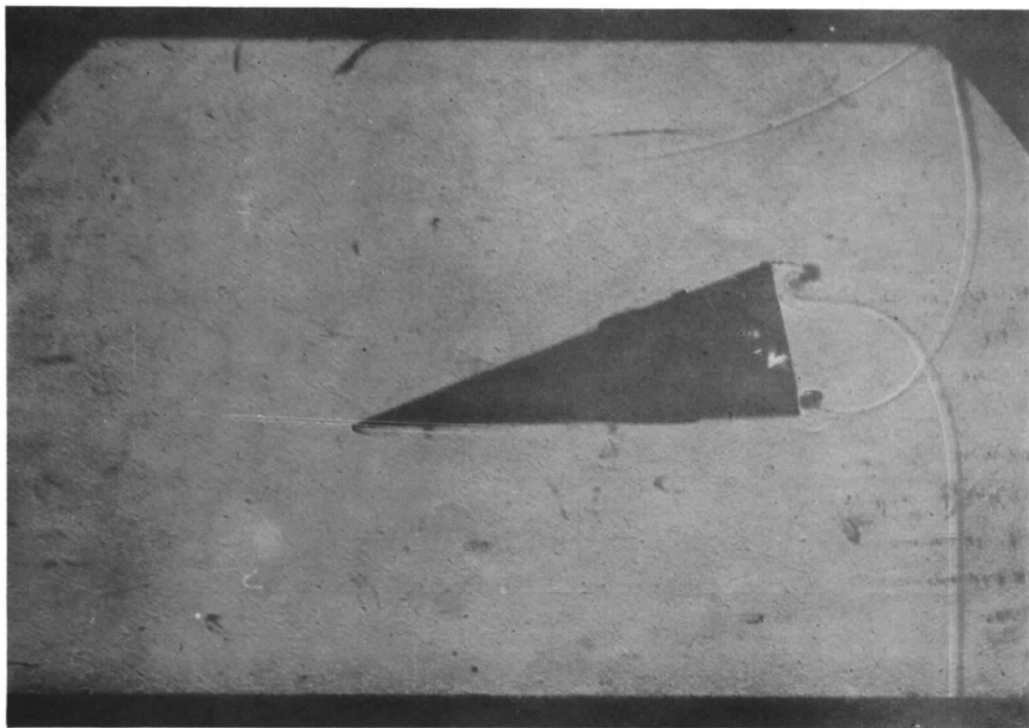Fig. 73.   Shadow photographs: spark source.   Flow over a 10-deg wedge.

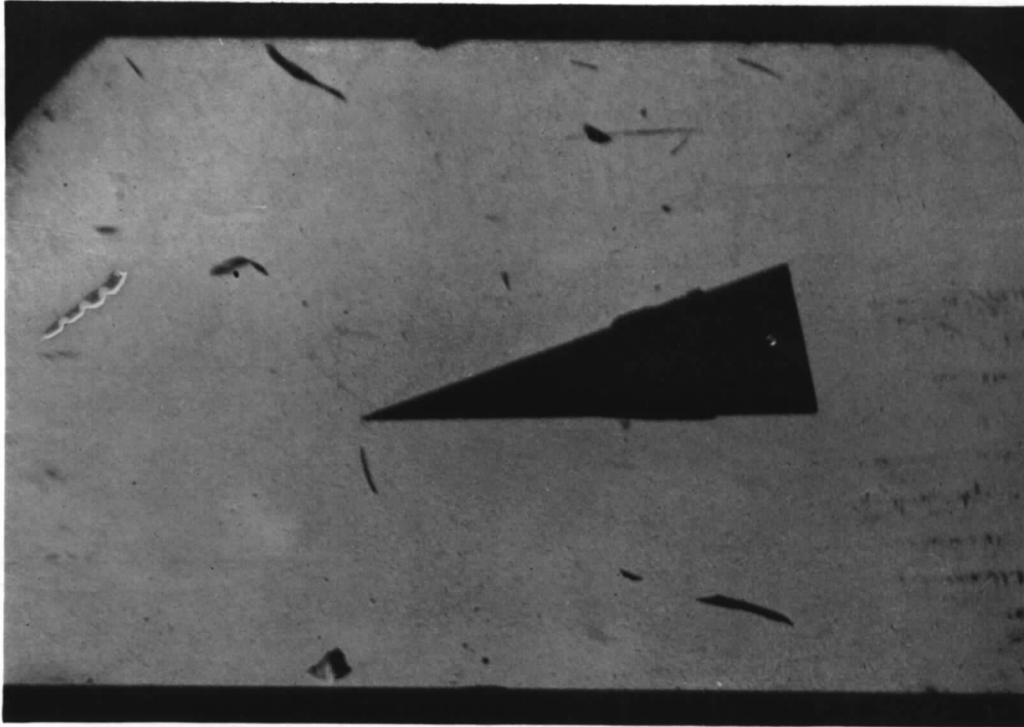Fig. 74.   Spark shadowgraph.   Detail of flow over a 10-deg wedge.

100

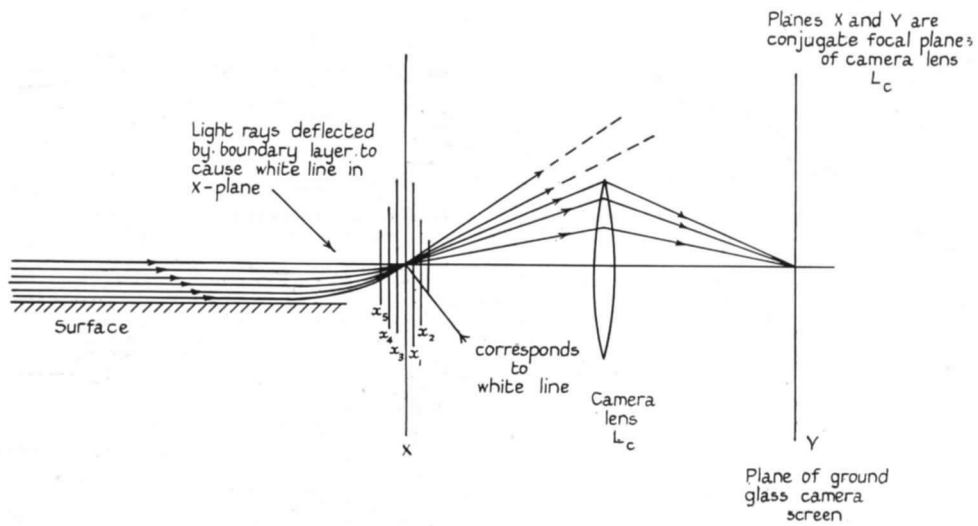FIG. 75. Shadowgraph: LSD–2 source. Detail of flow over a 10-deg wedge.

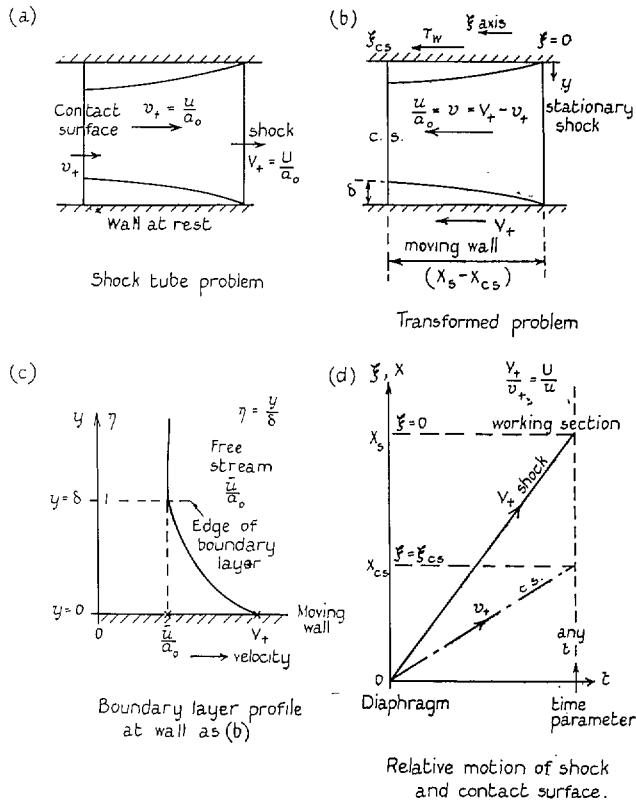FIG. 76. Determination of the state of a boundary layer from shadowgraph pictures.

FIG. 77. Boundary-layer effects: transformation I.

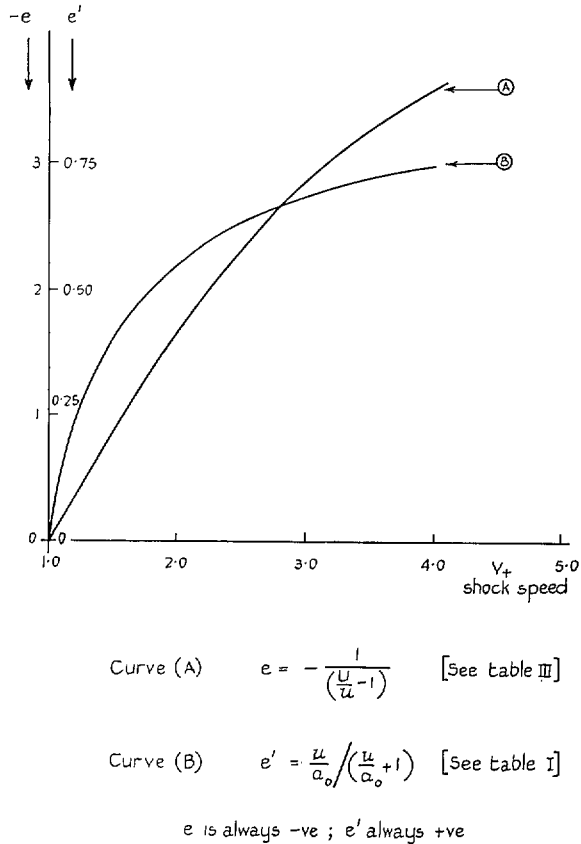Consideration of flow region between the shock and the contact surface.

(a) Shock tube problem

(b) Transformed problem

(c) Boundary layer profile at wall as (b)

(d) Relative motion of shock and contact surface.

$t_2 > t_1$

For any given ζ; δ_ζ is constant.

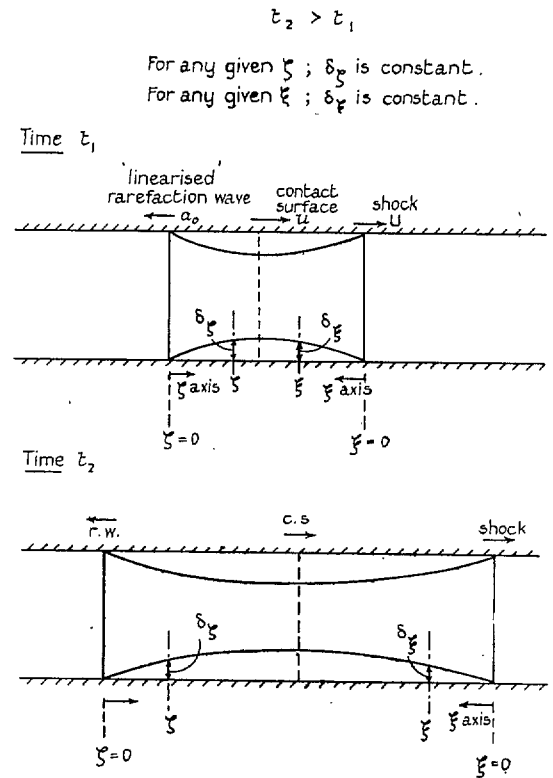For any given ξ; δ_ξ is constant.

Time t_1

Time t_2

FIG. 78. The fundamental assumption of the boundary-layer analysis.

Instantaneous pictures of shock-tube flow at two consecutive times.

Curve (A) $\quad e = -\dfrac{1}{\left(\frac{U}{u}-1\right)}$ [See table III]

Curve (B) $\quad e' = \dfrac{u}{a_0}\Big/\left(\dfrac{u}{a_0}+1\right)$ [See table I]

e is always $-ve$; e' always $+ve$

FIG. 79. Boundary-layer effects: dependence of functions e and e' on shock speed.

(a) Shock tube problem

(b) Transformed problem

(c) Boundary layer velocity profile at wall as (b)

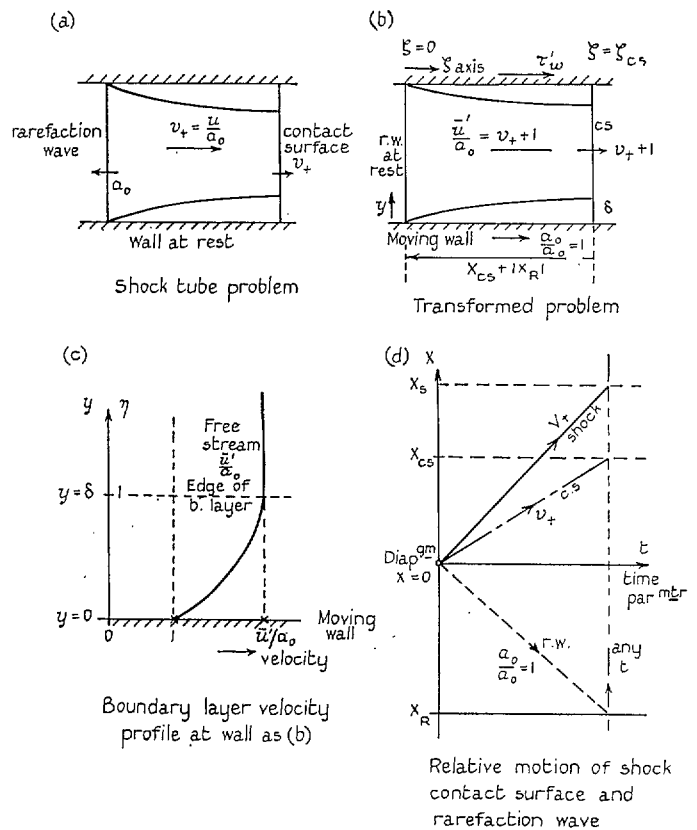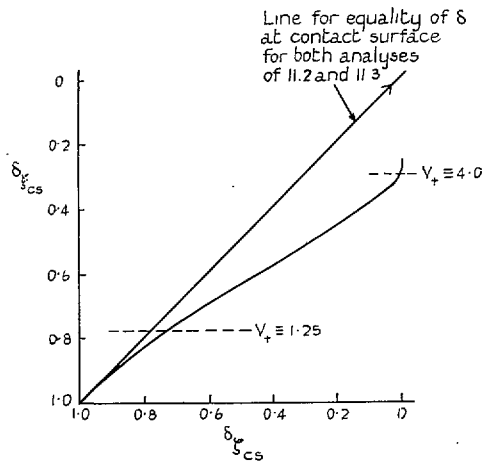(d) Relative motion of shock contact surface and rarefaction wave

FIG. 80. Boundary-layer effects; transformation II.

Simplified consideration of the flow region between the rarefaction wave and the contact surface.

102

$$\frac{\delta_{\zeta_{cs}}}{\delta_{\xi_{cs}}} = \frac{\left(1 + \frac{v_+}{V_+}\right)}{\left(1 - \frac{74}{189}\frac{v_+}{V_+}\right)} \left[\frac{(1 + v_+)}{\left(1 + \frac{74}{189}v_+\right)} \cdot \left(\frac{\overline{T}}{T}\right)^{7/4}\right]^{-1} \quad \ldots\ldots(\text{II.34})$$

For given values of V_+ as parameter, equation (II.34) above may be evaluated

$\frac{v_+}{V_+}$ values — Table III , v_+ — Table I and $\left(\frac{\overline{T}}{T}\right)$ — Table V

FIG. 81.   Relations for boundary-layer thickness at the contact surface.
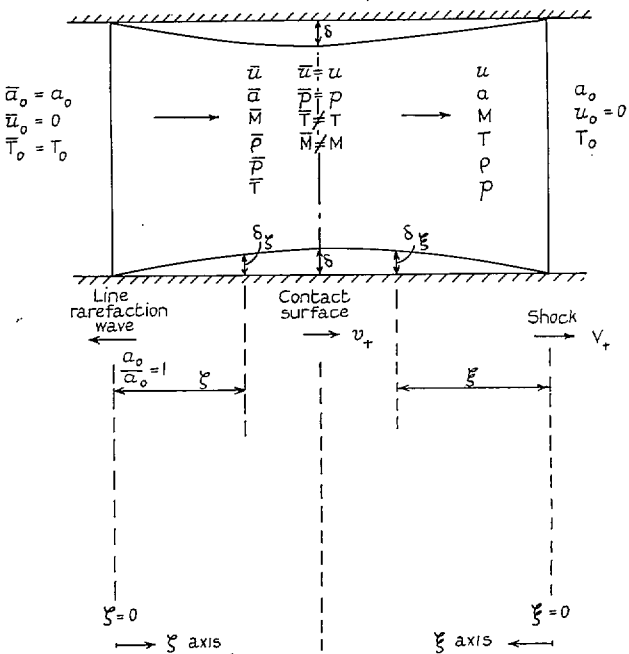

FIG. 82.   Determination of the boundary-layer profile in a shock tube at any given instant.

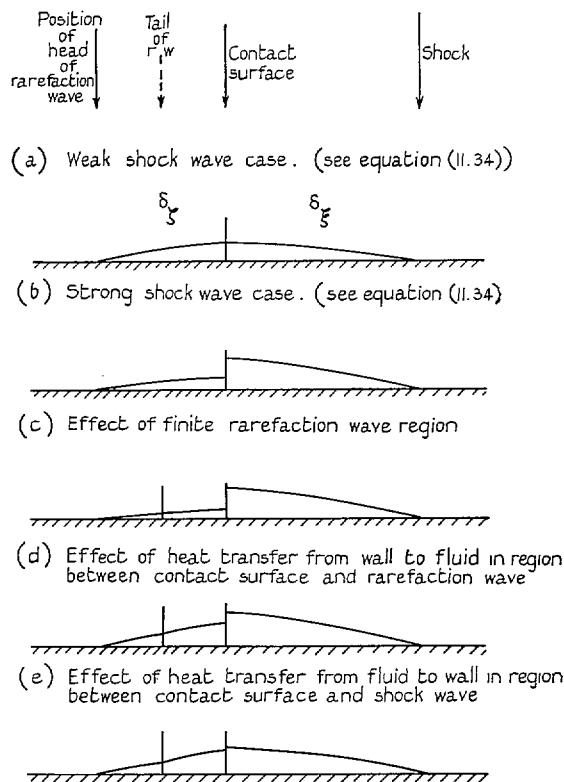Diagram of shock-tube flow at some instant after diaphragm has been ruptured.

(a) Weak shock wave case. (see equation (II.34))

(b) Strong shock wave case. (see equation (II.34))

(c) Effect of finite rarefaction wave region

(d) Effect of heat transfer from wall to fluid in region between contact surface and rarefaction wave

(e) Effect of heat transfer from fluid to wall in region between contact surface and shock wave

FIG. 83.   Boundary-layer thicknesses at the contact surface.

103

Publications of the

Aeronautical Research Council

ANNUAL TECHNICAL REPORTS OF THE AERONAUTICAL RESEARCH COUNCIL (BOUND VOLUMES)

1939 Vol. I. Aerodynamics General, Performance, Airscrews, Engines. 50s. (51s. 9d.).
  Vol. II. Stability and Control, Flutter and Vibration, Instruments, Structures, Seaplanes, etc.
    63s. (64s. 9d.)

1940 Aero and Hydrodynamics, Aerofoils, Airscrews, Engines, Flutter, Icing, Stability and Control
    Structures, and a miscellaneous section. 50s. (51s. 9d.)

1941 Aero and Hydrodynamics, Aerofoils, Airscrews, Engines, Flutter, Stability and Control
    Structures. 63s. (64s. 9d.)

1942 Vol. I. Aero and Hydrodynamics, Aerofoils, Airscrews, Engines. 75s. (76s. 9d.)
  Vol. II. Noise, Parachutes, Stability and Control, Structures, Vibration, Wind Tunnels.
    47s. 6d. (49s. 3d.)

1943 Vol. I. Aerodynamics, Aerofoils, Airscrews. 80s. (81s. 9d.)
  Vol. II. Engines, Flutter, Materials, Parachutes, Performance, Stability and Control, Structures.
    90s. (92s. 6d.)

1944 Vol. I. Aero and Hydrodynamics, Aerofoils, Aircraft, Airscrews, Controls. 84s. (86s. 3d.)
  Vol. II. Flutter and Vibration, Materials, Miscellaneous, Navigation, Parachutes, Performance,
    Plates and Panels, Stability, Structures, Test Equipment, Wind Tunnels.
    84s. (86s. 3d.)

1945 Vol. I. Aero and Hydrodynamics, Aerofoils. 130s. (132s. 6d.)
  Vol. II. Aircraft, Airscrews, Controls. 130s. (132s. 6d.)
  Vol. III. Flutter and Vibration, Instruments, Miscellaneous, Parachutes, Plates and Panels,
    Propulsion. 130s. (132s. 3d.)
  Vol. IV. Stability, Structures, Wind Tunnels, Wind Tunnel Technique. 130s. (132s. 3d.)

Annual Reports of the Aeronautical Research Council—

  1937 2s. (2s. 2d.)   1938 1s. 6d. (1s. 8d.)   1939–48 3s. (3s. 3d.)

Index to all Reports and Memoranda published in the Annual Technical Reports, and separately—

  April, 1950   -   -   -   -   R. & M. 2600   2s. 6d. (2s. 8d.)

Author Index to all Reports and Memoranda of the Aeronautical Research Council—

  1909—January, 1954   R. & M. No. 2570   15s. (15s. 6d.)

Indexes to the Technical Reports of the Aeronautical Research Council—

  December 1, 1936—June 30, 1939   R. & M. No. 1850   1s. 3d. (1s. 5d.)
  July 1, 1939—June 30, 1945   R. & M. No. 1950   1s. (1s. 2d.)
  July 1, 1945—June 30, 1946   R. & M. No. 2050   1s. (1s. 2d.)
  July 1, 1946—December 31, 1946   R. & M. No. 2150   1s. 3d. (1s. 5d.)
  January 1, 1947—June 30, 1947   R. & M. No. 2250   1s. 3d. (1s. 5d.)

Published Reports and Memoranda of the Aeronautical Research Council—

  Between Nos. 2251–2349   R. & M. No. 2350   1s. 9d. (1s. 11d.)
  Between Nos. 2351–2449   R. & M. No. 2450   2s. (2s. 2d.)
  Between Nos. 2451–2549   R. & M. No. 2550   2s. 6d. (2s. 8d.)
  Between Nos. 2551–2649   R. & M. No. 2650   2s. 6d. (2s. 8d.)

Prices in brackets include postage

HER MAJESTY'S STATIONERY OFFICE